



THE UNIVERSITY
of ADELAIDE

SCHOOL OF EARTH AND
ENVIRONMENTAL SCIENCES

Petrography, mineralogy and trace element chemistry of Cu-Au-Mo mineralisation from Central Diorite, Boddington, W.A.

Ryan J. Guerin

**Supervisor
Cristiana L. Ciobanu**

**Co-supervisor
Nigel J. Cook**

Centre for Tectonics, Resources and Exploration
School of Earth and Environmental Sciences
The University of Adelaide, South Australia
ryan.guerin@student.adelaide.edu.au

ABSTRACT

The world-class Boddington Cu-Au-Mo deposit has a complex genetic history. The relative importance of different ore-forming processes during the period 3.0 – 2.6 Ga is debated, particularly with respect to the role played by the 2611 ± 3 Ma Wourahming granite. LA-ICP-MS analysis of trace element concentration in molybdenite represents a valuable new metallogenic tool to track mineralising events in deposits with protracted geologic histories. The Re content and trace-element signatures in molybdenite from diorite and granite show three distinct populations, attributed to porphyry-style (hundreds of ppm) orogenic- and granite-related systems (<1 to a few ppm, respectively). Rhenium concentrations in molybdenite are highly variable on the deposit-scale. Economic concentrations of Re occur only at shallower levels in both Central Diorite and ABreccia. The Au content correlates with high-concentrations of chalcophile elements (CE). This is seen in the association of Au-minerals and Bi-(Pb)-tellurides present as inclusions in the molybdenite from diorite and is inferred from an LA-ICP-MS element map for molybdenite in granite.

The FIB-SEM and TEM study show that visible telluride inclusions extend down to the nanoscale as coherent intergrowths with host molybdenite. Nanoporosity is accompanied by a whole range of structural defects and twinning. The telluride species identified include unnamed $\text{Bi}_4\text{Pb}_7\text{Te}_4\text{S}_9$. Analysis of stacking sequences show co-precipitation of Bi-tellurides and molybdenite under equilibrium conditions. In corroboration with EPMA data, this is the first confirmation that minerals from the aleksite series are characteristic components of the ore at Boddington. Molybdenite with high-concentration of chalcophile elements is present as the 2H polytype only, contrary to previous hypothesis that incorporation of trace elements is assisted by 3R structural modification. Instead, a new mechanism is presented in which coherent lattice-scale intergrowths between molybdenite and tellurides are reasons for the measured high CE concentrations. Knowing that Bi-(Pb)-tellurides are Au-carriers, this may also explain the observed, unusual Au-enrichment in molybdenite from Boddington. Nucleation of Au fine particles is inferred from element map correlations but further work is necessary to prove if Au nanoparticles are also present.

Petrographic, mineralogical and geochemical evidence support a three-stage model for Boddington. An early porphyry event can account for the bulk of the Cu mineralisation, as well as some of the Au and Mo. A subsequent orogenic-Au event led to shearing and remobilisation of ore components. New constraints on metamorphic conditions are offered by

chlorite and stannite-sphalerite geothermometry (200-420 °C) and the occurrence of two co-existing pyrrhotite species. The granite introduced some Au, Mo and other ‘granitic’ elements, notably Bi leading to substantial upgrading of Au grades by Bi-melt scavenging. The study concludes however that hydrothermal activity associated with granite was not the most important concentrator of ore minerals.

INTRODUCTION

The Boddington Cu-Au mine is located 100 km SSE of Perth, W.A., and is situated within the Archean Saddleback Greenstone Belt, a segment of the Yilgarn Craton. The deposit was originally discovered in 1980. Newmont Asia-Pacific developed the existing mine on a much larger scale than the original mine; starting production in 2009 (Hayes 2009).

A genetic model for the Boddington deposit which explains all observations has been difficult to derive since the deposit shows a number of features which are atypical of many other deposits in the Yilgarn Craton. As a consequence, a number of different models have been put forward (e.g. Roth & Anderson 1993, Allibone *et al.* 1998, McCuaig *et al.* 2001, Stein *et al.* 2001, Hagemann *et al.* 2007).

A previous University of Adelaide honours project (Kalleske 2010) made two important new findings: firstly that Re concentrations, and to some extent also Au concentrations within molybdenite are commonly extremely high; and secondly that Bi-tellurides are widespread throughout the deposit, generally associated with elevated Au grades. The geochemistry of molybdenite showed promise as a new method to constrain ore genesis, in particular the role of the late Wourahming granite as a source of ore metals or heat source driving remobilisation.

Using a variety of microanalytical methods, the present project aims to significantly enlarge the geochemical dataset for molybdenite, focussing in particular on high-grade areas of the Central Diorite orebody and the Wourahming monzogranite. The primary goal is to identify whether the geochemical trends reported by Kalleske (2010) are consistent within the larger dataset and, if so, to understand the underlying controls on molybdenite geochemistry and its apparent inhomogeneity in the context of multistage ore genesis.

Secondary goals include an attempt to better constrain the types of alteration present at Boddington, an assessment of metamorphic conditions (using chlorite and sphalerite-stannite geothermometry) and an evaluation of the petrogenetic information within a number of trace

minerals in the deposit. The large number and varied compositional character of different trace minerals in the Boddington deposit carries inferences for any genetic model and any attempt to constrain conditions of ore formation or superimposed modification.

GEOLOGICAL SETTING OF THE BODDINGTON DEPOSIT

A large portion of Western Australia is composed of Archean metavolcanic and metasedimentary rocks initially formed at 3050-2600 Ma (Myers 1993, Duuring *et al.* 2007). These rocks were originally part of volcanic arcs, back arc basins and microcontinents that amalgamated during a time of tectonic movement and formed the Yilgarn Craton (Myers 1993). Crustal fragments were aligned and became joined during a period of increased tectonic activity dated at 2780-2630 Ma (Myers 1993). A significant section of the Yilgarn Craton is comprised of granitoids and associated greenstone belts that underwent metamorphism. All greenstone belts in W.A. contain packages of igneous and sedimentary rocks that display similar lithologies and broad-scale structural controls. Greenstone belts are widely associated with metallic mineral deposits, since the latter form in volcanic arc and back arc basin environments where faulting can occur (Barley *et al.* 1990).

Boddington is a Cu-Au deposit with associated Mo, W and Bi. The deposit is located in the northern part of the 50 km-long, NNW-striking Saddleback Greenstone Belt (SGB). This belt forms a part of the southwestern Yilgarn Craton (Allibone *et al.* 1998). The trace element chemistry of diorite intrusions (2715-2690 Ma) from the SGB implies formation in an island arc setting (Allibone *et al.* 1998, McCuaig *et al.* 2001). Initial basaltic and dacitic volcanism occurred at 2714-2696 Ma. Magmatic activity was initiated again at 2675 Ma as a series of dikes. The greenstone belt is enclosed by the Western Gneiss Terrane which hosts the Wourahming monzogranite dated at 2611 ± 3 Ma (Allibone *et al.* 1998).

The Boddington deposit strikes NW-SE over a length of 4 km, with a width of 1 km (Le May 2010). Mineralisation is contained within felsic to intermediate volcanic and sedimentary rocks. Mineralisation occurs within shear zones, brittle ductile faults, veins and reactivated veins, veinlets, lenses and disseminated ores. The deposit is currently mined via two open pits (North and South). The North Pit is further divided into ABreccia, Blob, Son of Blob and North Diorite and the South Pit is divided into Blackbutt, Central Diorite, Pipeline and Southern Diorite Deep (Figure 1). The Southern Diorite Deep zone has not yet been mined as it is below the depths of the pit. The Central Diorite is a high-grade zone that is

currently being mined (at time of fieldwork) at the U108 level. At the end of 2010, in addition to 728,000 Oz Au, the mine had produced ~27,000 t Cu. Copper reserves are estimated at 1.2 Mt.

The Boddington greenstone sequence is divided into three formations. The formations hosting the Boddington deposit are the 2714-2696 Ma Wells and Marradong Formations; the Hotham Fm. is structurally below these two formations (Wilde *et al.* 1986). The Wells Fm. has a thickness of 2-5.5 km and comprises felsic volcanic rocks alternating with lavas and breccias that recrystallized during metamorphism at ~2640 Ma. The Marradong Fm. (on top of the Wells Fm.) consists of metamorphosed actinolite- and albite-epidote-dominant basalts (Wilde *et al.* 1986). Deposit mineralogy shows that a dominant lower amphibolite facies metamorphism was followed by retrograde metamorphism (greenschist-amphibolite facies boundary conditions), especially around lithological contacts (Wilde *et al.* 1986). Brittle-ductile faults were widely developed during this metamorphic event (Allibone *et al.* 1998).

The series of deformational events at Boddington is hotly debated. Allibone *et al.* (1998) propose seven distinct post-mineralisation deformational events. In this scheme, molybdenite and chalcopyrite veins formed between 2714-2696 Ma before the first deformational event. Widespread metamorphism led to a quartz±oligoclase±albite-clinzoisite-muscovite-biotite±chlorite mineralogy and well-defined rock fabric. Sericite-quartz alteration then took place within shear zones after peak metamorphism. D₃ shears dated at post-2675 Ma hold quartz-albite-epidote alteration and cut through the previous two sets. Dikes were intruded along D₄ faults introducing actinolite-bearing veins and biotite-clinzoisite±actinolite alteration halos. Further movement on the D₄ faults introduced superimposed (remobilised?) mineralisation (Au+Cu+Mo+W quartz vein mineralisation and clinzoisite-biotite-pyrrhotite-chalcopyrite veins).

The giant size and unusual geochemical features of the Boddington deposit would suggest at least two mineralisation events, even if researchers disagree about what these events represent (see 'Discussion' section).

SAMPLING, APPROACH AND METHODOLOGY

Fieldwork

The Boddington deposit is confined between two main shear zones and the Central Diorite is placed within the southern part of the Open Pit; it is truncated to the South by an E-W fault (Figure A1a). A dense swarm of mafic (and locally ultramafic) dykes, both longitudinal and oblique, occur within the deposit (Figure A1b). Even though some of these dykes are Archean, the majority are Proterozoic, post-dating mineralisation. They are monitored because they represent mine waste.

Sampling was carried out in April 2011 in the Open Pit at RL 108 (11 samples) and in 4 drillcores (42 samples) (Figure 1) where molybdenite is present. One drillcore intersects the Wourahming granite (~1 km SE from the other drillcores). The granite plunges westwards and intersects the South-East Shear on the eastern side (Figure A2a, b). High-grade Mo and Au intervals were sampled from three drillcores in the Central Diorite (Figure A3a, b). Sampling intervals were located within the high-grade core defined as 'Southern Diorite Deep'. Sulphide mineralisation was also found in one of the drillcores intersecting the deepest margin of the Central Diorite. Samples from the Open Pit were collected from high Au-grade blocks (Figure A4). Drillcore intervals were chosen on the basis of assays (Figure A5), targeting the overlap between high-grade Au, Mo and Bi. Samples were selected on the basis of visible sulphides, including molybdenite. Details of the sampling intervals in all four drillcores, highlighting lithology and mineralisation, are presented in Figure A6-9.

Analytical Methods

A Nikon optical microscope equipped with a digital camera was used in reflected light mode (magnifying lenses up to 50x) to identify mineral associations and relevant textures.

Philips XL-30 and XL-40 scanning electron microscopes (SEM) at Adelaide Microscopy were used to examine selected sections. These instruments possess back-scatter electron (BSE) detectors to enable observation of subtle compositional differences. Both instruments were operated at an accelerating voltage of 20 eV, with a spot size of 4 (XL-30) or 4-6 depending on the mineralogy (XL-40). Special attention was given to micron-scale inclusions and fine-scale compositional zoning within minerals. Both SEMs are equipped with EDAX software permitting generation of semi-quantitative compositional information on 1-2 μm -

sized spots. Imaging and EDAX analysis were also used to select specific target areas for electron probe microanalysis (EPMA) and laser-ablation inductively-coupled plasma mass spectroscopy (LA-ICP-MS).

A CAMECA SX-51 EPMA instrument at Adelaide Microscopy was used to provide quantitative compositional data, mineral stoichiometry and chemical characterisation of zoning patterns in sulphides and gangue minerals. Standards and spectral lines for rock-forming silicates were: Na (albite, $K\alpha$), Mg (almandine, $K\alpha$), Al (almandine, $K\alpha$), Si (almandine, $K\alpha$), P (apatite, $K\alpha$), Cl (tugtupite, $K\alpha$), K (sanidine, $K\alpha$), Ca (apatite, $K\alpha$), Ti (rutile, $K\alpha$), Cr (pyrope, $K\alpha$), Mn (rhodonite, $K\alpha$), Fe (almandine, $K\alpha$) and F (fluorite, $K\alpha$). Standards and spectral lines for ore minerals were: Au (Au metal, $M\alpha$), Ag (Ag_2Se , $L\alpha$), Cu (Cu_2S , $K\alpha$), Zn (ZnS, $K\alpha$), Fe (FeS_2 , $K\alpha$), S (FeS_2 , $K\alpha$), Se (Ag_2Se , $L\alpha$), Co (Co metal, $K\alpha$), Ni (Ni metal, $K\alpha$), As ($AsGa$, $L\alpha$), Cd (CdS , $L\alpha$), Mn (MnS, $K\alpha$), Te (Bi_2Se_3 , $L\alpha$), Pb (PbS , $M\alpha$) and Bi (Bi_2Se_3 , $M\alpha$).

A LA-ICP-MS system located at CODES, University of Tasmania was used to acquire the trace element data for molybdenite. This machine is a 7500 series ICP-MS instrument coupled with a UP-213 laser-ablation system. The following isotopes were measured: ^{57}Fe , ^{59}Co , ^{60}Ni , ^{65}Cu , ^{66}Zn , ^{75}As , ^{77}Se , ^{107}Ag , ^{118}Sn , ^{121}Sb , ^{125}Te , ^{182}W , ^{185}Re , ^{197}Au , ^{204}Pb , ^{207}Bi , ^{238}U , i.e. the same element set as used by Kalleske (2010). In-house standard STDGL2b2 was used for calibration (Danyushevskiy *et al.* 2011). Pre-ablation at 1 Hz was undertaken to clean the surface of contaminants. Sample measurement took place at a laser frequency of 5 Hz and 35 μm spot size. Analysed isotopes were selected to avoid interference from other isotopes with the same weight or a combination of isotopes with the same weight.

In addition to spot analysis, 4 element maps were created using the same instrument (see Large *et al.* 2009 for experimental details). Each mapped a different grain of molybdenite in four samples (NK25, RG10, RG27 and RG45). The maps highlight grain-scale element distributions. Map NK25 was compiled using 15 μm resolution, map RG10 used a 10 μm resolution and maps RG27 and RG45 used an 8 μm resolution with each map taking 3-6 hours to complete. Mapped elements were Al, Si, S, Ca, Fe, Co, Ni, Cu, As, Se, Mo, Ag, Sb, Te, W, Re, Au, Hg, Pb and Bi in all cases.

Focussed Ion Beam – SEM (FIB-SEM) methods were used for high-resolution cross-section imaging of μm and sub- μm -sized inclusions in molybdenite and for extraction and thinning of *in-situ* foils for Transmission Electron Microscopy (TEM). A FEI-Helios

nanoLab DualBeam system at Adelaide Microscopy was used, following methodology described by Ciobanu *et al.* (2011). Standard operating conditions are 30kV for ion milling and 20kV and 5kV for normal and immersion mode imaging, respectively, using the electron beam.

TEM study (electron diffraction and high-resolution) imaging of the FIB-prepared foils was performed on a Philips 200CM TEM instrument (Adelaide Microscopy) operated at 200 kV. The instrument is equipped with a double-tilt holder and Gatan digital camera. Measurements on the diffractions were performed using DigitalMicrograph™ 3.11.1.

RESULTS

Lithologies and alteration assemblages

PETROGRAPHY AND MINERALOGY

At Boddington the mineralisation occurs as disseminations and veinlets throughout several types of magmatic rocks, including diorite, andesite, rhyodacite, dolerite and granite, all with various degrees of alteration. All these rocks, except the granite, are deformed and metamorphosed at lower amphibolite facies (biotite-plagioclase present). The present study was focused on sulphide-rich samples from diorite and granite in the southern part of the deposit. For the sake of comparison, a sample of dolerite with scattered sulphides (RG19) from the same part of the deposit was also analysed. Mineral associations (ore minerals and gangue) in the 53 polished blocks are listed in Table 1 and abbreviations for mineral names throughout the tables and text are given in Table 2.

Diorite is a term attributed to foliated rocks consisting of variable amounts of plagioclase, quartz, biotite and subordinate muscovite. This rock can vary from coarse- to very fine-grained (Figure A10a, b) and in some cases shows extremely sheared mylonitic texture; in the latter the proportion of muscovite increases. Albitisation of diorite is seen throughout large intervals in the lower half (400-900m) of drillcore WBD 105900002. This diorite is characterised by a prominent sheared porphyroblastic texture, in which the porphyroblasts consists of symplectites of quartz and albite.

In contrast, the granite and dolerite are both coarse-grained. The **granite** (Figure A10c) consists of perthitic feldspar (potassium feldspar with exsolutions of albite), plagioclase,

quartz and mica (both biotite and muscovite). In comparison with the diorite, the granite is less altered and the alteration is mostly confined to, or in and around the sulphide patches. A micro-grained aplitic variety occurs at depth (Table 1). The studied **dolerite** is a quartz-bearing variety in which the pyroxene is pseudomorphed by hornblende and Fe-Ti-oxides (Figure A10d, e) and the plagioclase is minor and largely replaced by epidote.

This study focused on alteration assemblages that are tied to (hydrothermal) sulphide deposition, rather than those resulting from metamorphism. Such **alteration assemblages**, seen in both diorite and granite, include actinolite, intermediate members of the clinzoisite-epidote (Clz/Ep) group, biotite, chlorite, albite, K-feldspar (adularia), quartz, stilbite and clay minerals.

Minor components of the alteration assemblages seen in both diorite and granite samples are Fe-Ti-oxides (ilmenite, rutile), titanite, apatite, scheelite, fluorite, thorite and a variety of REE-bearing minerals as well as niobates. Apatite and scheelite are widespread and in some samples very abundant (e.g. RG52, Figure A10f). Among the niobates, fergusonite, $(Y,REE)NbO_4$, is quite common in the granite (Figure A10g) whereas Ca-niobates are present in both granite and diorite. Hochelagaite, $[(Ca,Na,Sr)Nb_4]_{11} \cdot 8H_2O$, was identified in the latter, together with scheelite as dusty inclusions within ilmenite surrounding a core of rutile (Figure A10h, i). Fluorite is more abundant in the granite where it can occur as veinlets together with sulphides; in the diorite fluorite is seen as small patches tied to the sulphides.

It is very difficult to establish specific mineral sequences since all these minerals are ubiquitously present, except for actinolite and stilbite which are much rarer. In most cases, the abovementioned minerals are associated, in variable proportions, with one another. Illustrating the complexity of the alteration assemblages, for example, in a diorite sample (RG52), actinolite was seen filling the inner part of a quartz veinlet with sulphides where the veinlet selvage includes both epidote and biotite (Figure A10j). The most common and abundant alteration mineral, always seen embedding the sulphide patches, is Clz/Ep (Figure A10k, l). This often displays oscillatory zonation patterns seen on the back scatter electron (BSE) images as various shades of grey (Figure A10m). Biotite (Figure A10n) is the second most common alteration mineral and is tied to the sulphide occurrence even though it is difficult to discriminate between different generations of biotite. In diorite, some of the biotite is formed by replacement of mafic minerals (pyroxene/amphibole). In this case it occurs as coarse grains containing abundant inclusions of titanite. In contrast, the hydrothermal biotite (associated with sulphide deposition) forms short lamella packages.

Chlorite is less abundant but nonetheless widespread. Chamosite, the Fe-rich variety, is seen interlayered with muscovite (Figure A10o) - in particular in the granite samples.

A zeolite facies alteration is also present based on the fact that a Ca-rich variety of stilbite has been identified in three diorite samples (RG67, 27, 60). Stilbite occurs either intergrown with molybdenite (Figure A11a), replacing feldspars (Figure A11b, c), or forming veinlets. In the sample from the open pit (RG67) stilbite is found in an intensely-altered diorite featuring high porosity and silica + clay minerals replacement of feldspars (Figure A11d). Hydrothermal biotite interlayered with chlorite (Figure A11e) and overgrown by Clz/Ep (Figure A11f) is also observed in the same rock. These minerals coexist with allanite that contains dusty inclusions of REE-minerals (Figure A11g, h) and rims of thorite (Figure A11i),

Silicate Mineral Chemistry

Electron microprobe analysis was carried out on the rock-forming silicates and alteration assemblages hosting the mineralisation. Results for feldspar, biotite, muscovite, epidote and chlorite are summarised (as means for each sample) in Tables A1-5; means for chlorite are given in Table 3.

FELDSPAR

Plagioclase feldspars from the granite are Na-rich with a narrow compositional variation within the albite ($Ab_{99.1-99.7}$) or oligoclase ($Ab_{82}An_{16}$; RG50) fields. Similarly, the potassium feldspar is close to end-member Kfs showing a narrow variation in all samples except RG50 ($Kfs_{97.6-96.8}$ and $Kfs_{86.6}Ab_{12.8}$, respectively). The compositional spread for the plagioclase feldspars in the diorite is also in the albite-oligoclase range but, unlike in the granite, this variation is observed in each of the analysed samples; a single analysis plots in the andesine field. End-member potassium feldspar has been found in two samples (RG36). The Ab-An-Kfs plots (Figure 2a, b) show there is little difference in terms of compositional variation for plagioclase but the granite has more variation in terms of K-feldspar composition.

BIOTITE

The data for biotite in both granite and diorite shows little variation around an intermediate composition between the Fe-rich (annite) and Mg-rich (phlogopite) end-members ($\text{Ann}_{43-50}\text{Phl}_{47-53}$). A slightly Fe-richer variety ($\text{Ann}_{57.6}$) is present in a granite sample (RG50) and a second population of biotite, a Mg-rich variety ($\text{Phl}_{60.6}$), is observed in a diorite sample (RG29). The biotite has variable but consistent F content in both granite and diorite ranging from 0.5-2.71 wt%, giving fluorophlogopite components in the range 10.8-32.5 mol%.

MUSCOVITE

Muscovite also has little variation throughout the dataset for granite and diorite with a phengite component ranging from 8.5-18.2 mol%. The fluorine content in the muscovite is appreciably lower than in the biotite, ranging from 0.12-0.69 wt%, corresponding to a mol% F-end-member component in the range 1.2-7.4.

EPIDOTE GROUP MINERALS

Data for minerals from the epidote group show the presence of dominantly Al-rich compositions with X_{Al} between 76.4-82.9 mol% and 72.2-86.3 mol% in the granite and diorite, respectively. This indicates that clinozoisite is the mineral in both diorite and granite. The Mn component is minor throughout the dataset (<1 wt%). The compositional plots (Figure 2c, d) show somewhat greater spread among the analyses from granite than those from the diorite. Compositional variation across profiles in individual grains that show oscillatory zonation (Figure A10m) indicate a narrower range of variation than the entire compositional interval with only 6-7 mol% X_{Al} difference across the profile. This means that in a given sample the variation in composition is higher from grain to grain than across the zonation.

CHLORITE

In contrast to the other silicates chlorite shows a wider variation between different samples and from granite to the diorite. One of the granite samples (RG42) is characterised by varieties richest in Fe (94.9 mol% chamosite, the Fe-end-member). Otherwise, the chamosite component in other granite samples ranges from 70.9 to 81.7 mol%. In the diorite, Mg-richer

compositions are noted; Fe/(Fe+Mg+Mn) ranges from 0.38 to 0.78, inferring that both chamosite and clinocllore (Mg end-member) are present. Mn contents are consistently <0.7 wt%. Al^{vi} (octahedral Al) varies from 1.2 to 1.6, with no statistical difference between granite and diorite. In the diorite sample RG27, there are two distinct compositional types of chlorite: one is appreciable richer in Fe (78.5 against 63.5 mol% chamosite) but poorer in Al^{vi} (1.26 against 1.36 a.p.f.u.). This suggests two distinct generations (see below). The ternary Fe-Mg-Al^{vi} plot (Figure 2e) discriminates chamosite in the granite from the intermediate compositions in other samples.

Application of the chlorite geothermometer (Cathelineau 1988, Jowett 1991, De Caritat *et al.* 1993) uses the Al^{iv} (tetrahedral) component in chlorite to derive a peak metamorphic temperature. The calibrations of Cathelineau (1988) and Jowett (1991) are used: for chlorites with Fe/(Fe+Mg+Mn)<0.6, whereas the calibration of Cathelineau (1988) is preferred for the Fe-rich varieties. Realistic temperatures are obtained (Table 3), ranging from 194 to 366 °C in the granite and 219 to 421 °C in the diorite. The two populations in RG27 give temperature estimates at the minimum of the range (219 °C) and towards the upper limit (367 °C), further suggesting these two populations were formed under different conditions. Temperature estimates from individual analyses are also summarised in Figure 2f-h.

Mineralisation

The major components of the Cu-Mo mineralisation at Boddington are chalcopyrite, pyrrhotite and molybdenite. Other sulphides identified here are cubanite, pyrite, sphalerite, stannite, pentlandite, argentopentlandite, a Fe-Ni-thiospinel possibly violarite, Co-mackinawite, bornite, chalcocite and covellite; native copper was also found in one of the samples with zeolite alteration (RG67). The Au mineralisation at Boddington is characterised by an Au-Ag-Bi-(Pb)-Te-(Se) mineral association which includes native gold, electrum, maldonite (Au₂Bi), native bismuth, hessite (Ag₂Te), altaite (PbTe), intermediate members of the galena-clausthalite series (PbS-PbSe), naummanite (Ag₂Se), abundant Bi-tellurides from the tetradyomite group (Cook *et al.* 2007a) and subordinate Bi-Pb-sulphotellurides from the aleksite series (Cook *et al.* 2007b).

PETROGRAPHY AND MINERALOGY OF SULPHIDES

Most commonly, the sulphides occur as narrow veinlets (mm-cm size) or as patches and disseminations (Figure A12). **Chalcopyrite** is often associated with **pyrrhotite** and in some cases with **molybdenite**; the latter however is often found in monomineralic patches of cm- to mm-size. All these minerals are found in both granite and diorite samples. Also common in the two types of rocks is the presence of **sphalerite** where the latter is found as small grains at the boundaries between chalcopyrite and pyrrhotite.

In the diorite the sulphide assemblages are more varied. In many cases pyrrhotite is present as two compositionally distinct species (see below), with lamellar exsolution textures recognisable on the BSE images by the different shades of grey (Figure A12a). Either of the two species can be the host for lamellar exsolutions. **Cubanite**, commonly seen in minor amounts as lamellar exsolution in chalcopyrite, is also the main sulphide in a couple of samples (RG24 and RG59). In sample RG24 cubanite occurs as a fine dissemination along the foliation in the diorite. In many grains, skeletal exsolution of pyrrhotite (Figure A12b), as well as small inclusions of sphalerite and pentlandite are present. In the same sample patches of chalcopyrite/pyrrhotite host grains of **pentlandite** that is compositionally inhomogeneous; **argentopentlandite** (Figure A12c) was identified within such grains. In sample RG59 the cubanite contains fields of tiny exsolutions of **stannite** + sphalerite (Figure A12d). Coarser inclusions of sphalerite and stannite (up to several microns; Figure A12e) also occur either throughout the cubanite or at the margin between cubanite and pyrrhotite. The association stannite+sphalerite is also found coexisting with pyrrhotite in a sample where chalcopyrite is the main copper sulphide (RG27; Figure A12f).

Pyrite is rare and is found either coexisting with (RG59) or without pyrrhotite (RG17). In the latter case, however, lamellar textures are observed indicating replacement of pre-existing pyrrhotite. In the dolerite, pyrite is the main sulphide and contains rounded inclusions of chalcopyrite. Cobalt-nickel minerals are represented by **Co-mackinawite** (RG11; Figure A12g) and **Fe-Ni-thiospinel** (RG36, RG59). These were identified from two samples in associations containing pyrrhotite; in RG59, it also coexists with pyrite. In sample RG59, the thiospinel occurs as unusual intergrowths with (REE-bearing) (bastnäsite) (Figure A12h-j).

Apart from chalcopyrite, very minor amounts of other Cu-(Fe)-sulphides (bornite, covellite, chalcocite) are found in two samples. **Bornite** and **covellite** (Figure A12k) are seen along thin veinlets or grain boundaries of chalcopyrite where some of the grains contain

lamellar cubanite (RG25). Several grains of **chalcocite** (Figure A12l) occur in association with **native copper** (Figure A12m) in a sample from the open pit containing zeolite alteration (RG67). Native copper is quite abundant in this sample where is present as visible disseminations and thin veinlets or staining the rock surfaces. Some of the grains occur as inclusions in epidote or stilbite; in former case they have a narrow rim with clay minerals.

MOLYBDENITE

Molybdenite is present in 24 samples, a third of which are from the granite. In the majority of cases, it is associated with chalcopyrite and pyrrhotite. It displays great morphological variety from bundles and knots to lamellar aggregates along the foliation or single lamella scattered in the surroundings of the larger patches (Figure 3). It is commonly coarse-grained with contorted and kink deformation lamellae (Figure 3a-c). In some samples, however such coarse aggregates coexist with meshes formed by shorter lamellae (RG64, Figure 3d) and also aggregates of idiomorphic short lamellae.

In the present sample suite a conspicuous feature of the molybdenite is the presence of inclusions (up to several microns; Figure 3e) of different minerals (see also next section). In molybdenite from both granite and diorite Bi-tellurides from the tetradymite group are abundant; galena and hessite are also noted. Phases from the aleksite series are present in the granite whereas chalcopyrite, native gold, electrum, native bismuth and minor altaite are seen in the diorite.

The molybdenite in the granite displays regular, dense fields of telluride inclusions. In the diorite, however, chalcopyrite inclusions are regular and dense (Figure 3f). In the latter case all other inclusions, including tellurides, have an irregular distribution and range in abundance from scattered to very dense in certain areas. In both cases the inclusions are seen preferentially along the molybdenite lamellae with a tendency to coarsening across intervals of kink deformation or in the axial plane of tight microfolds (Figure 3g, h). Ductile remobilisation of inclusions is also observed along microshears oblique to the molybdenite lamellae (Figure 3i). The thicker chalcopyrite inclusions display pointing edges indicating they are formed under stress conditions (Figure 3f).

Sulphide Mineral Chemistry

Compositional variation in the sulphides was measured using EPMA. Results are presented in terms of means and standard deviation for each sample or distinct populations in a given sample in Tables 4-7 and Table A6 in Appendix.

Pyrrhotite, Fe_{1-x}S , where $0 < x < 0.125$, is an interesting mineral group both in geological and crystallographic terms. The pyrrhotite structures have hexagonal close packed (hcp) layers of S with Fe atoms occupying octahedral interstices between the S layers. All octahedral positions are occupied in troilite (FeS ; hexagonal), whereas the non-stoichiometric pyrrhotites have vacancies on the Fe positions (Posfai & Buseck 1997). The most common forms in nature are monoclinic 4C pyrrhotite (ideally Fe_7S_8) and hexagonal 5C pyrrhotite (ideally Fe_9S_{10}) (Becker *et al.* 2010).

The EPMA data shows distinct compositions for Po in the granite relative to the diorite and also distinct compositional fields for the 2-phase Po with lamellar exsolution textures identified on BSE images (Figure A12a) in diorite (Table 4). Compositional variation is expressed as M/S, where $M = \text{Fe} + \text{Co} + \text{Ni} + \text{Cu}$, ranging from 0.98 to 0.87 in terms of mean values. Nickel is present in highest amounts (means of 0.19 and 0.2 wt%) in the dark lamellae from RG52 and RG24 and is detectable (means of 0.05 and 0.09 wt%) in 2 other samples, one of which is the single phase Po (RG27). Cobalt is present in detectable amounts only in 2 samples, both from the single phase Po, one from the granite (RG48) and one from the diorite (RG66). Copper is detectable in a majority of the samples with mean values between 0.25 and 0.07 wt%.

The plot of M versus S shows that the single phase Po corresponds to the Fe_7S_8 field in the granite and spreads into the field of Fe_9S_{10} for single phase Po in the diorite (Figure 5a, b). About a third of the Po in the granite analyses plot in a field with still lower M, which is difficult to explain unless we consider that the Po is replaced by Py and the latter is not observable on the BSE images (submicroscopic grain replacement). There is a clear compositional gap between the ‘dark’ (showing a wide spread across Fe_7S_8 to $\text{Fe}_{10}\text{S}_{11}$) and ‘bright’ lamellae (towards the upper limit of stoichiometric FeS) from the 2-phase Po in the diorite (Figure 5c).

Sphalerite (Table 5) from both diorite and granite samples is rich in Fe, with mol% FeS in the range between 14.23 (RG48) and 20.67 (RG24). Detectable amounts of Cd were found in all samples (means from 0.22 wt% in RG27 to 1.16 wt% in RG48). Copper is also present in

the majority of samples with mean values between 0.27 wt% (RG66) and 1.72 wt% (R59). **Stannite**, present together with sphalerite in 2 diorite samples shows variable Fe:Zn ration from 1.624:0.376 to 1.905:0.103 in samples RG59 and RG27, respectively.

Co-existing Sph-Stn pairs were used to calculate formation temperatures based on equilibrium $\log X_{\text{FeS}}/X_{\text{ZnS}}$ ratios in the two minerals (Table 5) following the calibration of Shimizu & Shikazono (1985). Even though the Stn grains are relatively small to ensure accurate measurements, the geothermometer gave realistic temperatures of ~350 °C a cluster of points (Figure 5d).

Pyrite was measured in one sample (RG18, Table A6) and shows detectable amounts of Co and Ni (means 0.08 and 0.04 wt%, respectively). Although As was not measured, the good totals indicate that, if present, it is only present at very minor levels, concordant with pyrite data given in Kalleske (2010). **Pentlandite** shows stoichiometric composition whereas **argentopentlandite** is slightly metal deficient, probably due to analytical error brought in by the small grain size (Table A6). Copper is present in both minerals (means 1.19 and 2.17 wt%, respectively); mean Co contents are 4.68 and 0.19 wt% in Pn and Ag-Pn, respectively. Two different Co-Ni-bearing varieties of stoichiometric (M:S=1) **mackinawite** are present (Table A6). The **Fe-Ni thiospinel phase** (Wagner & Cook 1999) gives compositions along the Fe_3S_4 (greigite) – Ni_3S_4 (polydymite) join, but conspicuously closer to Fe_2NiS_4 than the named mineral FeNi_2S_4 (violarite).

AU-AG-BI-PB-TE-SE ASSOCIATION

Gold and silver minerals (native gold, electrum, maldonite and hessite; Table 6) as well as tellurides (Figure 4) were found in the diorite samples, both as inclusions within molybdenite and as clusters of minute grains (up to 10 microns) in the alteration assemblages surrounding the sulphides; the latter type of occurrence is also present in the granite. Even though native gold and electrum are present in larger amounts as monomineralic filaments or small droplets/patches (RG60, RG62) (Figure 4a, b), these are also observed together with Bi- and Pb-tellurides (RG25; Figure 4c) within molybdenite from the diorite.

The genetic link between gold and bismuth minerals is clearly seen in the presence of crystallised droplets containing the assemblage maldonite + hedleyite + bismuth (RG52, Figure 4d), an association representing the equivalent of the eutectic at 235 °C in the Au-Bi-

Te system (Prince *et al.* 1990) Such an association is part of the larger clusters including native gold, native bismuth, hessite and several Bi-tellurides from the Bi-rich end of the tetradymite group (Figure 4e, f). These clusters are tied to local brecciation and chloritisation superimposed onto an earlier alteration assemblage, e.g. actinolite-quartz-epidote in RG52. Hessite is always associated with native bismuth \pm bismuth tellurides and is relatively widespread as inclusions in either molybdenite, other sulphides or in the gangue (Figure 4g-i).

The bismuth tellurides (Table 7) found in molybdenite are either tsumoite or species with ratios of Bi/Te > 1 (including several unnamed species) in the granite (Figure 4j) and diorite, respectively. Several tellurosulphides from the aleksite series (saddlebackite, aleksite and phase 'C'; see below) were found in the molybdenite from the granite. Variation in the sulphur content is observed in the Bi-tellurides occurring within molybdenite but not in those from the outside clusters.

Other tellurides and selenides identified by EDAX analysis include altaite (Figure 4k), clausenthalite, ikunolite (Figure 4l), laitakarite and naummanite.

Trace Element Chemistry of Molybdenite (LA-ICP-MS data)

Molybdenite from 19 samples was analysed using LA-ICP-MS to determine trace element concentrations. The sample selection comprises 6 granite and 13 diorite samples, of which one was a sample from the ABreccia orebody (NK25) from the Kalleske (2010) sample suite. 250 individual spot analyses were carried out. Results are summarised as means, standard deviations, minima and maxima for each sample in Table 8; the full dataset is listed in Table A7, Appendix.

ELEMENT SPECTRA AND CONCENTRATIONS

In molybdenite from both diorite and granite, some elements, e.g. Re, W and Se, show flat signals on the time-resolved spectra. Most chalcophile elements (Bi, Te, Ag, Pb) and Au typically display irregular signals during spectra acquisition. Representative spectra for both diorite and granite are shown in Figure 6.

Rhenium concentrations in molybdenite from diorite (expressed as mean within an individual sample) vary across 4 orders of magnitude, from <1 (0.16; RG29) to 374 ppm

(NK25). Mean values of several hundred ppm Re were all obtained from samples from the open pit (NK25, RG8, RG10) and one sample from the drillcores gives a mean of tens of ppm Re (36 ppm; RG64). All other samples had mean Re concentrations of $\ll 10$ ppm. The range of Re concentrations in individual spot analyses across the diorite sample suite is 0.03 ppm (RG29, RG30) to 905 ppm (NK25). In terms of variation within a single sample, the highest variation is seen in one sample (RG64), which shows a range over 3 orders of magnitude. All samples from the open pit show the least intra-sample variation. Results obtained on samples from the open pit in the Central Diorite are comparable in terms of Re concentration with some of the highest concentrations obtained in the ABreccia orebody sample at a difference in depths of ~42 m. Maximum values of hundreds of ppm Re are also recorded from some of the drillcore samples that intersect mineralisation ~200 m below, e.g. 347 and 218 ppm for RG27 and RG64, respectively. In contrast with the diorite, molybdenite from granite has means Re concentrations that are consistently low (0.4 to 18 ppm).

Mean concentrations of W in molybdenite from diorite samples show a range from 79 to 306 ppm. The range of W values within each diorite sample is low, although one sample from the open pit (RG10) displays a variation up to 2 orders of magnitude. Mean W concentrations in the granite samples show a spread from 69 to 206 ppm. Tungsten variation in the granite is low with all samples showing a range of no more than one order of magnitude.

Mean Au concentrations in molybdenite from the diorite range from 9.4 (RG27) to 116 ppm (RG30), with a maximum value of 1,110 and a minimum value of 0.01 ppm. The highest variation within a single sample is 4 orders of magnitude (RG30 and RG65). Variation is, in general, always greater than one order of magnitude. Although comparably higher mean Au concentrations and maximum values are obtained for the two samples from Central Diorite in the open pit than in drillcores at depth, there is a suggestion that the shallower samples are poorer in Au than the deeper ones. In addition, shallower samples from the Central Diorite have a higher spread in Au values than that of the ABreccia. The mean Au concentrations in molybdenite from granite varied between 0.01 and 11 ppm, with 4 of the 6 samples having all values $< \text{mdl}$ and an individual maximum value of only 53 ppm (RG40).

Mean Ag concentrations in molybdenite from the diorite range from 2.2 to 96 ppm. The range in variation in Ag is high (up to 4 orders of magnitude; RG65). In the granite, Ag means range between 1.3 and 32 ppm.

Means for Te in molybdenite from the diorite vary between 46 and 865 ppm with individual values of 20-3,912 ppm. The variability in Te concentration within each sample is low (up to 2 orders of magnitude). The range of variation for Te means in the granite is between 36 and 5,093 ppm (maxima and minima are 35,599 and 8.0 ppm, respectively). Two of the 6 samples (RG49, RG51) have much lower Te concentration (tens of ppm) in comparison with the other 4 which show hundreds or thousands of ppm Te. These granite samples are slightly finer-grained than the other 4.

Mean Bi concentrations in molybdenite from the diorite show variation between 113 and 2,929 ppm (RG25, RG27) with maxima of 12,108 ppm and minima of 1.3 ppm (RG25, RG29, respectively). Bi values in the diorite samples display greater variation than Te (up to 3 orders of magnitude). In granite molybdenite, Bi shows a still higher range of variation; mean concentrations are from 32 to 7,885, with the maximum (52,682) and minimum (0.02 ppm) concentrations in molybdenite from the same samples (RG45, RG51). The highest variation in a single sample is up to 5 orders of magnitude (RG40). The lowest Bi concentrations are recorded in the fine-grained granite samples.

Mean Pb concentrations in molybdenite from the diorite ranges from 57 (RG62) to 1,532 ppm (RG25), with a maximum individual value of 3,440 and a minimum of 0.28 ppm. The range of Pb concentration in each sample shows a high variation (up to 3 orders of magnitude; RG29 and RG64). Mean Pb concentrations for molybdenite in the granite show variation between 146 (RG51) and 4,774 ppm (RG45). Variation within individual samples is high (up to 3 orders of magnitude).

Selenium concentrations in molybdenite from the diorite show a range from 311 to 1,149 ppm, with a maximum value of 1,543 ppm and minimum of 268 ppm. Molybdenite in the granite has mean Se concentrations that range from 205 to 444 ppm. Unlike most other elements, Se has a low variance within each sample in both diorite and granite.

Detectable concentrations of Co and Ni are recorded in molybdenite from the diorite. Mean concentrations are 0.85-14 ppm and 2.2-53 ppm for Co and Ni, respectively. In molybdenite from the granite, Co and Ni concentrations are extremely low (0.44-3.0 ppm and 0.06-0.27 ppm, respectively).

Mean Fe concentrations in molybdenite from the diorite lie in the range 1,390–26,853 ppm (samples RG60 and RG25, respectively). Samples from the granite show mean

concentrations of 420-5,549 for Fe in molybdenite. Variance within individual samples is high in both rock types (up to 3 orders of magnitude).

Copper is present at detectable concentrations (means 15-1,261 ppm in the diorite and 2.1-400 ppm in the granite). Overall the diorite samples have higher Cu concentrations in molybdenite than the granite. Detectable amounts of several other elements (Zn, As, Sn, Sb, Tl and U) are also recorded in the analysed molybdenites and in some samples show somewhat higher values.

HISTOGRAMS

The distribution of trace elements in molybdenite from both diorite and granite is expressed in histograms (Figure 7). Elements which are commonly incorporated within the molybdenite structure (i.e. Re and W) show contrary distribution patterns in molybdenite from the two rock types. The rhenium distribution is bimodal and W shows a normal distribution in diorite, but in granite Re is normally distributed and W is bimodal (Figure 7a, b). The population from molybdenite in granite overlaps with the low-concentration population in the diorite for Re. Histograms for Au and Ag in molybdenite from both granite and diorite show normal distributions (Figure 7c, d). The distribution of Au is however positively skewed for diorite with granite in the lower concentration range. Silver shows the best similarity between the population in the diorite and granite. The 3 chalcophile elements (Bi, Te, Pb) associated with Au and Ag (see section above) show broadly normal distributions in the entire dataset (Figure 7e-g) although there is a slight positive skew towards higher concentrations in the Bi and Pb populations. In the granite population there is a bimodal tendency for all 3 elements, best expressed for Te, largely due to the fact that molybdenite in the fine-grained granite is characterised by lower concentrations of these elements (see above).

VARIATION TRENDS

Plots of element concentration in molybdenite against depth (Figure 8) are illustrative of the spread in variation across the depth interval sampled in the Central Diorite (~250 m) and in relation to the sample from ABreccia (42 m above). Rhenium shows a slight decreasing trend and a wide variation with depth (Figure 8a). The wide variation is seen in those diorite samples that overlap with the granite depth. In contrast, W shows no apparent trend or range of variation with depth (Figure 8b). Gold shows a wider variation at depth but indication of a

decreasing trend with depth if the 2 fine-grained granite samples that record the lowermost values (<0.1 ppm) are included (Figure 8c). Silver shows no trend but a wider range of variation with increasing depth (Figure 8d); in this case the fine- and coarse-grained granite samples have comparable ranges of variation in Ag concentration. A clear increasing trend and wider spread of variation with depth is seen for Te, whereas both Bi and Pb show comparable wide ranges of variation but no trends with depth (Figure 8e-g). For all three elements the highest values and widest ranges are in molybdenite from the granite but the finer-grained granite variety records the lowermost concentrations in each case. For Pb there is, however, an overlap in the range of values with those of the coarse-grained granite.

Binary plots of Au against chalcophile elements (Figure 9a-c) display much higher correlation coefficients for molybdenite from diorite ($r^2=0.79$ for Au-Bi; $r^2=0.65$ for Au-Te; $r^2=0.69$ for Au-Pb) than the granite ($r^2\sim 0.50$ for Au-Bi, Au-Te, Au-Pb). The Au-Ag plot (Figure 9d) is, however, an exception in that the trends are parallel ($r^2=0.64$) for the 2 sample groups. A strong distinction is seen in the correlation plot between Ni and Co (Figure 9e), where the correlation coefficient for the diorite population ($r^2=0.91$) is much higher than that for the granite population ($r^2=0.38$). The plot of Re versus W shows a funnel-shaped distribution where the highest Re values (in diorite) record the highest spread in W and this spread narrows down to intermediate Re values (in granite) and further to the lowest Re values (in other diorite samples) (Figure 9f). The plot for Au versus Re (Figure 9g) shows that the diorite has the highest values in Au over a wide range of Re and that the analyses from granite cluster within a distinct field with the lowermost values for both Re and Au.

GRAIN SCALE INHOMOGENEITY

In molybdenite from the diorite the spot analyses demonstrate a high degree of grain-scale inhomogeneity (Figure 10). This depends, to some extent, upon textures such as bending, kink deformation, grain boundaries and replacement by silicates or other sulphides such as chalcopyrite. For example, spot analyses taken along a trajectory following apexes of bends in molybdenite lamellae from sample RG10 show relatively constant, high Re concentrations (hundreds of ppm) and constant Au concentrations (tens of ppm) (Figure 10a). In another case typifying the same type of texture (sample RG27), an inverse trend of variation is seen for the two elements, when comparing values from one spot to another i.e. consistently hundreds of ppm Re but an order of magnitude variation in Au (Figure 10b). In the same sample, in areas where there is replacement along molybdenite lamellae by chalcopyrite,

spots located on the apex of a kink show values of Re in the lower range for this sample (a few ppm) but Au values are in the upper range (tens of ppm) (Figure 10c).

An interesting case is seen in sample RG64, where coarse molybdenite coexists with packages of idiomorphic short molybdenite lamellae. In the former type, Re concentrations are lowest (a few ppm) but Au is highest (tens of ppm) (Figure 10d). In the latter type, however, the opposite is seen. Rhenium records the highest values (hundreds of ppm) but Au is at most a few ppm (Figure 10e). In the same sample, inhomogeneity throughout packages of short lamellae that display slight deformation show variation in Au content over 2 orders of magnitude, from few to a hundred ppm (Figure 10f). The highest concentration of Au in the diorite samples (Figure 10g) was recorded along grain boundaries where particle nucleation takes place, explaining the highly irregular Au signal across the time-resolved downhole spectra. In some cases, increases in Au concentration (up to tens of ppm) are also observed along the axes of kink folds (Figure 10h). In another sample (RG62), Au in the same textural context is only few ppm (RG56, Figure 10i), but increases to tens of ppm in the apexes of tight microfolds (Figure 10j).

Variability of Re and Au concentration depending upon comparable microscale textures is seen in molybdenite from the granite samples, even though the overall values are much lower than in the diorite. In the granite, trace element inhomogeneity in molybdenite is much more strongly expressed in terms of Te, Bi, Pb variation, and to some extent also of W, rather than Re and Au (Figure 10k).

LA-ICP-MS MAPPING OF MOLYBDENITE

LA-ICP-MS element mapping was carried out on 4 samples, 3 from the diorite (RG27, RG10, NK25; Figure 11, A13, A14, respectively) and 1 from the granite (RG45; Figure 12), to better understand the observed correlation between textures, inclusion distribution and grain scale inhomogeneity obtained from spot analysis in the molybdenite.

Sample RG27 (Figure 11) represents the case of molybdenite in diorite where replacement of Cp and Clz takes place along the lamellar boundaries. An area with small kink deformation was also included. Native Bi is also observed as tiny inclusions. This is one of the diorite samples where wider variation was recorded for Re with upper values of several hundred ppm (Table A7b). The elemental maps show broadly similar distribution for Re and W with enrichment overlapping the Cp inclusions. Strong enrichment of Re is observed in the

kink area. Bismuth and Pb are higher than Te and seems to be concentrated within the lamellar rather than towards the Cp inclusions.

Sample RG10 (Figure A7) typifies molybdenite with consistently high Re concentration in the South Open Pit. Inclusions of Bi and Bi-tellurides are present. The map area is over a coarse lamella with a tight micro-fold on one side and silicate replacement on the other side. Rhenium shows high, pervasively concentration throughout the entire molybdenite. The micro-fold is marked by highest concentration whereas depletion in Re is observed through the middle of the lamella on the side with silicate replacement. Tungsten shows an inverse trend to Re with clear depletion in the coarser molybdenite lamella with highest concentration on the lamella boundaries as well as in the fold axis. Tellurium, Bi and Pb express very similar patterns with spots of highest concentration along the lamella in the micro-fold and also in the oblique alignment; such spots indicate sites for sub-micron particle nucleation. Gold and silver show very similar trends with the 3 chalcophile elements above even though at much lower concentration.

Sample NK25 (Figure A14) is representative for coarse-grained, highly deformed molybdenite with consistently high Re concentration in the diorite from the North Open Pit (ABreccia). Careful re-examination of the sample has shown the presence of minute inclusions of Au in the molybdenite. Rhenium and W show inverse patterns with trends of Re depletion and W concentration with the deformation. Bismuth and Pb are higher than Te and they broadly show a similar pattern with W, re-emphasising that deformation controls trace element distribution. Similar trends observed for Au and Ag even though in this case the concentration is much lower. It is interesting to note that Se shows comparable trends with Re.

Sample RG45 (Figure 12) is representative of the coarse molybdenite in the granite where the abundance of Bi-(Pb)-tellurides is greatest. The selected area includes 2 sets of kink-bends on each side; replacement of silicates strongly marks the kink-bends. Slight deformation oblique to lamella orientation is also seen on the optical microscopic image (Figure 10k). Rhenium shows zonation with strong enrichment in the areas with the kink-bends relative to the middle part of the mapping area. In contrast W only shows strong enrichment along the kink bends and also along the oblique deformation. Lead, Bi and Te show high concentration with similar pattern to the W, strongly suggesting the relationship between textures and trace element concentration. Notably, Au show spot concentrations

overlapping the chalcophile elements enrichment despite the fact that the measured Au values in the sample are at best a few ppm.

CRYSTAL-STRUCTURE AND NANOSCALE CHARACTERISATION OF MOLYBDENITE AND BI-(PB)-TELLURIDES (FIB-TEM DATA)

Molybdenite occurs as 2 different polytypes: hexagonal (2H) and rhombohedral (3R) of which the first type is the most common in nature. Newberry (1979a, b) stipulated that there should be a correlation between the crystal structure and the amount of minor/trace elements incorporated since 3R molybdenite has a wider *c* parameter than 2H molybdenite (18 and 12 Å, respectively). This assumption was based on the fact that many natural molybdenites appear to be rich in a range of trace elements including Te, Bi, Pb, Re, W. For one such molybdenite, from Whipstick (NSW, Australia), Plimer (1974) concluded that the Mo-Au-Bi breccias in this deposit were zoned in terms of molybdenite polytypes, with the 2H polytype in inner parts and the 3R polytype dominating in the halo.

The petrographical, mineralogical and trace element distribution in molybdenite indicates that Boddington represents an ideal case to test Newberry's hypothesis. The high degree of inhomogeneity in terms of trace element distribution observed from both LA-ICP-MS spot analyses and element mapping suggests the widespread presence of sub-microscopic inclusions, including Bi-(Pb)-tellurides, in all cases. High Au and Ag contents of both overlapping Bi-Pb-Te zones on the element maps and the strong correlation between the precious metals and these chalcophile elements suggest that underlying controlling factors operate at the sub-microscopic scale. Therefore, in order to understand the reasons for such correlation at the sub-microscopic scale, and whether this is controlled by crystal-structural modification in the host molybdenite, a TEM study that addresses these issues at the grain-scale was considered necessary. This is now possible by using FIB-SEM methods for TEM sample preparation (Figure A15). The technique offers the advantage that TEM foils can be obtained in-situ, from specific sites where the sample shows compositional variation and the presence of inclusions (Ciobanu *et al.* 2011).

The main target was molybdenite from one granite sample (RG45) that contained abundant inclusions of phases from both the tetradymite group and aleksite series. A diorite sample (RG62) containing Bi-telluride inclusions within molybdenite was also studied. Four TEM foils were obtained from the molybdenite in the granite sample and one from the diorite

(Figure A16). High-resolution FIB imaging during slice cutting shows that sub-microscopic inclusions of tellurides are always present adjacent to the larger telluride inclusions; abundant kink-bending, high porosity and sub-micron inclusions were observed in the molybdenite (Figure 13a-c; Figure A16b-e, i, j, m, n).

Bright-field (BF) HR-TEM imaging shows that the telluride inclusions and porosity are present down to the nm-scale (Figure 13d-j). Lattice fringes with distortions closing in towards the pores are also a common feature (Figure 13k, l). Lattice fringes and electron diffraction patterns (EDPs) of the molybdenite from all 5 TEM foils indicate only the presence of the 2H polytype (Figure 13m and inset). EDPs obtained from boundaries between molybdenite and telluride inclusions show coherent intergrowths between the 2 minerals with preferential orientation along the c^* axis (Figure 13d inset). Tiny inclusions of Gn were also identified from EDP (Figure 13g inset).

Bismuth-tellurides (-selenides, -tellurosulphides and -telluroselenides) comprising the homologous tetradymite group (Cook *et al.* 2007a, Ciobanu *et al.* 2009a) and the ‘aleksite’ series (Cook *et al.* 2007b) are mixed-layer compounds with rhombohedral or trigonal symmetry. They are derived from the same 5-layer module (X-Bi-X-Bi-X; X=Te, Se, S), known as the ‘tetradymite archetype’ ($a=4.25 \text{ \AA}$; $c=29.6 \text{ \AA}$), by incremental addition of Bi-Bi and M-X (M=Pb, Bi), respectively.

Ciobanu *et al.* (2009a) show that all phases are N-fold superstructures (N= total number of layers in the unit cell) of a rhombohedral subcell and that homology is underpinned by the structural formula $S'(Bi_{2k}X_3) \cdot L'(Bi_{2(k+1)}X_3)$, where X = chalcogen and S' and L' are the number of short and long modules, respectively. Phases from the aleksite series are isoconfigurational with those of the tetradymite group and have the general formula: M_pX_{p+1} ; $p \geq 2$; homology is given by the structural formula: $S(M_pX_{p+1}) \cdot L(M_{p+1}X_{p+2})$; S, L = numbers of short and long modules. The only named minerals in the aleksite series are: aleksite ($Bi_2PbTe_2S_2$) and saddlebackite ($Bi_2Pb_2Te_2S_3$; Clarke 1997), with $p=3$ and 4, respectively. Crystal-structure in each of these minerals is built by a single type of layer, i.e. 7-atom layer: S-Bi-Te-Pb-Te-Bi-S and 9-atom layer: S-Bi-Te-Pb-Te-Pb-S-Bi-S, respectively. Unnamed ‘phase C’ ($Bi_4PbTe_5S_2$; Cook *et al.* 2007b) identified here by EPMA has a structure built by a stacking sequence where 5- and 7-atom layers alternate.

Homology implies that the mineral-chemistry and structure are related closely to one another so that the stacking sequences can be calculated from either the chemical composition or from electron diffraction patterns (Ciobanu *et al.* 2009a). The small grain size

and inherent fine-scale intergrown nature of minerals from homologous series hamper accurate EPMA measurements. Thus, assessment of stacking sequences using EDPs is necessary given the importance of the 'k' or 'p' factors in establishing equilibrium in multi-phase assemblages. At equilibrium k or p factors in the formulae of the component phases must be consecutive, e.g. joséite-B ($\text{Bi}_4\text{Te}_2\text{S}$) and hedleyite (Bi_7Te_3), where $k=2$ and 3 , respectively, can coexist at equilibrium, whereas tetradymite ($\text{Bi}_2\text{Te}_2\text{S}$; $k=1$) and hedleyite ($k=3$) cannot.

Based on empirical observations on a large number of occurrences, assemblages from the tetradymite group reflect the reduced/oxidised character of the mineral association (Ciobanu *et al.* 2005, Cook *et al.* 2009). Phases with $\text{Bi:X} > 1$ indicate reduced conditions (pyrrhotite- or magnetite-stable) and coexist with native bismuth, maldonite. In contrast, phases with $\text{Bi:X} < 1$ are found in oxidised associations (pyrite- or hematite-stable), coexisting with native tellurium and Au-tellurides. Thermodynamic modelling for the stability of native elements, Au- and main Fe-minerals in $f\text{S}_2$ - $f\text{O}_2$ space at $300\text{ }^\circ\text{C}$ also support the above (Cook *et al.* 2009).

Stacking sequences corresponding to Bi-tellurides present as inclusions in molybdenite were interpreted using EDPs following the method of Ciobanu *et al.* (2009a) (Figure 14). The Bi-telluride identified from the diorite is Bi_4X_3 (Figure 14a, h). The EDPs confirm the EPMA data for the dominant telluride in the granite as tsumoite; slight stacking disorder is indicated from both EDP's and BF HR-TEM images (Figure 14b, c). The EDPs obtained from foil 4 on an area with inclusions from the aleksite series indicate a higher-order phase. Stacking sequences interpreted from the EDPs indicate alternating 11- and 13-atom layers corresponding to composition $\text{Bi}_2\text{Pb}_7\text{Te}_4\text{S}_9$, an unnamed phase in the aleksite series (Figure 14d-g, j). The observed lattice fringes support this interpretation (Figure 14f). Disorder is observed on both EDPs and lattice fringes obtained for the unnamed phase (Figure 14e, g, j), as well as for tsumoite (Figure 14c). The domains of disorder observed in both cases comprise combination of layers with consecutive p or k, respectively, indicating crystallisation under equilibrium. This infers that the studied telluride inclusions embedded within molybdenite are not affected by an overprint inducing disequilibrium.

DISCUSSION

Previous work

The Boddington deposit was first considered as an Archean porphyry-style Cu-Mo deposit based on fluid inclusion evidence (high-salinity ore fluids; Roth & Anderson 1993). This hypothesis was refuted by Cassidy *et al.* (1998) based on the lack of similarity between whole rock geochemistry of the diorite relative to diorites with associated porphyry-style mineralisation worldwide. An orogenic style of Au deposit is interpreted by Allibone *et al.* (1998) based on the strong structural control and the presence of high-grade Au in shear zones (e.g. 'Jarrah' bonanza ore along the South-East shear zone).

Stein *et al.* (2001) provide Re-Os dating of Boddington molybdenite and discuss a two-stage model of Au mineralisation: (i) porphyry Cu-Au-Mo (2707 ± 17 Ma), (ii) orogenic Au (2623 ± 9 Ma). Even though description of the samples giving the later date correspond to the granite as described here, i.e. "coarse-grained intervals of cloudy Qz, perthitic feldspar, Mu and Bt", the age is attributed to an orogenic event based on both the low Re content and by similarity with orogenic Au mineralisation in the Yilgarn Craton. The error on the second age overlaps with SHRIMP U-Pb zircon dating of the granite (2611 ± 3 Ma; Allibone *et al.* 1998). Attribution of the first date to the porphyry event is favoured by the high Re-concentration, comparable with porphyry-style mineralisation elsewhere. McCuaig *et al.* (2001) chose to interpret the second Re-Os age in terms of an intrusion-related Au-Mo model rather than orogenic Au.

This intrusion-related Au model is reinforced by Duuring *et al.* (2007), based on the typical Bi-signature present at Boddington - a key factor in this class of deposits (e.g. Lang *et al.* 2000, Hart 2007). Hagemann *et al.* (2007) also support an intrusion-related Au model based on the high Bi and W measured in melt inclusions from granite. These authors consider the granite (with affinities to A- or fractionated I-type, unusual for Archean granitoids in the Yilgarn Craton) to be an important Au-Cu-Mo metal source and a good exploration model for the Boddington area.

Kalleske (2010) acknowledges the multi-stage character of mineralisation in which a pre-existing Cu-Mo-Au mineralisation is attributed to mafic rocks (diorite) and an inferred porphyry-style mineralisation. The Au-Bi-Te association is recognised not only in mineralogical terms but also discussed in terms of overprinting during metamorphism and

granite emplacement The novelty of this work was that it raised the question of why molybdenite from the diorite and the granite have different trace element signatures (the granite is much poorer in Re and Au) and whether these data could help validate a genetic model for Boddington. The Au-Bi-Te signature and reduced character of the ore assemblages led Kalleske (2010) to suggest that an intrusion-related model could not be ignored, despite the fact that only modest values of chalcophile elements were measured in molybdenite from granite (fine-grained aplitic variety).

The present study brings in a consistent package of new data concerning ore stages, formation temperatures, remobilisation and Au deposition in the Central Diorite together with new mineral chemistry data for molybdenite-dominant mineralisation within the granite.

Stages of mineralisation

The main ore assemblages and alteration in diorite and granite share similarities but also differ in several aspects. Among the similarities are: (i) the ore is defined by the assemblage $Cp+Po\pm Mo\pm Sph$; (ii) Bi-(Pb)-tellurides present in both molybdenite and altered country rock; (iii) a reduced character for the sulphide assemblage (Po stable, high Fe-content in Sph) and telluride association ($Bi\geq Te$); (iv) clinozoisite is the main alteration mineral associated with the ore. Notable differences are: (i) a generation of sulphides that clearly pre-date the granite (the difference in Po composition, Cub present in the diorite but not the granite; the bimodal distribution of Re and Au concentrations in molybdenite in diorite and the difference in the Ni-Co signature of molybdenite from diorite and the granite); (ii) the absence of any visible Au in the granite; (iii) the low degree of alteration of the granite relative to that of the diorite; and (iv) that chamosite (Fe-rich chlorite) is present only in the granite.

This summary highlights that at Boddington there are at least 2 main ore stages (A) relating to host diorite and (B) formed during emplacement of granite. The similarity in the main sulphide and alteration assemblages, as well as the reducing character indicate that the metals and the fluids involved in both mineralising stages have either undergone a similar mechanism of ore deposition or that a strong superposition or obliteration occurred during granite emplacement.

Metamorphism and hydrothermal alteration

Actinolite was recognised as an important component of alteration assemblages by Kalleske (2010). In the present study, however, it is scarce, a fact that can be at least partially attributed to replacement by Clz. In the Central Diorite and the granite there is a strong association between ore and Clz which could be indicative of redox reactions controlling metal precipitation during fluid-rock interaction. Such reactions would also favour crystallisation of molybdenite which is considered to be facilitated by reduction of Mo^{6+} (the species considered for hydrothermal transport) to Mo^{4+} (e.g. Stein *et al.* 2003).

Whereas Clz is part of the Ab/Olig+Qz+Bt±Mu/Chl alteration compatible with low amphibolite facies metamorphism, there is evidence of superimposed greenschist facies (Chl+Mu+Qz+Ab) alteration in both diorite and the granite (e.g. Cham+Mu→Bt). This is more pronounced towards depth and probably relates to the granite contact aureole. The lowest temperature type of alteration (zeolite facies, Stb+Qz+clay minerals) is attributable to localised action of faults. The presence of native copper instead of sulphides in samples from the open pit or the formation of Bn+Cov in samples from the drillcores indicates various degrees of reducing conditions during the fault (re)activation.

The compositional data in this study allowed two independent geothermometers to be applied. The wide range of formation temperatures indicated by chlorite geothermometry and corresponding (6-Al^{vi}) values can be clearly seen on Figure 2h, reinforcing a model of regional metamorphism with pronounced retrograde overprint (e.g. in sample RG27). The temperatures obtained from sphalerite-stannite geothermometry (Figure 5d) overlap with upper temperature ranges obtained for chlorite from both diorite and granite. Considering the depth of the analysed samples with similar depth to the granite it is most likely that this temperature represents re-equilibration of Sph-Stn in the thermal contact aureoles of the granite.

Syn-metamorphic and late-granite overprinting

The ore textures, associations and trace element distribution in molybdenite are all highly suggestive of mineral re-equilibration and remobilisation during metamorphism and subsequent granite emplacement.

LOCAL SULPHIDE REMOBILISATION

The relationships between Cu-Fe-sulphides (Cp and Cub) and Po and the inclusions they contain are indicative of localised variability in the composition of sulphide assemblages followed by different degrees of re-equilibration. For example, variable Cu:Fe ratios within the Cu-Fe-sulphides would result in exsolution of Cub exsolving from Cp or Po from Cub. Minor contents of Zn and Sn in the Cu-Fe-sulphides would result in either exsolution of Sph-Stn pairs from Cub or their accumulation at the boundaries between Cp and Po. The low Ni and Co contents determined in Po reflect release of these elements during metamorphism and subsequent formation of discrete Co-Ni-bearing minerals (Pn, Mkw and Thio). The diversity of Co-Ni-mineral species within the same sample, e.g. coexisting Ag-Pn and Pn and from one sample to another e.g. differences in the thiospinel composition (see also Kalleske 2010) further emphasises the role of syn-metamorphic remobilisation in generation of the highly variable trace mineral signature seen throughout the deposit. The replacement of Po by Py, the abundance of REE-minerals observed in such samples (e.g. RG59), as well as the abundance of scheelite and W-REE-bearing minerals within Fe-Ti oxides (e.g. RG52) are all indicative of a late-stage overprint due to interaction with fluids attributable to hydrothermal activity associated with granite emplacement.

The wide compositional range for Po (Figure 5a-c) and the textural relationships observed between the two pyrrhotite species in the diorite suggest the presence of different structural types, one of which is close to troilite, and the others, defined by different stoichiometries (Fe_7S_8 , Fe_9S_{10} , $\text{Fe}_{10}\text{S}_{11}$), represent superstructures (Posfai & Buseck 1997). Natural Po superstructures are commonly ferromagnetic. Troilite, however, is antiferromagnetic at temperatures below 140 °C and 1 bar, but undergoes two magnetic phase transitions of which the β -phase transition is at the Curie temperature (315 °C; e.g. Fleet 2006). The textural expression of lamellar exsolution of the two Po species (with pointed edges) suggests formation during syn-metamorphic deformation. Although the crystal structure of the $\sim\text{FeS}$ phase would need to be determined, an analogy can be made with comparable lamellar exsolution between coexisting Po species at Challenger, S.A. (Haese 2010), one of which is troilite. As in the Challenger case, the coexisting Po types can be used to infer Po transition at the Curie point. Troilite is very rare in natural samples and is restricted to meteorites and liquid-magmatic Ni-Cu deposits (Becker *et al.* 2010). The possible occurrence at Boddington thus represents a second occurrence where troilite has formed in response to metamorphism.

RHENIUM AND W BEHAVIOUR IN MOLYBDENITE

Previous LA-ICP-MS studies of molybdenite were focused on identifying sub-grain-scale decoupling of Re and Os to assess the validity of this method for dating (e.g. Stein *et al.* 2003, Kössler *et al.* 2003, Selby & Creaser 2004). All these studies concluded that Re-Os decoupling readily takes place within molybdenite grains that undergo deformation. Rhenium mobility is discussed in terms of molybdenite crystallographic orientation but in general it is considered that Os is more mobile than Re, in particular under deformation conditions, and this explains the grain-scale decoupling observed. Other sulphides such as Cp accommodate much lower Re than molybdenite.

The trace element distributions and grain-scale inhomogeneity in molybdenite shown here are strong evidence for remobilisation of a whole range of elements, including Re, and has particular implication for Au (re)concentration. The distinctive flatness in the signal of both Re and W throughout the majority of the spectra clearly (Figure 6) indicates that these two elements are incorporated in the molybdenite lattice. This is commonly discussed in terms of the similarity between the ionic radii of Mo^{4+} (0.65Å), Re^{4+} (0.63Å) and W^{4+} (0.66Å) (e.g. Stein *et al.* 2003). In the present dataset, both Re and W have wide variation from one sample to another and even within the same sample in the diorite and differ fundamentally from the very constant values measured in molybdenite from granite. This is a clear indication that both elements have undergone grain-scale remobilisation during deformation (kinks, folds and dislocation) and/or fluids introduced by the granite. There is, however, a marked difference in the patterns observed for Re and W on the element maps, where only 1 of the 4 maps show comparable patterns (RG27) for both elements. Tungsten concentration correlates with textures attributable to either deformation or replacement. In contrast, Re remains highly concentrated within molybdenite lamellae (RG10, 25NK) that, although strongly deformed, do not show too extensive replacement. Mobilisation of Re outside of the grain is seen in the case where there is evidence for fluid percolation, e.g. dense inclusions in the granite, porosity and replacement by either Cp or silicates.

McCandless *et al.* (1993) suggested that the presence of Re in molybdenite directly induces point defects and screw-dislocation growth due to the small difference in Re^{4+} and Mo^{4+} ionic radii. Such defects could assist Re loss during post-crystallisation alteration/deformation. The present study has shown that such defects, in particular kink bending extends to the lattice scale and these are also associated with nanoporosity (Figure

13). The element maps show that W is more mobile relative to Re. The latter can display stunning zonation patterns with discrete remobilisation along pathways of fluid percolation (Figure 12).

MOLYBDENITE ROLE IN UPGRADING AU CONCENTRATION

The present study shows the consistent presence of Au and chalcophile elements (Ag, Te, Bi, Pb) throughout the molybdenite. All these elements are typically characterised by irregular signals on the LA-ICPMS spectra (Figure 6). This is concordant with the presence of abundant inclusions of tellurides in molybdenite from both granite and diorite, and also gold minerals in the diorite. The irregularity in the signal of these elements is much higher in the present dataset than in that of Kalleske (2010) implying orefield heterogeneity in terms of processes that control the concentration of these elements.

High correlation coefficients between Au and all chalcophile elements (Figure 9a-d) in the diorite indicate a common behaviour in response to processes that remobilise them. Similarly a strong association between chalcophile elements and Au is observed on the element maps, with clear indication of gold particle nucleation, even in the case of molybdenite from the granite. The presence of Bi-(Pb)-tellurides as sub-microscopic lamellae adjacent to micron-scale inclusions (Figures 13, A16) indicates coarsening of telluride lamellae from coherent lattice-scale intergrowths with molybdenite to visible inclusions. This hypothesis is reinforced by the presence of nanoporosity in the same areas. On the other hand, Au can be incorporated into the lattice of Bi-(Pb)-tellurides (Ciobanu *et al.* 2009b) and this will be released as nanoparticles during overprinting. The presence of high Au anomalies overlapping the areas with Bi, Te, Pb can be attributed to such Au concentrations in the tellurides in molybdenite from the granite. Release of this Au to form discrete gold inclusions in the same areas with visible tellurides, or further away in the same sample, is characteristic for molybdenite in the diorite.

The present study shows no 2H to 3R transformation in molybdenite. This was the crystal-structural mechanism for high concentration of trace elements suggested by Newberry (1979a, b). It gives, however an alternative explanation— formation of lattice-scale intergrowths between molybdenite and phases with crystal-structural compatibility such as Bi-(Pb)-tellurides. Considering the capacity of Bi-tellurides as Au carriers, molybdenite can

act as a true trap for Au and chalcophile elements if these elements are present in the same fluids from which molybdenite precipitated.

LATE-STAGE GRANITE AND AU SCAVENGING BY BISMUTH MELTS

Gold is seen outside molybdenite in the same Au-Ag-Bi-Te association in diorite from the contact aureole of the late-stage granite. Such associations are not locked within sulphides but rather tied to areas of chloritisation in the country rock. Temperatures of 235 °C, inferred from the equilibrium assemblages in Mld-Hed-Bi droplets, overlap with the lower temperature range estimated from chlorite geothermometry. The appearance of such droplets is indicative of crystallisation from melts precipitated out of a fluid (Ciobanu *et al.* 2005). The most likely scenario is that redox reactions between the oxidised, granite-derived fluid and reduced, altered diorite country rock neutralise Bi^{3+} which in turn scavenges Au and other elements (Te) from the fluid. The Bi^0 will precipitate as a composite Au-Bi-Te melt (instead of mineral crystallisation upon saturation) if the temperature of the redox reaction is above the melting temperature of the precipitated assemblage. This is feasible given the low-temperature assemblages mentioned above.

Bismuth-melts can scavenge Au even from a fluid undersaturated in this element (e.g. Tooth *et al.* 2008, 2011) and will greatly improve the grade in a deposit with a protracted geological history. This interpretation is concordant with the fact that the granite-derived fluid is Bi-rich but does not seem to carry high Au concentrations (gold is absent in the granite-hosted mineralisation and granite-hosted molybdenite has the lowest Au content).

Genetic model

The present study supports a multi-stage genetic model in which (i) an early porphyry-style mineralisation is overprinted by (ii) regional metamorphism and (iii) granite emplacement (Figure 16). Each of these events are characterised by metal input, the majority of Cu introduced during (i), Au in (ii) and Bi-Te in (iii). Although primary textures from the earliest event are obliterated by metamorphism, the dominant Cu character and style of mineralisation (disseminations, patches, small veinlets) in the deposit are concordant with a porphyry Cu-Mo-(Au) system.

Rhenium content in molybdenite is a good indicator of the mineralisation type (see above) and the present LA-ICPMS dataset is large enough to statistically characterise distinct populations of molybdenite. Despite grain-scale variability, the Re values in a given sample and also across sampling intervals cluster within a narrow range, a fact also supported by the element maps, thus proving the ‘robustness’ of Re relative to overprint. The three distinct populations of molybdenite can be attributed to: (i) porphyry-Moly (highest Re, mean 254 ppm) (ii) orogenic-Moly (lowest Re, mean 1.76 ppm) and (iii) granite-Moly (low Re, mean 3.94 ppm). The first two are hosted in diorite and the last in granite. Although, low-Re Moly in the diorite could be considered input from the granite in the contact aureole, given the small difference in the Re concentration, the distinct Ni-Co signature of all Moly hosted by diorite (Figure 9e) shows that the three Moly generations are proven as discussed above.

The spatial distribution shows that the porphyry-Moly is dominant at shallower levels in both Central Diorite and ABreccia; orogenic Moly is at an intermediate level between the shallow levels and the granite (Figure 8a). The spatial overlap of these two types within the same sample or sampling interval (2.5m interval for RG27, 29, 30; WBD105900002 and RG64; WRD10600004) is observed in diorite located within the granite contact aureole; in the latter example re-crystallisation of porphyry Moly is also observed.

Higher Au values in molybdenite, both porphyry and orogenic, throughout the Central Diorite are the result of increase in Au concentration during both the metamorphic and granite emplacement events as discussed above. The distal location of ABreccia relative to the granite can thus explain the lower Au values in the molybdenite from this orebody where only metamorphism would have overprinted porphyry Moly. High-grade, shear-hosted Au mineralisation within the Eastern Shear Zone (‘Jarrah’), as well as the majority of Au locked as inclusions within the sulphides, is attributable to the orogenic event.

The granite introduced chalcophile elements (Bi and Te) that greatly assisted concentration of Au in diorite-hosted Moly. The granite is clearly multi-phase where the finer-grained varieties are part of later aplitic suites and are depleted in such elements. Rhenium values are, however, comparable indicating the common magmatic reservoir for both coarse- and aplitic-granite. The granitic fluids are probably the lowest in Au but they have contributed to the overall Au balance in the deposit given the high Bi-Te content and melt-scavenging by Bi. The granite was probably emplaced during or shortly after peak metamorphism. The ages obtained by Allibone *et al.* (1998) and Stein *et al.* (2001) both carry

a sizeable analytical error. Based on the present observation the low-Re Moly in the diorite could be used for a more accurate dating of the orogenic event.

The strong Bi-Te signature in Au mineralisation throughout the deposit, as well as molybdenite from the diorite, suggests that this is a characteristic that may have been inherited from the earlier porphyry- or orogenic-style systems rather than introduced only by the granite. It is interesting to note that even the bonanza ore has a marked Bi-Te signature (e.g. saddlebackite).

Although the intrusion-related model for the mineralisation has merit (high Bi-Te, reduced ore types, localised alteration), it cannot be proven in totality (low-Au fluids, lack of the S-type granite character). However, the overprinting effects introduced by granite emplacement (heat flow, acidic Bi-bearing fluids) greatly increased Au grades in the contact aureole. The intrusion-related exploration model is thus valid in the SGB. The recent discovery of the high-grade Katanning Au prospects in a granite aureole (Ausgold 2010), 200 km SE of Boddington supports this idea. The unusual characteristics of Boddington are however the result of the protracted geological history where gold- and sulphide-remobilisation greatly contributed to the giant size and economic Au grades.

The data presented here, complementing Kalleske (2010), strongly support the hypothesis that molybdenite trace element chemistry represents a valuable new metallogenic and vectoring tool.

CONCLUSIONS

- Molybdenite can incorporate not only Re but a whole range of other trace elements via structural defects and coherent lattice scale-intergrowths
- Concentrations of Re in molybdenite are highly variable on the deposit-scale. Economically significant concentrations of Re occur only at shallower levels in both Central Diorite and ABreccia; and not at deeper levels in the contact aureole of the granite.
- Grain-scale inhomogeneity in molybdenite is documented and can be related to the relative mobility of the different trace elements during overprinting.
- There is a marked association between gold and molybdenite, particularly when accompanied by intergrowths of Bi-tellurides, suggesting trapping of Au within Bi-

tellurides in both reworked early, high-Au molybdenite and later, Au-poor molybdenite.

- Available petrographic, mineralogical and geochemical evidence points to a three-stage (porphyry-style, ‘orogenic’ and intrusion-related) genetic model for Boddington.
- Whereas the orogenic event introduces most of the Au, the granite emplacement upgrades the Au grades in the deposit by Bi-melt scavenging.
- Molybdenite trace element chemistry represents a valuable new metallogenic and vectoring tool in comparable terranes.

ACKNOWLEDGEMENTS

First and foremost, I would like to thank Newmont Asia-Pacific and the staff of the Boddington Gold Mine for their financial support, accommodation, time and assistance throughout the project. In particular, I wish to thank Graeme Reynolds (Senior Exploration Geologist), Daniella De Pretis and Royce Haese for making time in their busy schedules to assist throughout the year. Secondly, I would also like to thank my co-supervisors Cristiana Ciobanu and Nigel Cook for their guidance and expertise in fieldwork, analytical work and their continual enthusiasm throughout the year. The advice and effort they gave over the year to continually put the project ahead of their own agendas was commendable and the experience I gained throughout the year was invaluable.

A thank you must go to the staff of Adelaide Microscopy, with special mentions to Ben Wade, Angus Netting and Leonard Green for their tireless efforts through day and night helping with the world-class machines. The Australian Microscopy and Microanalysis Research Facility is gratefully acknowledged for access to FIB-SEM instrumentation. A further mention must go to Cristiana for her time and guidance spent on the TEM collecting the data. A thank you must go to CODES (University of Tasmania) for use of their LA-ICPMS and for the expertise of Sarah Gilbert and Leonard Danyushevsky. Thanks are also due to the University of Adelaide and staff for the facilities throughout the year that enabled completion of this project, and for the time staff spent on field trips. Thank you to Emma Alexander, Ryan Gore, Dennis Meria and Daniel O’Rielly for their help and assistance with the computer programmes used during the year.

Lastly, I would like to thank the large number of friends and family who have helped me over the year, in particular Emma Alexander and her family for continual support and

hospitality. Thank you to the honours year of 2011 for a great experience and to my own family for the financial assistance and support throughout the year.

REFERENCES

- Allibone A. H., Windh J., Etheridge M. A., Burton D., Anderson G., Edwards P. W., Miller A., Graves C., Fanning C. M. & Wysoczanski R. 1998. Timing relationships and structural controls on the location of Au-Cu mineralization at the Boddington gold mine, Western Australia. *Economic Geology* **93**, 245-270.
- Ausgold 2011. Katanning update-gold mineralisation confirmed at Fraser. ASX announcement, www.ausgold.com.au.
- Barley M. E. & Groves D. I. 1990. Deciphering the tectonic evolution of archean greenstone belts: The importance of contracting histories to the distribution of mineralisation in the Yilgarn craton, Western Australia. *Precambrian Research* **46**, 3-20.
- Becker M., De Villiers J. & Bradshaw D. 2010. The mineralogy and crystallography of pyrrhotite from selected nickel and PGE ore deposits. *Economic Geology* **105**, 1025–1037.
- Cassidy K. F., Champion D. C. & Wyborn L. A. I. 1998. A geochemical study of granitoids of the Boddington gold mine. *Australian Geological Survey Organisation*, 1-34.
- Cathelineau M. 1988. Cation site occupancy in chlorites and illites as a function of temperature. *Clays and Clay Minerals* **23**, 471–485.
- Ciobanu C. L., Cook N. J. & Pring A. 2005. Bismuth tellurides as gold scavengers. In: Mao, J.W., Bierlein, F.P. (eds.). *Mineral Deposit Research: Meeting the Global Challenge*, vol. **2**, Springer, p.1383-1386.
- Ciobanu C. L., Pring A., Cook N. J., Self P., Jefferson D., Dima G. I. & Melnikov V. 2009a. Crystal-structural modularity in the tetradymite group: An HR-TEM study. *American Mineralogist* **94**, 517–534.
- Ciobanu C. L., Cook N. J., Pring A., Brugger J., Danyushevsky L. V. & Shimizu M. 2009b. 'Invisible gold' in bismuth chalcogenides. *Geochimica et Cosmochimica Acta* **73**, 1970-1999.
- Ciobanu C. L., Cook N. J., Utsunomiya S., Pring A., Green L., 2011. Focussed ion beam-transmission electron microscopy applications in ore mineralogy: Bridging micro- and nanoscale observations. *Ore Geology Reviews*, Vol 42, p. 7-31.
- Clarke R. M. 1997. Saddlebackite, $Pb_2Bi_2Te_2S_3$, a new mineral species from the Boddington gold deposit, Western Australia. *Australian Journal of Mineralogy* **3**, 119-124.

- Cook N. J., Ciobanu C. L., Wagner T. & Stanley C. J. 2007a. Minerals of the system bi-te-se-s related to the tetradymite archetype: Review of classification and compositional variation. *Canadian Mineralogist* **45**, 665-708.
- Cook N. J., Ciobanu C. L., Stanley C. J., Paar W. H. & Sundblad K. 2007b. Compositional data for Bi-Pb tellurosulfides. *Canadian Mineralogist* **45**, 417-435.
- Cook N. J., Ciobanu C. L., Spry P. G., Voudouris P., and the participants of IGCP-486 2009. Understanding gold-(silver)-telluride-(selenide) mineral deposits. *Episodes* **32**, 249-263.
- Danyushevsky L. V., Robinson P., Gilbert S., Norman, M., Large R., McGoldrick P. & Shelley J. M. G. 2011. Routine quantitative multi-element analysis of sulphide minerals by Laser Ablation ICP-MS: Standard development and consideration of matrix effects. *Geochemistry: Exploration, Environment, Analysis* **11**, 51-60.
- De Caritat T. P., Hutcheon I. & Walshe J. L. 1993. Chlorite geothermometry: A review. *Clays and Clay Minerals* **41**, 219-239.
- Duuring P., Cassidy K. F. & Hagemann S. G. 2007. Granitoid-associated orogenic, intrusion-related, and porphyry style metal deposits in the Archean Yilgarn craton, Western Australia. *Ore Geology Reviews* **32**, 157-186.
- Fleet M. E. 2006. Phase equilibria at high temperatures. *Reviews in Mineralogy and Geochemistry* **61**. 365-419.
- Haese R. 2010. Ore mineralogy and geochemistry in the M2 orebody, Challenger, SA: Implications for gold distribution and remobilisation. Bsc (Hons) thesis, Geology and Geophysics, University of Adelaide, Adelaide (unpubl.).
- Hagemann S. G., McCuaig C. C., Mavrogenes J., Cassidy K. F. & Behn M. 2007. The genesis of the Au-Cu-Mo Boddington gold mine: Constraints based on a melt and fluid inclusion study. Proceedings of Kalgoorlie '07 Conference, Kalgoorlie, W.A. *Geoscience Australia Record*, p. 62-64.
- Hart C. J. R. 2007. Reduced intrusion-related gold systems. In: Goodfellow, W.D. (ed.), Mineral Deposits of Canada: A synthesis of major deposit types, district metallogeny, the evolution of geological provinces, and exploration methods. Geological Association of Canada, Mineral Deposits Division, p. 95-112.
- Hayes P. 2009. Newmont starts production at Boddington. *Australian Mining*.
- Jowett E. C. 1991. Fitting iron and magnesium into the hydrothermal chlorite geothermometer. Abstract volume, GAC/MAC/SEG Joint Annual Meeting, Toronto, May 27-29 1991.

- Kalleske N. 2010. Mineralogical and petrogenetic study of gold ore from the Boddington gold deposit, W.A. Bsc (Hons) thesis, Geology and Geophysics, University of Adelaide, Adelaide (unpubl.).
- Kösler J., Simonetti A., Sylvester P., Cox R., Tubrett M. N. & Wilton D. 2003. Laser ablation ICP-MS measurements of Re/Os in molybdenite and implications for Re-Os geochronology. *Canadian Mineralogist* **41**, 307-320.
- Lang J. R. & Baker T. 2001. Intrusion-related gold systems: The present level of understanding. *Mineralium Deposita* **36**, 477-489.
- Large R. R., Danyushevsky L., Hollit C., Maslennikov V., Meffre S., Gilbert S., Bull S., Scott R., Emsbo P., Thomas H., Singh B. & J. F. 2009. Gold and trace element zonation in pyrite using a laser imaging technique: Implications for the timing of gold in orogenic and Carlin-style sediment-hosted deposits. *Economic Geology* **104**, 635-668.
- McCandless T. E., Ruiz J. & Campbell A. R. 1993. Rhenium behaviour in molybdenite in hypogene and near-surface environments: Implications for Re-Os geochronology. *Geochimica et Cosmochimica Acta* **57**, 889-905.
- McCuaig T. C., Behn M., Stein H. J., Hagemann S. G., McNaughton N. J., Cassidy K. F., Champion D. & Wyborn L. 2001. The Boddington gold mine: A new style of Archean Au-Cu deposit. *AGSO. Geoscience Australia* **37**, 453-455.
- Myers J. S. 1993. Precambrian history of the West Australian craton and adjacent orogens. *Annual Review of Earth Planetary Sciences* **21**, 453-485.
- Newberry R. J. J. 1979a. Polytypism in molybdenite (i): A non-equilibrium impurity induced phenomenon. *American Mineralogist* **64**, 758-767.
- Newberry R. J. J. 1979b. Polytypism in molybdenite (ii): Relationships between polytypism, ore deposition/alteration stages and rhenium contents. *American Mineralogist* **64**, 768-775.
- Plimer I., R. 1974. A spessartite-rich alteration assemblage from the Bega granite, N.S.W., Australia. *Lithos* **7**, 43-51.
- Posfai M. & Busek P. R. 1997. Modular structures in sulphides: Spalerite/wurtzite-pyrite/marcasite-, and pyrrhotite-type minerals. *EMU Notes in Mineralogy* **1**, 193-235.
- Prince A., Raynor G. V. & Evans D. S. 1990. Phase Diagrams of Ternary Gold Alloys. Institute of Metals, London, 505 pp.
- Roth E. & Anderson G. 1993. Evidence for reduced high salinity ore fluids in the archaean porphyry-style Cu-Au-Mo deposit at Boddington, Western Australia. Current Research in

- Geology Applied to Ore Deposits, Proceedings of the Second Biennial SGA Meeting, Granada, Spain, p. 233-236
- Selby D. & Creaser R. A. 2004. Macroscale trends and microscale laser-ablation ICP-MS Re-Os isotopic analysis of molybdenite: Testing restrictions for reliable Re-Os age determinations, and implications for the decoupling of Re and Os within molybdenite. *Geochimica et Cosmochimica Acta* **68**, 3897-3908.
- Shimizu M. & Shikazono N. 1985. Iron and zinc partitioning between coexisting stannite and sphalerite: A possible indicator of temperature and sulfur fugacity. *Mineralium Deposita* **20**, 314-320.
- Stein H. J., Markey R. J., Morgan J.W., Selby D., Creaser R.A., McCuaig T.C. & Behn M. 2001. Re-Os dating of Boddington Molybdenite, SW Yilgarn: Two mineralisation events. *AGSO- Geoscience Australia* **37**, 469-471.
- Stein H. J., Schersten A., Hannah J. L. & Markey R. J. 2003. Subgrain decoupling of Re and ¹⁸⁷Os and assessment of Laser Ablation ICP-MS spot dating in molybdenite. *Geochimica et Cosmochimica Acta* **67**, 3673-3686.
- Tooth B., Brugger J., Ciobanu C. L. & Liu W. 2008. Modeling of gold scavenging by bismuth melts coexisting with hydrothermal fluids. *Geology* **36**, 815-818.
- Tooth B., Ciobanu C. L., Green L., O'Neill B. & Brugger J. 2011. Bi-melt formation and gold scavenging from hydrothermal fluids: An experimental study. *Geochimica et Cosmochimica Acta* **75**, 5423-5443.
- Wagner T. & Cook N. J. 1999. Carrollite and related minerals of the Linnaeite group: solid solutions and nomenclature in the light of new data from the Siegerland district, Germany. *Canadian Mineralogist* **37**, 545-558.
- Wilde S. A. & Pidgeon R. T. 1986. Geology and geochronology of the saddleback greenstone belt in the archaean Yilgarn block, Southwestern Australia. *Australian Journal of Earth Sciences* **33**, 491-501.

FIGURE CAPTIONS

FIGURE 1. Geological sketch showing geology and main orebodies in the Open Pit at Boodington at level 150RL (modified from Kalleske 2010). Location of samples from drillcore and Open Pit area is indicated in red. Inset shows the location of the Boddington deposit in the Yilgarn Craton.

FIGURE 2. (a-e) Ternary plots showing the composition of silicates in the granite and diorite. **(a, b)** Ab-An-Kfs plots showing the compositional variation in feldspars. **(c, d)** XFe-XAl-XMn compositional plots for epidote-group minerals; note that granite **(d)** shows a larger compositional field but the range remains within Clz. **(e)** Ternary Fe-Mg-Al^{vi} plot showing the compositional range for chlorite in diorite (diamonds) and granite (circles). Note that Fe-richer varieties (end-member chamosite) are present in granite, whereas the Mg-richer chlorites are from diorite. **(f-h)** Binary plots of T vs. Al^{iv} **(f, g)** and vs. 6-Al^{vi} **(h)** in chlorite, showing the temperature ranges for distinct populations in diorite and granite.

FIGURE 3. Reflected light photomicrographs showing textures in molybdenite. **(a-c)** Coarse-grained molybdenite with typical deformation **(a)**, kink-bending in marginal lamellae **(b)** and around silicates **(c)**. **(d)** Atypical short-lamellar molybdenite forming an aggregate mesh. **(e)** Typical occurrence of coarser, micron-scale Bi-telluride inclusions adjacent to kink-bending. **(f)** Abundant, coarse chalcopyrite inclusions occurring in molybdenite from diorite; note the pointed edge termination of chalcopyrite lamellae. **(g)** Field of Bi-telluride inclusions coarsening across kinked lamellae in molybdenite from granite. **(h)** Bismuth-telluride segregation through axial planes of microfolds. **(i)** Remobilisation of Bi-telluride and chalcopyrite inclusions along microshears.

FIGURE 4. Back-scattered electron (BSE) images showing aspects of the Au-Ag-Bi-(Pb)-Te-(Se) association. **(a, b)** Filaments of gold and electrum in molybdenite. **(c)** Composite gold and Pb-Bi-telluride inclusion in molybdenite. **(d)** Droplet of maldonite+hedleyite+bismuth in gangue. This association represents the equivalent of the eutectic at 235 °C in the system Au-Bi-Te. **(e)** Cluster of Au-minerals and Bi-tellurides in areas of chloritisation along an Act+Clz+Qz+Bt veinlet [the droplet in **(d)** is part of this area]. **(f)** Gold-bismuth assemblage in similar context as shown in **(e)**. **(g-i)** Different contexts for hessite-Bi-tellurides±bismuth inclusions: at the boundary between adularia and chalcopyrite in diorite **(g)**; in gangue adjacent to chalcopyrite in granite **(h)** and within molybdenite from granite **(i)**. **(j)** Typical fields of telluride inclusions along lamellae and kink-bends in

molybdenite. **(k)** Altaite associated with Bi-tellurides in molybdenite from diorite **(l)** Ikunolite as part of a complex telluride-bismuth assemblage within molybdenite from diorite.

FIGURE 5. (a-c) Binary plots of total metal (M) versus S for pyrrhotite in granite and diorite. **(a)** Single-phase pyrrhotite corresponding to Fe_7S_8 from granite. **(b)** Single-phase pyrrhotite corresponding with Fe_7S_8 - Fe_9S_{10} from diorite. **(c)** Distinct compositional fields for two-phase pyrrhotite occurring as lamellar exsolutions in diorite. The phase that is ‘bright’ on BSE images forms a field close to FeS (troilite) whereas composition of the ‘dark’ phase straddles across $\text{Fe}_{10}\text{S}_{11}$ - Fe_7S_8 . **(d)** Sphalerite-stannite geothermometry plot showing formation temperatures from $\log X_{\text{FeS}}/X_{\text{ZnS}}$ ratios in the two minerals. The cluster of points along the 350 °C calibration line (Shimizu & Shikazono 1985) is the most reliable.

FIGURE 6. (a-f) LA-ICPMS spectra for molybdenite from diorite **(a-f)** and granite **(g, h)**. Note the difference between the flat signals for Re and W highly irregular signals for Au, Bi, Te and Pb across the time-resolved spectra.

FIGURE 7. Histograms showing the distribution of trace elements in molybdenite from granite (green) and diorite (red, purple and blue colours). **(a)** Rhenium in molybdenite from granite has a normal distribution whereas in molybdenite from diorite shows bimodal distribution. **(b)** In contrast, W in molybdenite from granite has bimodal distribution and normal distribution in molybdenite from diorite. **(c)** Gold shows normal distribution in molybdenite from granite (lower concentration) and bimodal distribution in molybdenite from diorite; note that majority of data plots at higher concentrations in the latter case. **(d)** Silver displays normal distribution for molybdenite from both granite and diorite. **(e-g)** Bismuth, Te and Pb show slight bimodal and normal distributions for molybdenite in granite and diorite respectively. The high-range corresponds to molybdenite from the coarse-grained granite, whereas the lower range is for the molybdenite in the aplitic variety.

FIGURE 8: LA-ICP-MS plots showing element concentration vs. depth in all analysed molybdenite. **(a)** Rhenium shows a decreasing trend and wider variation at depth. **(b)** Tungsten shows no variation or trend with depth. **(c)** Gold shows a wider variation and slight decreasing trend with depth. **(d)** Silver shows no trend but slightly wider variation at depth. **(e)** Tellurium shows marked increasing trend and wider variation at depth. **(f, g)** Bismuth and lead both display wider variation at depth where the highest and lowest concentrations are seen in molybdenite from coarse- and fine-grained granite, respectively.

FIGURE 9. LA-ICP-MS correlation plots between Au and chalcophile elements (**a-d**), Ni-Co (**e**) Re-W (**f**) and Au-Re (**g**) in molybdenite. Au and chalcophile elements show much higher correlation coefficients for molybdenite in diorite compared to molybdenite in granite (**a-c**). Gold and Ag have comparable correlation coefficients for molybdenite from diorite and granite (**d**). Very high correlation coefficient for Co-Ni in molybdenite from diorite compared to molybdenite from granite (**e**). (**f**) Rhenium and W show a funnel-shaped distribution. (**g**) Gold versus Re shows no correlation but it discriminates the four Re populations in molybdenite. The higher Au is clearly characteristic for molybdenite from diorite.

FIGURE 10. LA-ICP-MS spot analysis of trace element concentration in molybdenite from diorite (**a-j**) and granite (**k**) showing grain scale inhomogeneity relative to textures. (**a**) Apex of bends in molybdenite lamellae from diorite showing both Re (hundreds of ppm) and Au (tens of ppm) are relatively constant. (**b**) Apex of bends in molybdenite lamellae from diorite showing constant Re values but variable Au (**c**) Replacement of molybdenite lamellae by chalcopyrite showing low Re and high Au values. (**d**) Coarse, deformed molybdenite from diorite showing low Re but higher Au values. (**e**) Idiomorphic, short molybdenite lamellae from the same diorite sample as in (**d**) showing high Re (hundreds of ppm) but very low Au values. (**f**) Slightly deformed molybdenite lamellae from the same diorite sample as in (**d**) and (**e**) showing Au variation up to two orders of magnitude but constant high Re. The examples in d-f show coexistence of molybdenite from two generations: recrystallised porphyry in (**e**, **f**) and orogenic in (**d**). (**g**) Molybdenite from diorite showing the highest Au value measured suggesting particle nucleation along grain boundaries. (**h**) Axis of a kink folds in molybdenite from the diorite higher Au but low Re. (**i**) Similar texture as in (**h**) in molybdenite from diorite showing lower Au. (**j**) Apex of a tight microfold in molybdenite from diorite showing higher Au. Aspects of molybdenite in (**g-j**) are characteristic for the orogenic event with low Re but highly variable Au content. (**k**) Large, coarse molybdenite aggregate in a granite sample showing microscale textures with large inhomogeneity in Bi, Pb, Te but relatively constant, low Re, W and Au. Rectangle in red shows the area for the LA-ICP-MS element map in Figure 12.

FIGURE 11. LA-ICP-MS element map for molybdenite in a diorite sample (RG27). The area is representative for trace element variation relative to replacement by Cp and Clz and also in kink bend. Both Re and W are concentrated towards the lamellae boundaries and within the kink. Bismuth and Pb show strong correlation and have similar patterns to Au and Ag.

FIGURE 12. LA-ICP-MS element map for molybdenite in a granite sample (RG45). The area shows kink bends and silicate replacement and minute Bi-(Pb)-telluride inclusions. The chalcophile elements (Bi, Pb, Te) show strong correlation with each other; Au shows high-concentration spots overlapping enrichment in chalcophile elements. Re displays grain zonation where the core is relative free of replacement.

FIGURE 13. High-resolution FIB-SEM (secondary electron) images (**a-c**) and bright-field TEM images (**d-m**) of molybdenite from granite and diorite. (**a-c**) Sub-micron inclusions and fine particles (arrowed on c) of Bi-tellurides in molybdenite; note also the presence of galena in (**a**). (**d-f**) Nanometer-scale lamellar intergrowths between Bi-(Pb)-tellurides and molybdenite. Note high-porosity and ‘hair-pin’ folds in molybdenite in (**e**). Selected area of electron diffraction (SAED) as insets in (d) and (f) show parallel orientation of molybdenite and Bi-Pb-tellurides along c^* and [1-10] zone in galena, respectively. (**g-j**) Nanoporosity in molybdenite (arrowed) adjusted by bending (**g**), curvature (**h**), ‘hair-pin’ folds (**i**) and twinning (**j**) in molybdenite. SAED (inset j) shows twinning at $\sim 90^\circ$. (**k-l**) Distortion of lattice fringes (arrowed). (**m**) Lattice fringes and SAED (inset) showing 2H molybdenite on [1100] zone; 3+1 integer ($hklm$) indexation is with respect to the hexagonal cell setting.

FIGURE 14. SAEDs, bright field TEM images and interpretation of stacking sequences in Bi-(Pb)-tellurides from the diorite and granite samples. (**a, b**) SAEDs showing $[-110]_R=[110]_H$ zone axis in pilsenite (**a**) and tsumoite (**b**). Three-integer indexation, corresponding to the subscript R, is with respect to rhombohedral subcell and (3 + 1) integer ($hklm$) indexation, whereas subscript H is with respect to the hexagonal cell setting. (**c**) Lattice fringes in tsumoite showing the typical 5- and 7-atom stacking sequence in which minor disorder is observed (‘55’ layer repeats). (**d-e**) SAEDs showing the $[-110]_R=[110]_H$ zone axis in unnamed $Bi_4Pb_7Te_4S_9$. Stacking disorder is indicated by streaks and the pronounced ellipsoidal shape of reflections along c^* and parallel rows in (**e**). (**f, g**) Lattice fringes in unnamed $Bi_4Pb_7Te_4S_9$ showing ordered sequences (alternative 11- and 13-atom layers, f) and disordered sequences (intervals of 13-atom layers, g). (**h-j**) interpretation of the stacking sequences using the reflection distribution and their relative intensities in the characteristic ‘d’ interval (Ciobanu *et al.* 2009a) corresponding to the rhombohedral sub-cell (marked on SAEDs in a, b, d, e). The number of divisions in the ‘d’ interval corresponds to the number of layers in the unit cell. The number of divisions within the central part of ‘d’ (between the two second brightest reflections) corresponds to the number of layer-units defining the stacking sequence, e.g. 2 in both tsumoite and the unnamed phase (**i, j**) but single

layer in pilsenite (**h**). In (**j**) the upper and lower ‘d’ intervals show the difference between ordered and disordered state in terms of reflection morphology.

FIGURE 15. Schematic cartoon illustrating the three-stage mineralisation model for Boddington. (**a**) Porphyry Cu-Mo-(Au) mineralisation formed during diorite intrusion within volcanic arc environment. High Re concentration in molybdenite is concordant with a mantle source. (**b**) Orogenic Au-style mineralisation emplaced during shearing and syn-metamorphic deformation at ca. 2675 Ma synchronous with the first (Archean) dyke emplacement (not shown on figure) and sulphide remobilisation. Molybdenite is characterised by low Re concentrations (<1 ppm) but a Co-Ni signature, common also to the porphyry-style molybdenite. (**c**) Intrusion-related Mo-Bi-Te-(Au) mineralisation associated with granite emplacement. Molybdenite is characterised by low Re concentration (a few ppm). Aplitic granite present at depth (yellow crosses) has the same Re concentration but much lower Bi and Te. Molybdenite lacks a Co-Ni signature. Further remobilisation of metals and sulphide re-equilibration in the contact aureole and Au scavenging by Bi-melts is interpreted as the result of interaction between high-chalcophile element but low-Au granitic fluids. (**d**) Present-day exposure level of the Boddington mineralisation. Abundant Proterozoic dyke swarms are not shown for simplicity.

LIST OF TABLES

TABLE 1. Sample description

TABLE 2. Mineral abbreviations

TABLE 3. Microprobe analyses of chlorite group minerals

TABLE 4. Electron probe microanalyses of pyrrhotite

TABLE 5. Electron probe microanalyses of sphalerite and stannite

TABLE 6. Electron probe microanalyses of gold/electrum, maldonite and hessite

TABLE 7. Electron probe microanalyses of bismuth telluride species

TABLE 8. Summary of LA-ICP-MS spot analyses of molybdenite

Figure 1

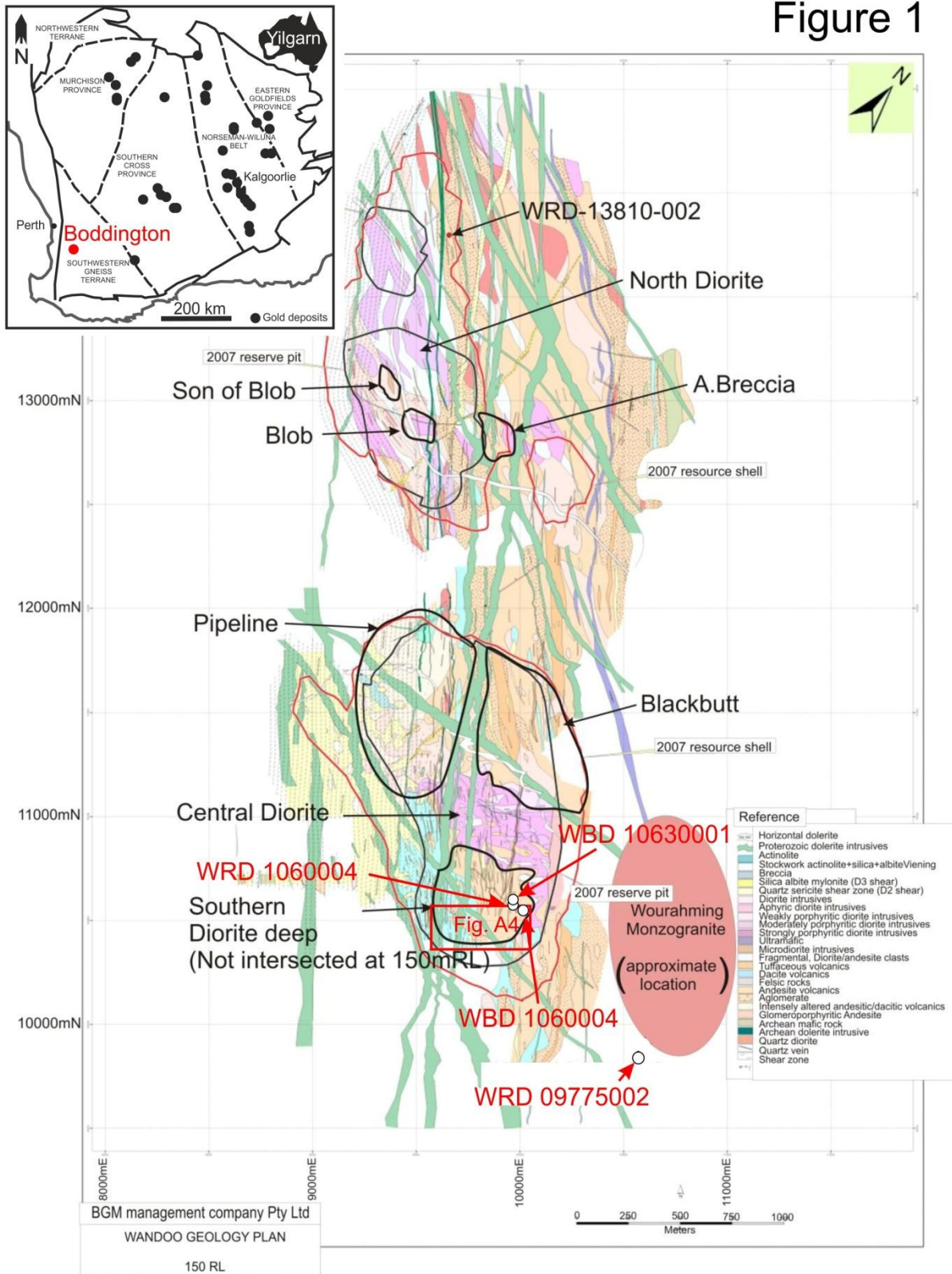


Figure 2

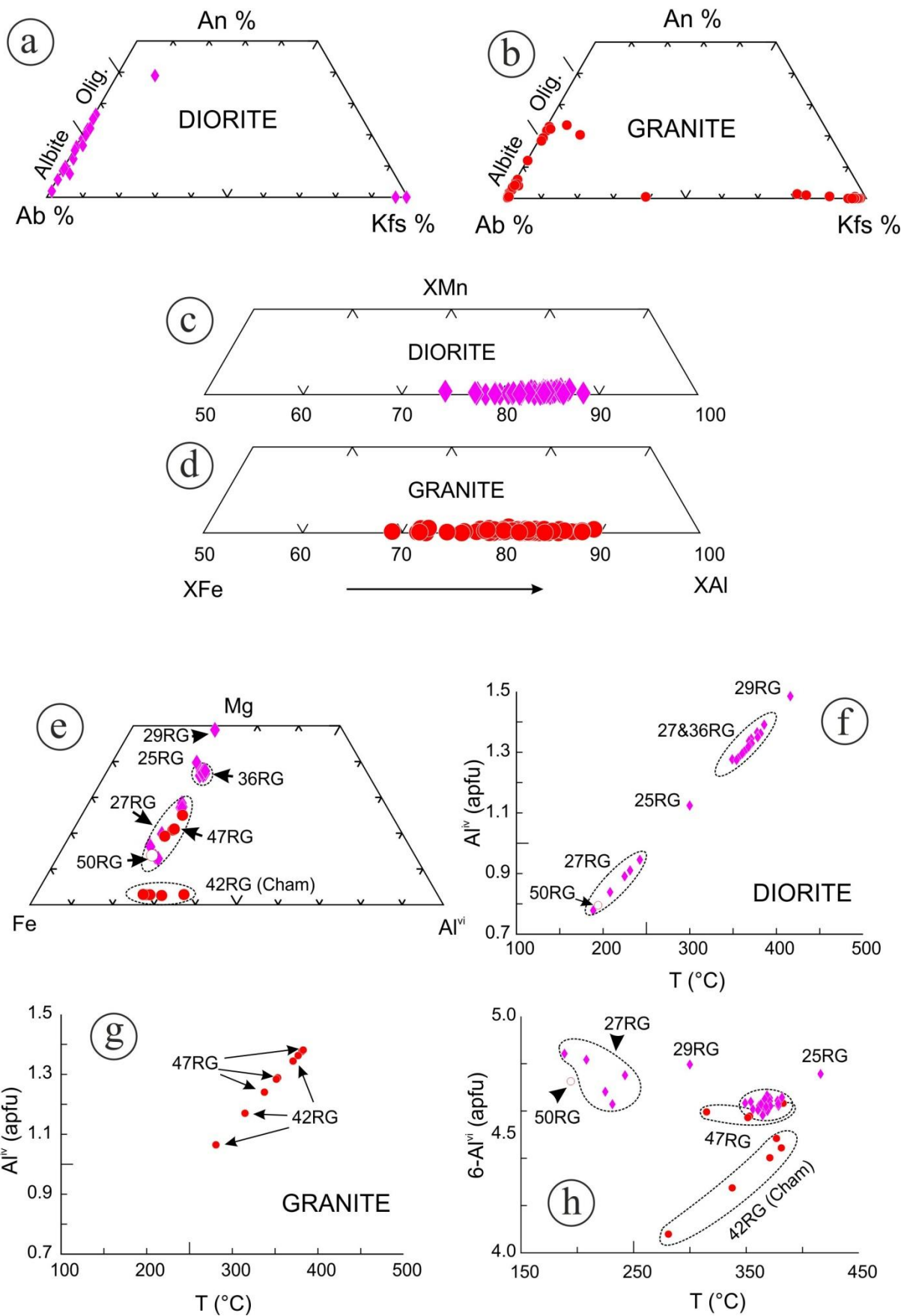


Figure 3

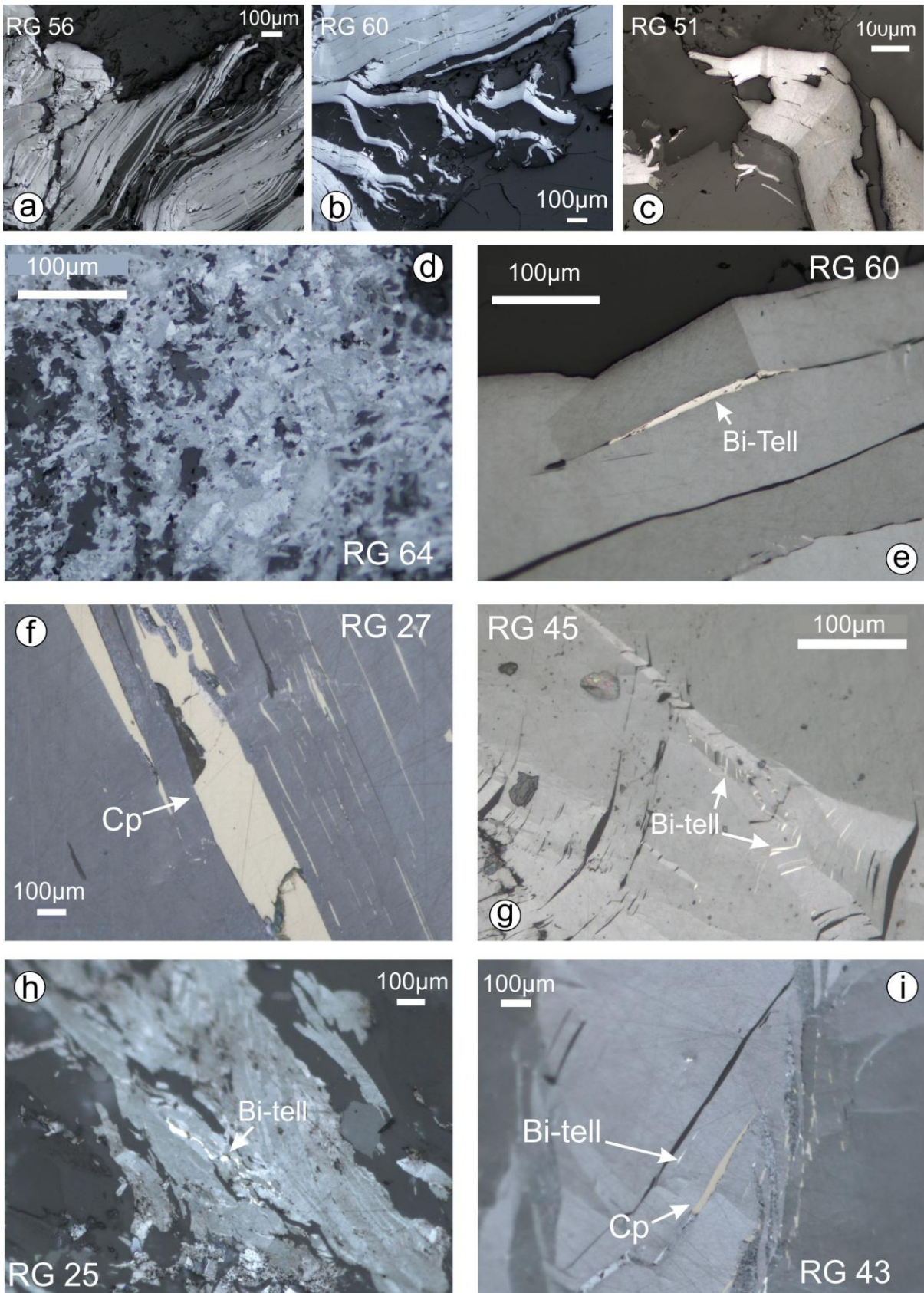


Figure 4

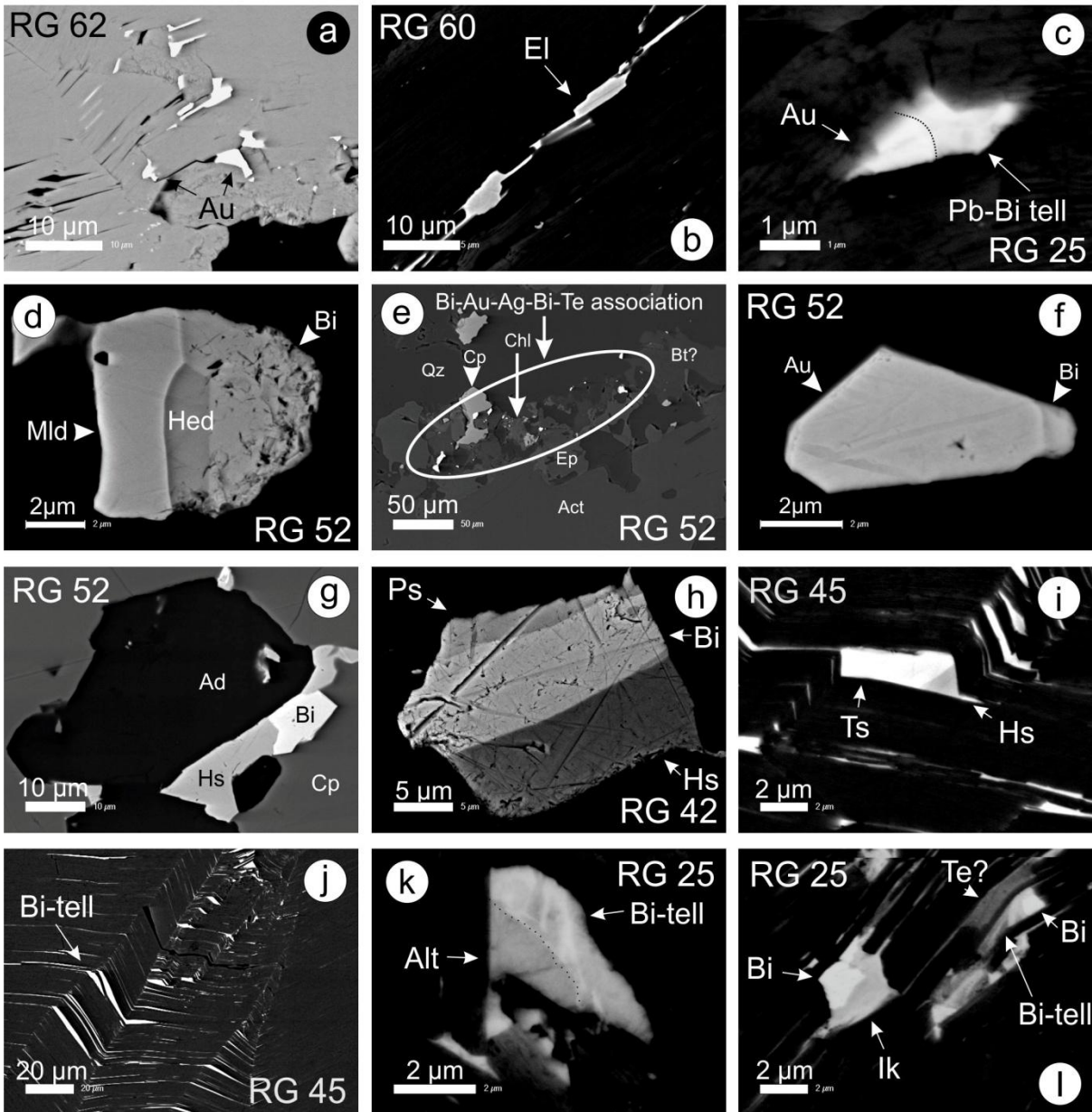


Figure 5

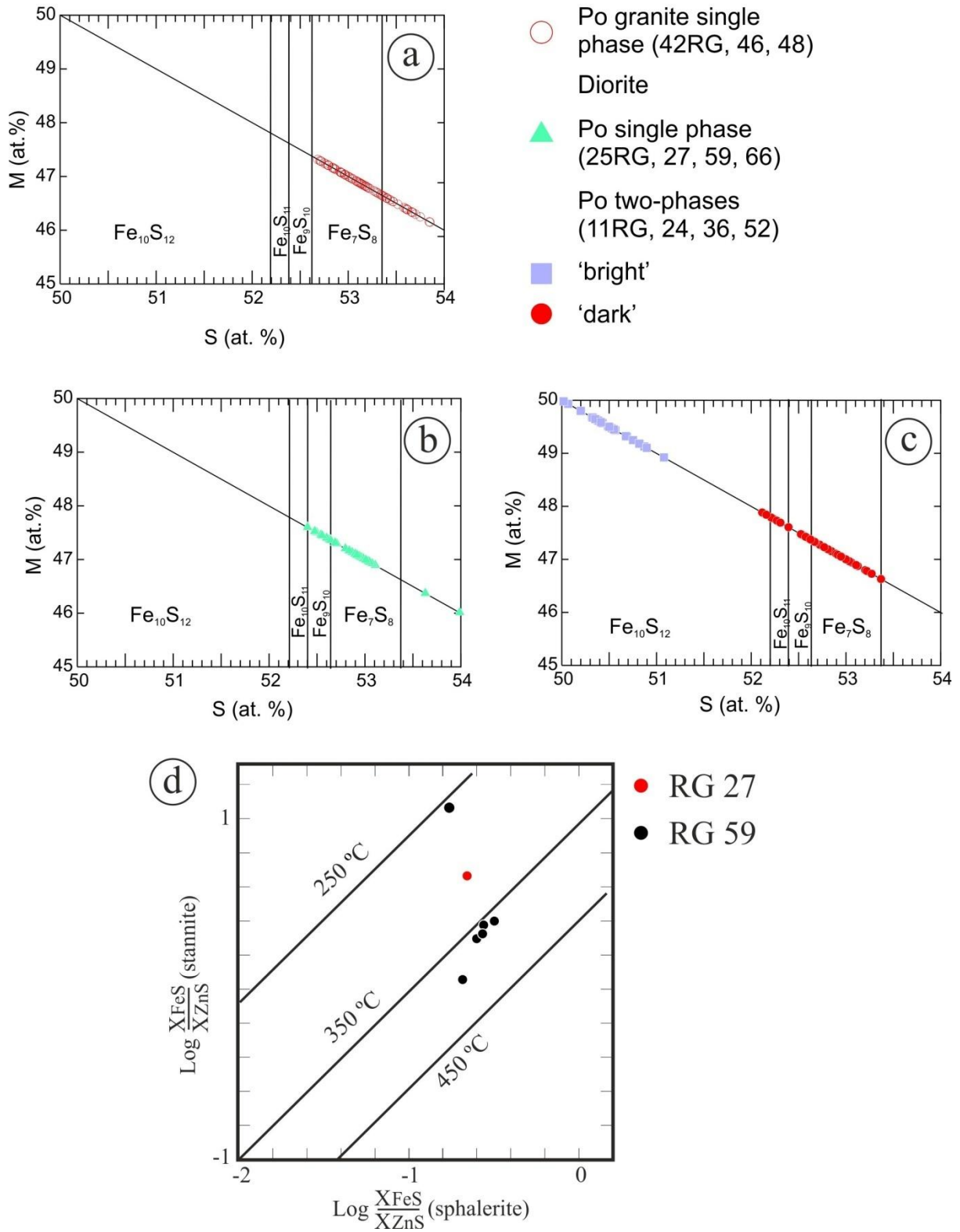


Figure 6

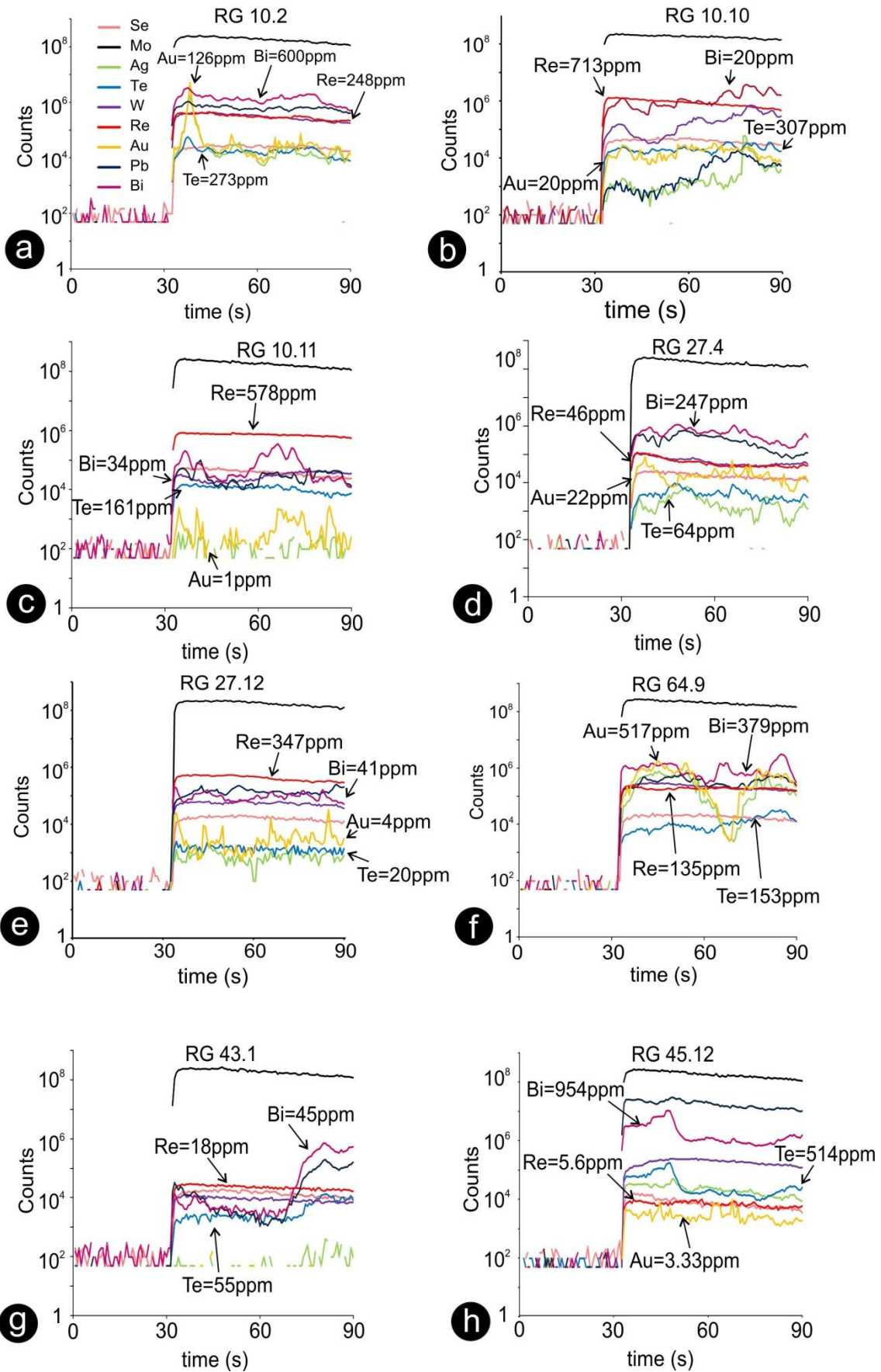


Figure 7

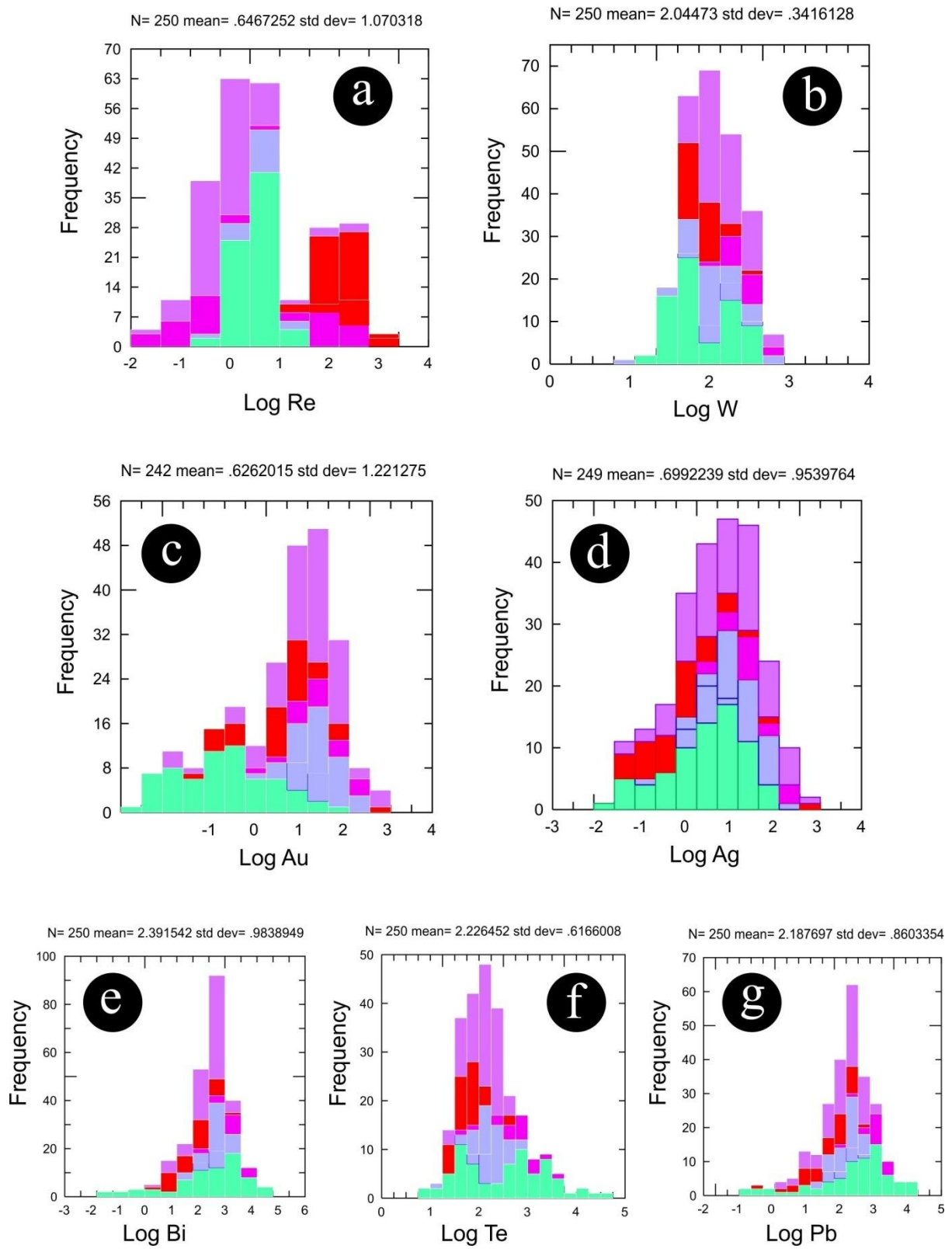


Figure 8

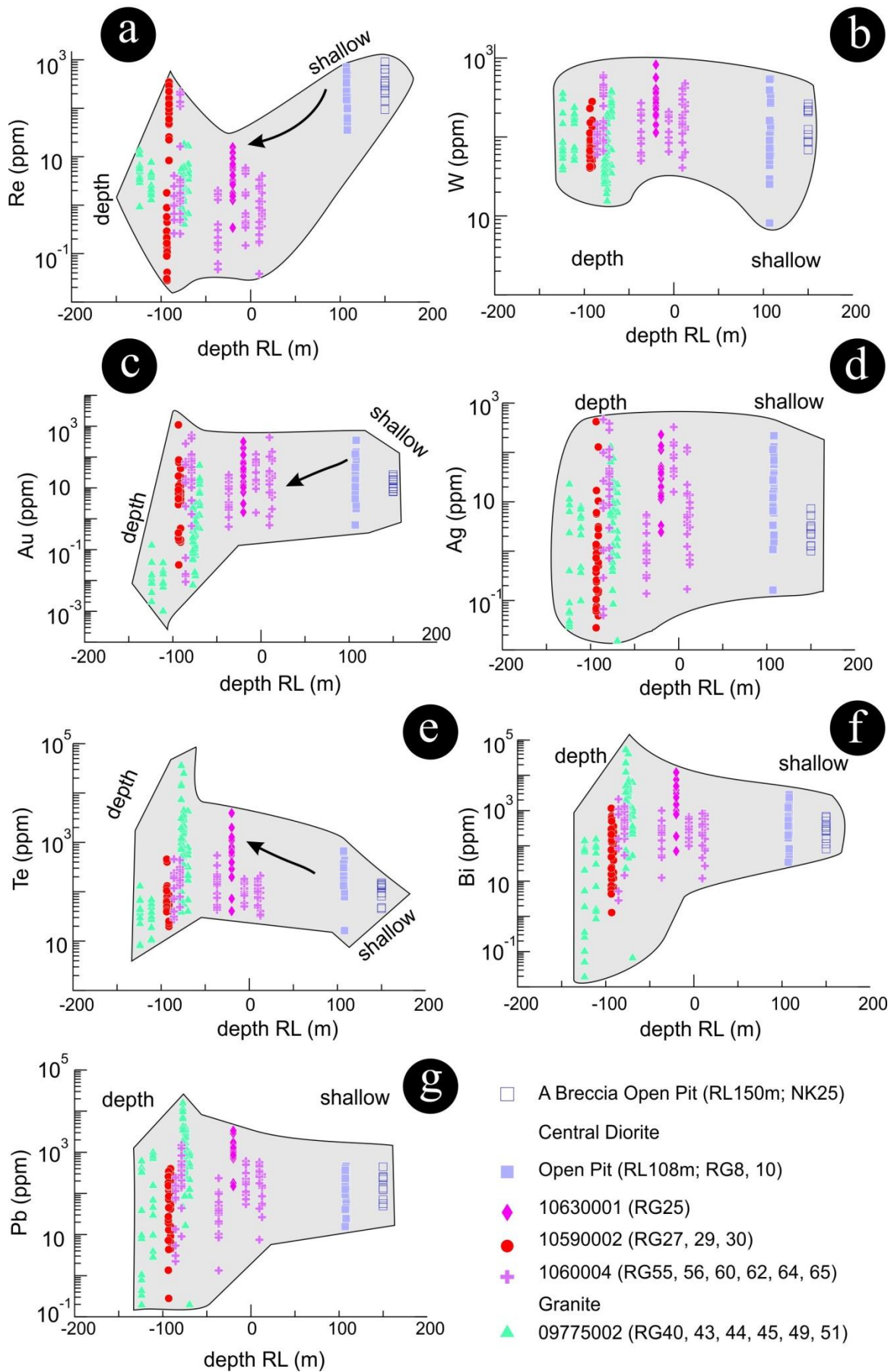


Figure 9

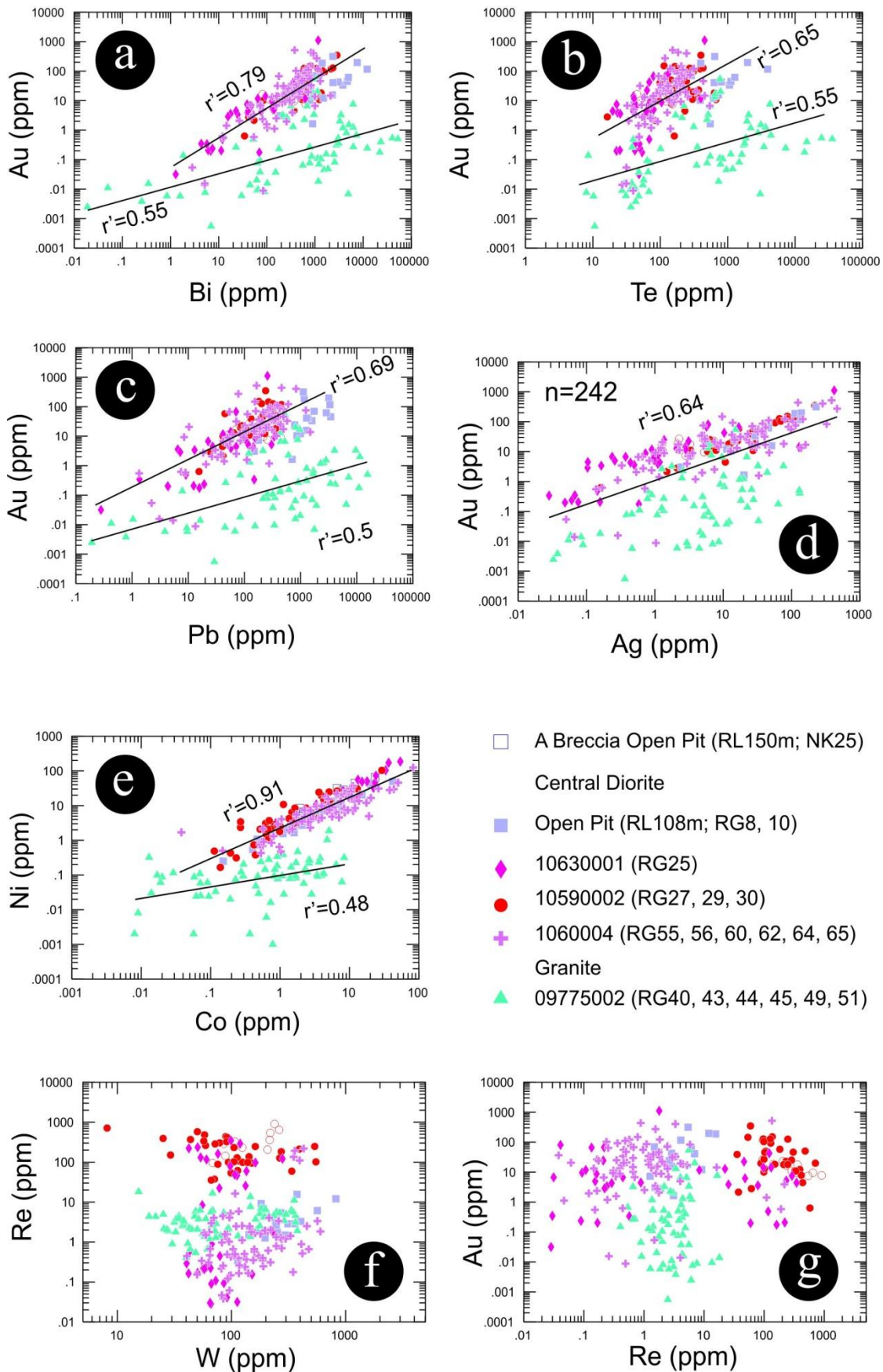
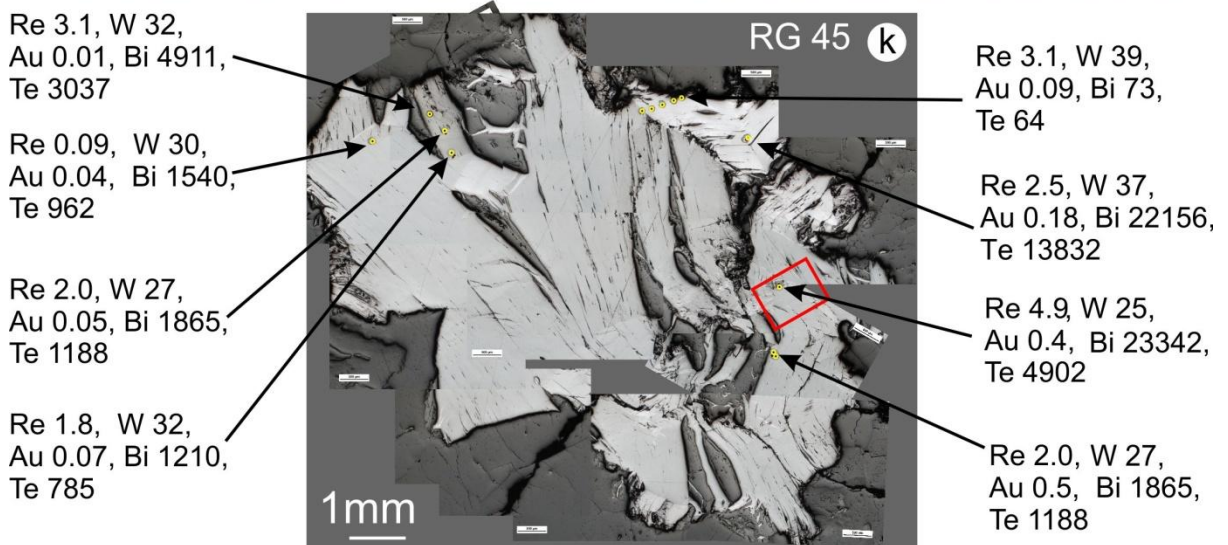
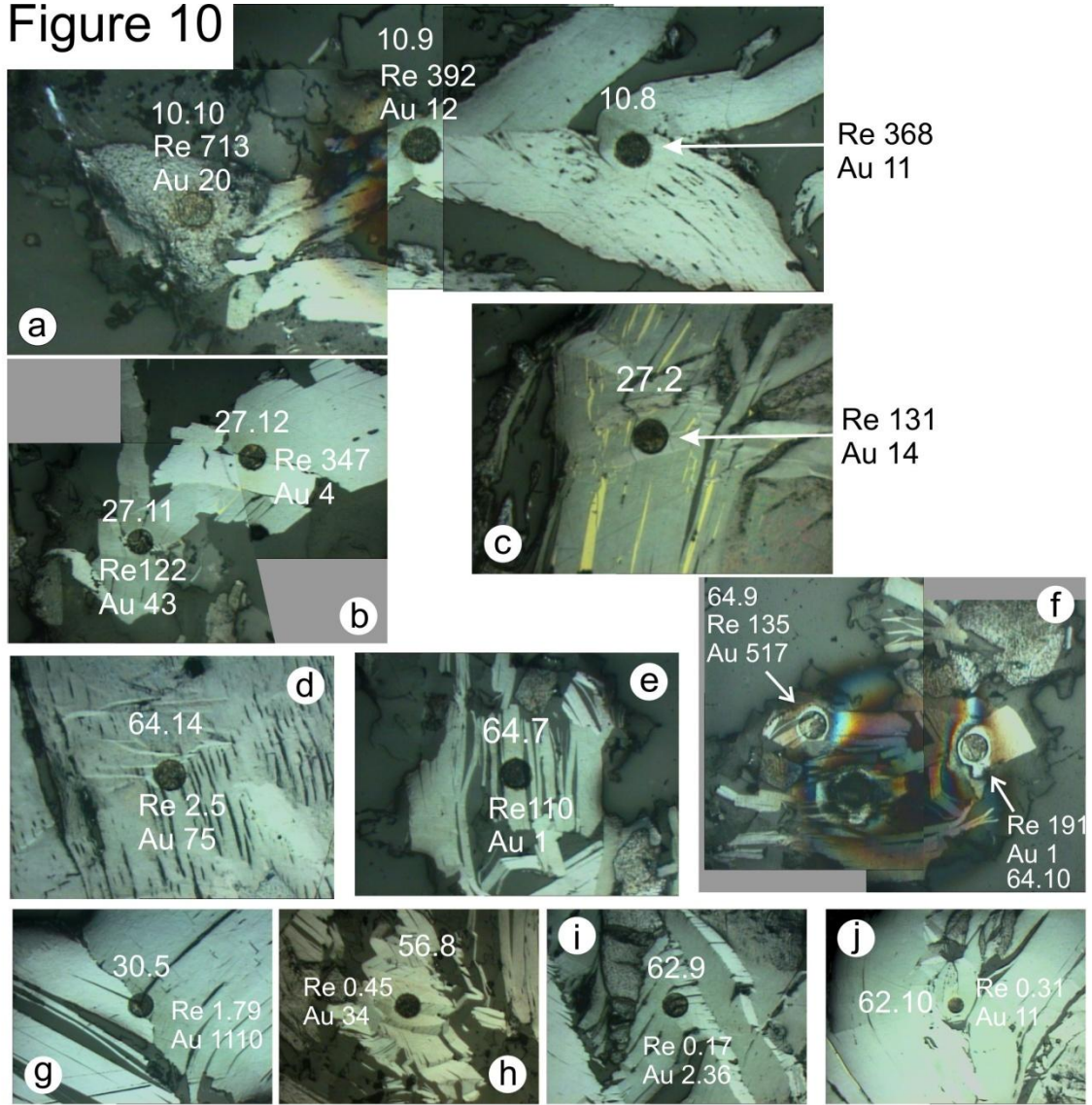
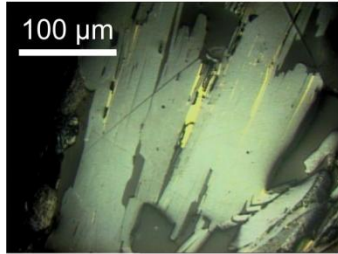


Figure 10





RG 27

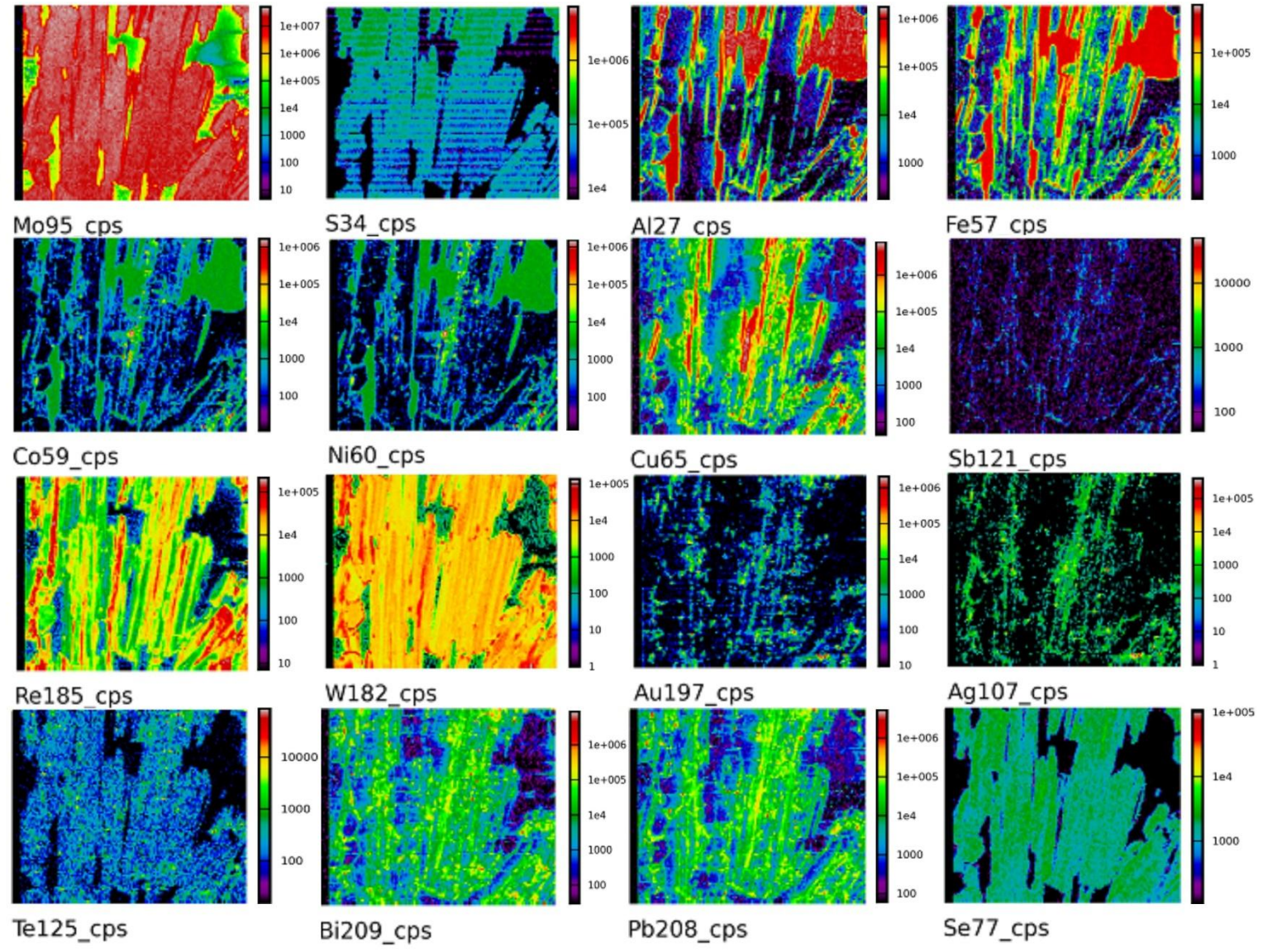
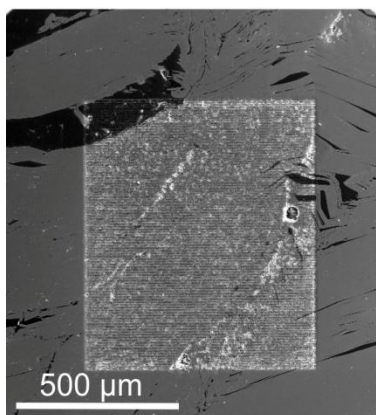


Figure 11



RG45

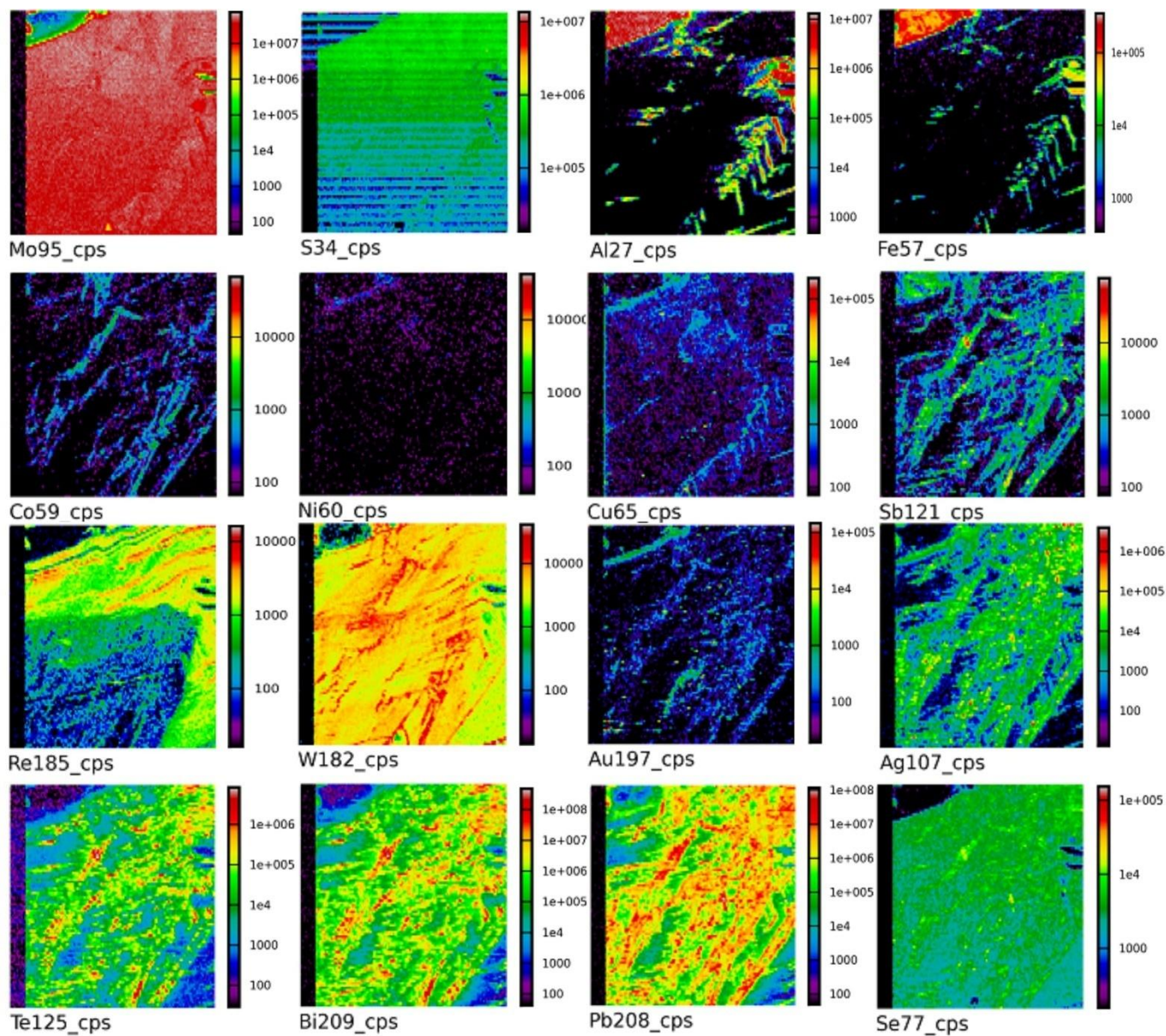


Figure 12

Figure 13

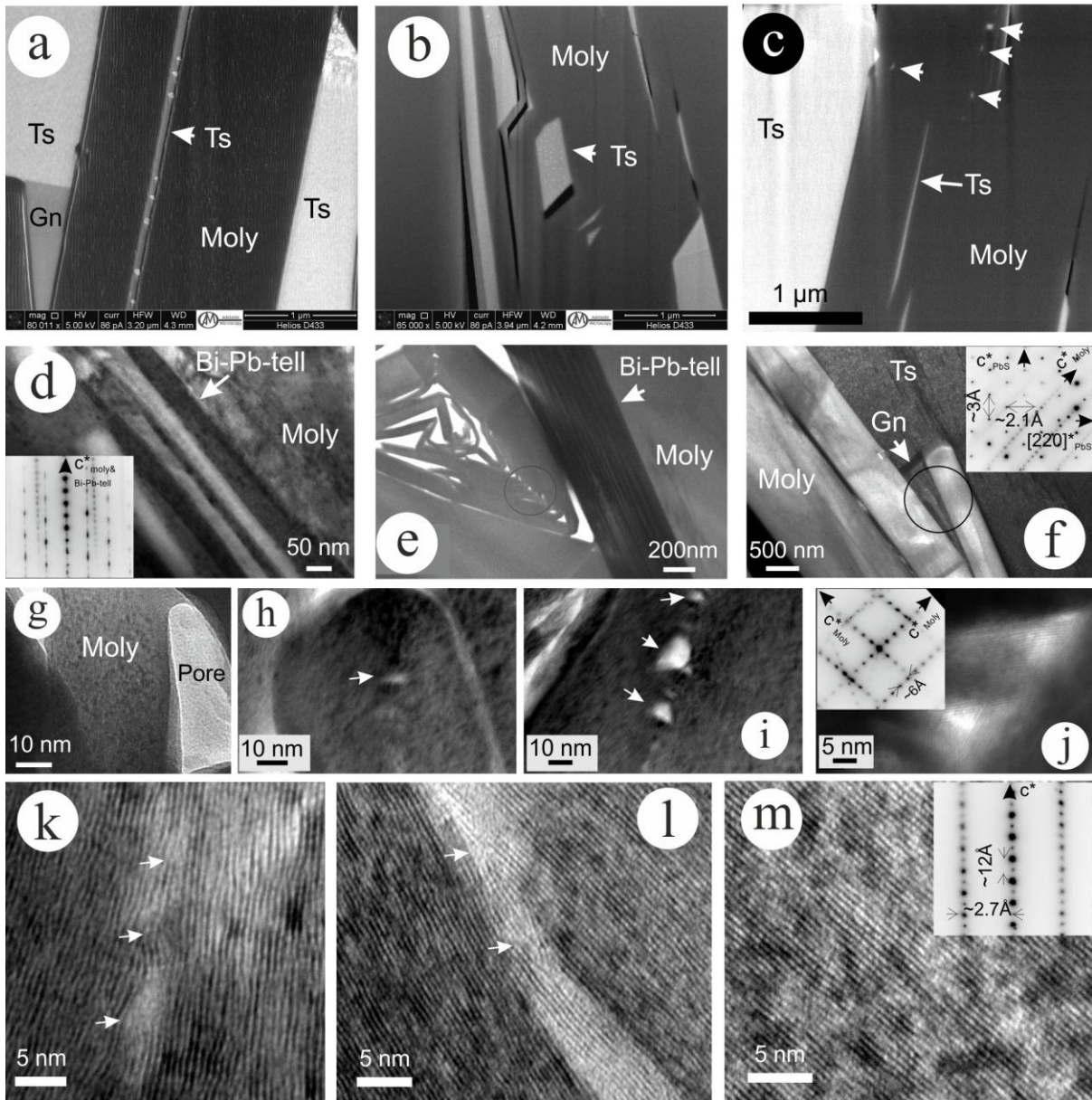
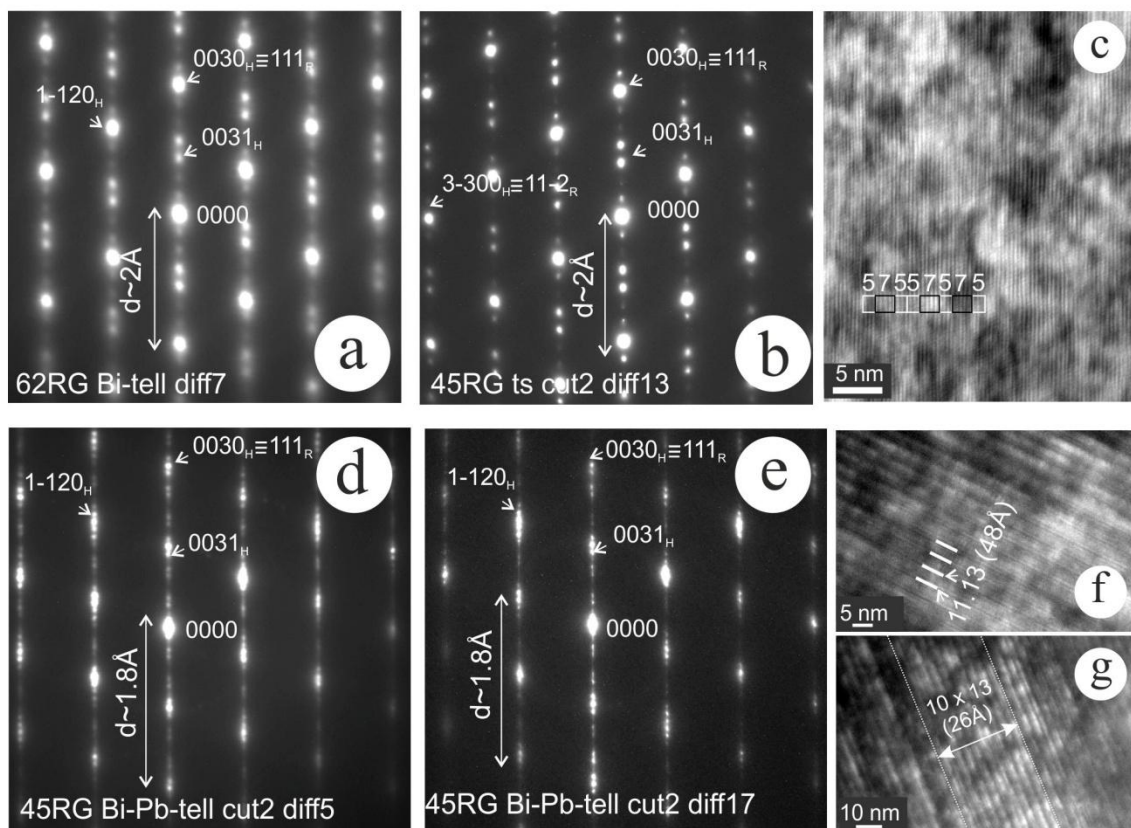


Figure 14



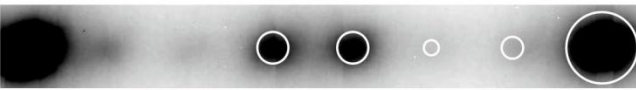
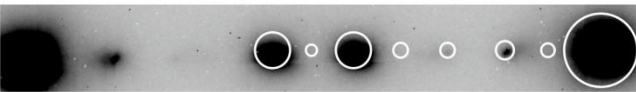
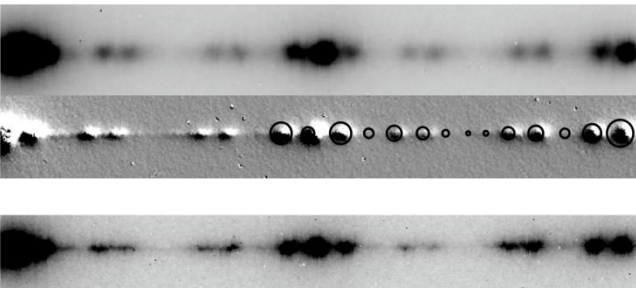
- h**  7 divisions;
stacking sequence 7
 Bi_4X_3 ; X=Te, S, Se;
if X=Te-->pilsenite
- i**  12 divisions;
stacking sequence 5.7
 $\text{Bi}_2\text{Te}_3 + \text{Bi}_4\text{Te}_3 = \text{Bi}_6\text{TE}_6$,
tsumoite
- j**  24 divisions;
stacking sequence 11.13
 $\text{Bi}_2\text{Pb}_3\text{Te}_2\text{S}_4 + \text{Bi}_2\text{Pb}_4\text{Te}_2\text{S}_5$
 $= \text{Bi}_4\text{Pb}_7\text{Te}_4\text{S}_9$ (unnamed)

Figure 15

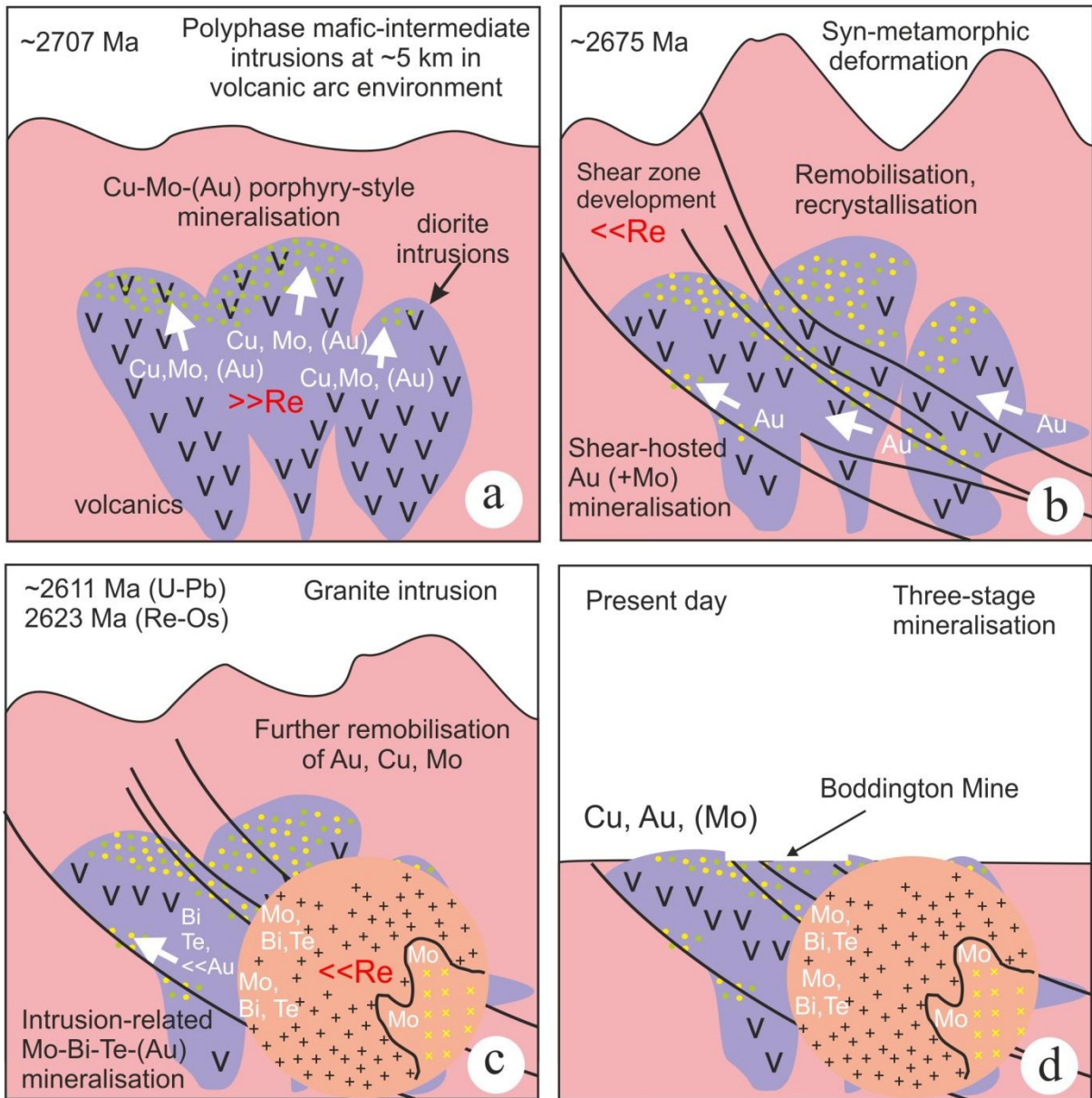


Table 1. Sample description

Sample description	meter	Sample ID	Ore minerals		Gangue/Alteration		SEM	EPMA	LA-ICPMS
			Major&Minor sulphides/ore min.	Au-Ag-Bi-Pb-Te-Se association	Major	Others			
		OPEN PIT							
Veinlet Moly in porph. diorite	RL108	RG8	Moly, Cp, Po		Qz, Ab/Plag, Ep, Bt, Mu	Tit, REE-min	x		x
Patch Moly in bleached diorite	RL108	RG10	Moly	Bi, Bi-tell	Qz, Ep/Clz, Ab, Plag	Cal, Clay min	x	X	x
Sulphide dissem. in diorite	RL108	RG11	Cp, Po, Sph	Hs, Bi, Ag?	Qz, Ep, Ab, KFs, Bt, Chl	Tit, Calc, Sch	x	X	
Sulphide vein in diorite	RL108	RG12	Cp, Po		Plag, Qz, Bt, Ep	Tit, Ap	x		
Large sulph. veinlet in diorite	RL108	RG13	Cp, Po	Hs	Qz, Bt, Ep, Plag		x		
X-sulph. veinlets in bleached diorite	RL108	RG14	Cp, Po		Plag, Qz, Ep, Bt, Mu	Ap, Tit	x		
Sulphide veinlet in diorite	RL108	RG16	Cp, Po		Qz, Plag, Bt, Mu, Ep				
Sulphide veinlet in diorite	RL108	RG17	Cp, Py	Bi, Cls	Qz, Bt, Plag, Ep	Bast, Zr, Tit	x		
Diorite wt large sulphide patches	RL108	RG18	Py, Cp		Qz, Plag, Bt, Ep				
Dolerite	RL108	RG19	Py, Cp		Hbn/Act, Ep, Qz, Plag, <KFs	Ilm, Ru, Tit, Ap	x		
Altered diorite wt Cu staining	RL108	RG67	Cu, Cc		Qz, Plag/Ab, Kfs, Bt, Mu, Ep, Aln, clay min.	Stb, Thor	x		
			WBD 10630001; RL232.59; 9986.19 BGM E/ 10628.24 BGM N						
Fine-gr. diorite, patch/dissem. Cp	252.5	RG21	Cp, Po, Cub, Sph		Qz, Bt, Plag/Ab, Ep, Chl	Tit			
Fine-grained diorite wt sulph. dissem.	254.9	RG23	Cp, Po		Qz, Bt, Plag, Ep				
Fine-grained diorite wt sulph. dissem.	255.9	RG24	Cub, Cp, Po, Pn/Ag-Pn, Sph	Bi, Cls	Bt, Ab/Plag, Qz, Ep	Tit, Zr	x	X	
Felsic patch wt. sulph/Moly in fine-grained diorite	256.4	RG25	Moly, Cp, Po/Lam, Cub, Bn, Cov	Bi-tell, Pb-Bi-tell, Alt, Bi, Ik, El, Te?, Naum	Ab/Plag, Qz, Bt, Ep/Clz	Tit	x	Xx	x
Veinlet in diorite	258.2	RG26	Cp, Po		Ab/Plag, Qz				
			WBD 105900002; RL 241.46; 10022.95 BGM E/ 10591.69 BGM N						
Diorite	339.8	RG27	Moly, Cp, Po, Cub, Sph, Stn, Thio?	Bi	Bt, Qz, Plag, Mu, Chl	Fl, Tit, Stb, Carb	x	Xx	x
Felsic band in diorite	340	RG28	Po, Cub, Moly, Sph	Bi-tell?	Qz, Ab, Ep/Clz, Bt				
Veinlet/diorite	342.1	RG29	Moly		Qz, Plg/Ab, Bt, Ep, Mu	Tit	x	x	x
Veinlet/diorite	342.5	RG30	Moly, Cp	Bi-tell	Qz, Ab/Plag, Ep, Bt, Mu	Tit, Fl, Bi	x		x
X-cutting veinlets in mylonite	344.9	RG31	Cp, Moly, Po, Sph, Mrs?		Qz, Bt, Mu, Ab, Ep/Clz	Tit			
Veinlet in sheared diorite	346.6	RG32	Moly		Plg/Ab, Qz, Bt, Chl	Tit		x	
Felsic zone/diorite	353	RG33	Po, Cp, Cub, Sph, Py		Qz, Ep, Ab/Plag, Bt				
X-cutting veinlets in diorite	353.5	RG34	Cp, Cub, Py		Qz, Bt, Ep				
Diorite wt sulphide dissem.	354.2	RG35	Cp, Po		Bt, Ab/Plag, Ep, Qz				
Diorite	359.5	RG36	Cp, Po, Thio?		Qz, Ab, Bt, Mu, Ep/Clz, Chl	Tit, Sch	x	Xx	

x=EPMA silicate; X=EPMA ore min.; *FIB-TEM

Coordinates given in Boddington Gold Mine Coordinates

RL= Relative level

Table 1 continued

Sample description	meter	Sample ID	Ore minerals		Gangue/Alteration		SEM	EPMA	LA-ICPMS
			Major&Minor sulphides/ore min.	Au-Ag-Bi-Pb-Te-Se association	Major	Others			
			WRD 09775002; RL 278.483; 10560.23 BGM E/ 9763.313 BGM N						
Diorite/veinlet	168.2	RG38	Cp, Po, Sph, Thio?		Bt, Qz, Plag, Ep/Clz	Tit, Cal			
Moly veinlet in granite	402.9	RG40	Moly, Cp		Qz, KFs/Pert, Ab, Clz, Bt, Mu				x
Vein sulphides in granite	410.2	RG42	Po, Cp, Moly, Sph	Hed, Pls?, Bi, Hs, Gn	Qz, Pert, Ab, Mu, Clz, Chl	Sch, Nbts	x	Xx	
Moly/Granite	411.3	RG43	Moly, Po, Cp	Ts, Gn	Qz, Ab, Kfs/Pert,Bt, Mu, Clz/Ep, Aln, Chl	REE-min	x	Xx	x
Granite wt patch Moly	412.6	RG44	Moly, Cp		Qz, Pert, Plag, Bt, Mu, Ep				x
Granite wt large Moly	416.5	RG45	Moly, Cp	Ts, Pb-Bi-tell, Gn, Hs	Ab, Qz	Fl	x	X*x	x
Large sulph. patch/dissem. in granite	419.7	RG46	Po, Cp	Gn	Qz, Ep, Pert, Plag, Bt	Tit		X	
Fluorite vein granite	448.1	RG47	Cp,Po		Qz,Pert, Ab, Bt, Mu, Clz, Chl	Fl		x	
Granite/ Veinlet	448.4	RG48	Cp, Po, Sph, Thio?		Qz, Ep/Clz, Mu, Chl			X	
Fine-grained granite wt patch Moly	477.3	RG49	Moly		Qz, Pert, Ab, Bt, Mu, Ep, Chl	Tit			x
Intrusive dyke	491.9	RG50	Moly, Po, Cub, Sph		Qz, Kfs, Plag/Ab, Bt, Clz, Chl	Tit, Carb		x	
Fine-grained granite wt patch Moly	500.3	RG51	Moly		Qz, Plg/Ab , Ep, Bt, Mu		x		x
			WRD 10600004; RL 278.483; 9996.546 BGM E/ 10602.093 BGM N						
Veinlet in diorite	217.5	RG52	Cp, Po, Py?, Sph	Mld, Au, Bi, Hed, Bi8Te3, Hs	Ab, Plag, Ad, Qz, Act, Ep, Bt, Mu	Tit, Ilm, Ru, Ap, Sch, Nbts	x	X	
Veinlet in diorite	218.2	RG53	Cp, Po		Ab, Qz, Act				
Veinlet in diorite	247.4	RG54	Cp, Po, Moly, Sph, Pn		Qz, Plag, Ep/Clz	Tit			
Veinlet (in diorite)	263.6	RG55	Moly, Cp		Qz, Clz/Ep, Ab				x
Felsic zone in diorite	267.1	RG56	Moly, Cp, Po		Qz, Plag, Bt, Ep/Clz				x
Sulphide veinlet&dissem. In diorite	276.6	RG57	Cp, Po		Qz, Bt, Plag, Ep/Clz, Chl				
Sulphide patch in felsic zone (diorite)	277.6	RG58	Cp, Po, Sph, Py		Qz, Plag, Ep/Clz, Bt	Tit			
Coarse diorite	280	RG59	Cub, Po, Py, Sph, Stn, Cp, Thio, Pn	Bi, Hs, Ltk?	Qz, Plag, Bt, Ep/Clz, Chl	Ap, Sch, Bast	x	X	
Veinlet/diorite	285.15	RG60	Moly, Cp, Py, Sph	El, Au, Bi	Qz, Ab, Clz/Ep, Bt, Mu	Cal, Stb	x		x
Sulph. veinlet in porphyrobl. diorite	318.6	RG61	Cp, Po, Sph, Thio?		Qz,Ab, Ep/Clz				
Coarse Plag.-felsic band /diorite	321.5	RG62	Moly, Cp, Po	Bi-tell (Bi4Te3, Bi2Te), Au, El	Qz, Plag/Ab, Bt, Ep, Mu, Chl	Ilm, Tit, REE-min	x	X*	x
Veinlet in diorite	323.5	RG63	Cp, Po						
Fine-grained diorite	371.3	RG64	Moly, Cp, Sph		Qz, Bt, Plag, Ep/Clz	Tit			x
Veinlet/diorite	379.3	RG65	Moly, Cp, Po, Cub		Qz, Bt, Plag/Ab, Clz				x
Bleached diorite	924.25	RG66	Cp, Po/Lam, Sph	Bi, Hs, Gn, Vol?	Bt, Mu, Ab/Plag, Qz, Ep, Chl	Tit	x	X	

x=EPMA silicate; X=EPMA ore min.; *FIB-TEM

Coordinates given in Boddington Gold Mine Coordinates

RL= Relative level

Table 2. Mineral Abbreviations

Mineral	Abbreviation
Actinolite	Act
Adularia	Ad
Albite	Ab
Allanite	Aln
Altaite	Alt
Apatite	Ap
Bastnasite	Bast
Biotite	Bt
Bismuth tellurides	Bi-tell
Bornite	Bn
Calcite	Cal
Calcium niobate	Nb-Ca
Carbonate	Carb
Chalcocite	Cc
Chalcopyrite	Cp
Chamosite	Cham
Clausthalite	Cls
Clinozoisite	Clz
Covellite	Co
Cubanite	Cub
Electrum	El
Epidote	Ep
Fergusonite	Ferg-(Y-Niobate)
Flourite	Fl
Galena	Gn
Gold	Au
Hedleyite	Hed
Hessite	Hs
Hornblende	Hbn
Ikunolite	Ik
Ilmenite	Ilm
K-feldspar	KFs
Laitakarite	Ltk
Maldonite	Mld
Marcasite	Mrs
Molybdenite	Moly
Muscovite	Mu
Naummanite	Naum
Niobates	Nbts
Native bismuth	Bi
Native copper	Cu
Native silver	Ag
Oligoclase	OI
Pentlandite	Pn
Perthitic feldspar	KFs-Pe
Pilsenite	Pls
Plagioclase	Plag
Pyrite	Py
Pyrrhotite	Po
Quartz	Qz
Rare Earth Minerals	REE-min
Rutile	Ru
Scheelite	Sch
Sphalerite	Sph
Stannite	Stn
Stilbite	Stb
Thiospinel	Thio
Thorite	Tho
Titanite	Tit
Tsumoite	Ts
Volynskite	Vol
Zircon	Zr

Table 3. Microprobe analyses of chlorite group minerals

	RG42		RG47		RG50	RG25	RG29	RG27				RG36	
	mean	SD	mean	SD				mean	SD	mean	SD	mean	SD
Wt.%	n=4		n=4					I n=5		II n=5		n=17	
F	0.32	0.03	0.31	0.02	0.28	0.32	0.39	0.45	0.05	0.30	0.15	0.28	0.05
Na2O	<mdl		0.12	0.24	0.19	<mdl	0.06	<mdl		0.13	0.09	<mdl	
MgO	0.92	0.04	7.44	0.77	4.53	14.78	18.59	9.80	0.20	9.58	7.44	13.61	0.24
Al2O3	21.23	0.51	19.99	0.53	15.20	21.16	18.93	20.59	0.18	15.21	8.72	21.31	0.24
SiO2	22.80	0.84	23.85	0.84	27.74	23.00	27.57	24.10	0.40	20.56	11.46	25.02	0.23
P2O5	<mdl		<mdl		<mdl		<mdl	<mdl		<mdl		0.05	0.03
Cl	0.02	0.02	<mdl		0.02	0.01	<mdl	0.02	0.02	0.02	0.00	0.02	0.02
K2O	0.28	0.34	0.04	0.01	0.10	0.01	0.02	0.01	0.01	0.03	0.04	0.03	0.01
CaO	0.02	0.02	0.02	0.02	0.56	0.01	0.02	0.09	0.07	0.15	0.23	0.03	0.02
TiO2	<mdl		<mdl		0.04	0.00	0.03	0.04	0.02	0.03	0.02	0.03	0.02
Cr2O3	0.01	0.01	<mdl		<mdl	<mdl	<mdl	0.01	0.01	<mdl		0.01	0.01
MnO	0.58	0.12	0.51	0.02	0.23	0.35	0.32	0.68	0.08	0.33	0.22	0.44	0.06
FeO	41.06	1.25	33.52	2.14	37.04	26.39	20.90	31.64	0.24	23.24	14.19	26.16	0.43
Total	87.24		85.80		85.94	86.03	86.82	87.42		86.55		87.02	
Formula, calculated on basis of [(Fe,Mg)10Al2](Al2Si6)O20(OH)16													
Al (total)	2.930	0.037	2.686	0.077	2.070	2.728	2.328	2.687	0.031	2.129	0.144	2.695	0.026
Si	2.670	0.062	2.719	0.086	3.205	2.515	2.876	2.668	0.033	3.127	0.065	2.684	0.024
Aliv	1.330	0.062	1.281	0.086	0.795	1.485	1.124	1.332	0.033	0.873	0.065	1.316	0.024
Total	4.000		4.000		4.000	4.000	4.000	4.000		4.000		4.000	
Alvi	1.600	0.091	1.405	0.027	1.275	1.244	1.204	1.355	0.016	1.256	0.090	1.379	0.020
Mg	0.161	0.009	1.263	0.127	0.779	2.408	2.889	1.617	0.034	0.888	0.163	2.175	0.030
Fe	4.020	0.172	3.195	0.215	3.578	2.413	1.823	2.929	0.032	3.469	0.096	2.347	0.035
Mn	0.057	0.012	0.050	0.002	0.023	0.032	0.028	0.063	0.007	0.067	0.011	0.040	0.006
Ti	-		-		0.004	0.000	0.002	0.003	0.002	0.002	0.002	0.003	0.001
Cr	0.001	0.001	-		-	-	-	0.001	0.001	-		0.001	0.001

Table 3 continued.

Ca	0.002	0.002	0.003	0.002	0.069	0.001	0.002	0.010	0.008	0.090	0.009	0.004	0.003
Na	-		0.027	0.053	0.043	-	0.012	-	0.002	0.020	0.010	-	0.006
K	0.042	0.050	0.005	0.002	0.015	0.001	0.003	0.002	0.001	0.012	0.004	0.004	0.002
Total	5.886		5.950		5.786	6.100	5.963	5.983		5.806		5.960	
F	0.120	0.010	0.110	0.008	0.104	0.112	0.128	0.156	0.017	0.114	0.017	0.096	0.018
Cl	0.004	0.005	-		0.004	0.002	0.001	0.004	0.004	0.004	0.002	0.003	0.003
(OH)	15.876	0.008	15.888	0.007	15.892	15.885	15.871	15.840	0.020	15.882	0.014	15.901	0.017
total	16.000		16.000		16.000	16.000	16.000	16.000		16.000		16.000	
Fe/(Fe+Mg+Mn)	0.95	0.00	0.71	0.03	0.82	0.50	0.38	0.64	0.01	0.78	0.03	0.51	0.006
% clinocllore	3.8	0.1	28.0	3.4	17.8	49.6	60.9	35.1	0.6	20.0	3.2	47.7	0.6
% chamosite	94.9	0.3	70.9	3.4	81.7	49.7	38.5	63.5	0.6	78.5	3.4	51.4	0.6
% pennantite	1.3	0.2	1.1	0.1	0.5	0.7	0.6	1.4	0.2	1.5	0.2	0.9	0.1
Geothermometric calculations													
Cath 1988	366	20	350	28	194	416	300	367	11	219	21	362	8
J 1991	386	20	362	29	211	421	302	377	11	235	21	367	8

using formulae from Caritat et al. (1993)

Cath = Cathelineau (1988)

J = Jowett (1991) - applies when $Fe/(Mg+Fe) < 0.6$

Bolding on geothermometric calculated values signifies chosen calibrations

Detection Limits (wt%) Al 0.01, Ca 0.02, Cr 0.01, Cl 0.02, F 0.17, Fe 0.03, K 0.01, Mn 0.03, Mg 0.02, Na 0.04, P 0.03, Si 0.02, Ti 0.02

Table 4. Electron probe analyses of pyrrhotite

	RG52				RG24			RG11				RG25		RG27			
	mean	SD	mean	SD	mean	SD	LIGHT	mean	SD	mean	SD	mean	SD	mean	SD		
	DARK n=9		LIGHT n=11		DARK n=3		LIGHT	DARK n=17		LIGHT n=15		no lam. N=3		no lam n=4		no lam n=15	
Cu	0.07	0.06	0.08	0.10	0.21	0.14	0.00	0.06	0.04	0.05	0.05	0.05	0.01	0.22	0.09	0.07	0.05
Fe	59.41	0.38	61.84	0.69	59.34	0.40	61.45	60.08	0.57	61.95	0.59	61.79	0.17	59.61	0.49	58.87	1.62
Co	0.03	0.03	0.00	0.01	0.00	0.00	0.00	0.00	0.01	0.00	0.00	0.00	0.00	0.00	0.00	0.00	0.00
Ni	0.20	0.12	0.03	0.07	0.02	0.02	0.00	0.19	0.05	0.03	0.08	0.03	0.01	0.03	0.01	0.09	0.09
S	38.17	0.26	36.51	0.85	38.68	0.38	36.84	38.42	0.23	36.60	0.55	36.26	0.16	38.88	0.27	38.52	1.61
Total	97.87		98.46		98.25		98.29	98.76		98.64		98.13		98.75		97.55	
Formulae (2 a.p.f.u.)																	
Cu	0.001	0.001	0.001	0.001	0.003	0.002	0.000	0.001	0.000	0.001	0.001	0.001	0.000	0.003	0.001	0.001	0.001
Fe	0.941	0.006	0.985	0.017	0.934	0.006	0.978	0.944	0.004	0.985	0.012	0.988	0.001	0.934	0.006	0.933	0.031
Co	0.000	0.000	0.000	0.000	0.000	0.000	0.000	0.000	0.000	0.000	0.000	0.000	0.000	0.000	0.000	0.000	0.000
Ni	0.003	0.002	0.000	0.001	0.000	0.000	0.000	0.003	0.001	0.000	0.001	0.000	0.000	0.000	0.000	0.001	0.001
Total M	0.947		0.987		0.939		0.978	0.948		0.987		0.990		0.938		0.937	
S	1.053	0.006	1.013	0.017	1.061	0.005	1.021	1.051	0.005	1.013	0.011	1.010	0.001	1.061	0.008	1.063	0.030
M/S	0.90	0.01	0.97	0.03	0.88	0.01	0.96	0.90	0.01	0.97	0.02	0.98	0.00	0.88	0.01	0.88	0.05

	RG36		RG59		RG66		RG42		RG46		RG48			
	mean	SD	mean	SD	mean	SD	mean	SD	mean	SD	mean	SD		
	DARK n=24		LIGHT n=7		no lam n=2		no lam n=14		no lam n=20		no lam n=18		no lam n=37	
Cu	0.10	0.08	0.25	0.20	0.06	0.03	0.14	0.10	0.07	0.05	0.01	0.02	0.03	0.03
Fe	59.89	0.45	61.91	0.56	59.18	0.76	59.66	0.32	59.24	0.73	59.21	0.48	59.33	0.60
Co	0.00	0.00	0.00	0.00	0.00	0.00	0.04	0.02	0.00	0.00	0.02	0.01	0.05	0.01
Ni	0.05	0.05	0.01	0.01	0.01	0.01	0.03	0.02	0.01	0.01	0.02	0.01	0.01	0.01
S	38.60	0.28	36.67	0.49	39.05	0.75	38.28	0.20	38.93	0.33	38.57	0.16	38.60	0.80
Total	98.64		98.84		98.31		98.15		98.25		97.82		98.02	
Formulae (2 a.p.f.u.)														
Cu	0.001	0.001	0.004	0.003	0.001	0.000	0.002	0.001	0.001	0.001	0.000	0.000	0.000	0.000
Fe	0.941	0.005	0.982	0.011	0.929	0.016	0.943	0.004	0.931	0.008	0.936	0.005	0.936	0.012
Co	0.000	0.000	0.000	0.000	0.000	0.000	0.001	0.000	0.000	0.000	0.000	0.000	0.001	0.000
Ni	0.000	0.000	0.000	0.000	0.000	0.000	0.000	0.000	0.000	0.000	0.000	0.000	0.000	0.000
Total M	0.943		0.986		0.931		0.946		0.933		0.938		0.939	
S	1.057	0.006	1.013	0.011	1.068	0.016	1.053	0.004	1.066	0.008	1.062	0.005	1.061	0.012
M/S	0.89	0.01	0.97	0.02	0.87	0.03	0.90	0.01	0.88	0.01	0.88	0.01	0.88	0.02

Detection limits (wt%) Cu 0.06, Co 0.04, Ni 0.03, Fe 0.05, S 0.06

Ag, As, Sb and Se were also measured; all were <mdl (0.14, 0.15, 0.09 and 0.15 wt%, respectively)

Table 5. Electron probe microanalyses of sphalerite and stannite

	S P H A L E R I T E												S T A N N I T E							
	RG52		RG24		RG59		RG11		RG66		RG27		RG42		RG48		RG59		RG27	
	mean	SD	mean	SD	mean	SD	mean	SD	mean	SD	mean	SD	mean	SD	mean	SD	mean	SD	mean	SD
(Wt.%)	n=22		n=4		n=9		n=12		n=22		n=6		n=9		n=15		n=10		n=2	
S	33.40	0.36	33.60	0.16	33.35	32.91	33.43	0.27	33.29	0.20	33.77	0.19	33.48	0.47	33.27	0.21	30.70	0.70	29.78	0.06
Mn	0.05	0.02	<mdl		0.07	0.00	0.04	0.02	0.05	0.02	0.03	0.02	0.05	0.03	<mdl		<mdl		<mdl	
Fe	10.22	0.31	11.78	0.73	10.70	1.24	9.59	0.58	9.83	0.29	10.39	0.53	10.13	0.33	8.11	0.14	18.05	4.46	16.19	0.84
Cu	0.28	0.55	0.96	1.43	1.72	1.78	0.06	0.06	0.27	0.83	0.34	0.30	0.36	0.37	0.04	0.03	24.92	1.88	28.62	1.59
Zn	54.34	0.91	51.81	0.83	52.42	2.18	55.69	0.70	54.69	1.35	54.77	0.36	55.08	0.51	56.47	0.25	5.93	3.06	1.59	1.65
Cd	0.26	0.05	0.29	0.05	0.35	0.11	0.30	0.06	0.71	0.05	0.22	0.05	0.29	0.07	1.16	0.06	<mdl		<mdl	
In	<mdl		<mdl		<mdl		<mdl		<mdl		<mdl		<mdl		<mdl		1.58	1.35	0.13	0.12
Sn	<mdl		<mdl		<mdl		<mdl		<mdl		<mdl		<mdl		<mdl		18.44	5.13	23.33	1.26
Total	98.56		98.44		98.61		99.11		98.83		99.52		99.37		99.04		99.63		99.65	
Formula (2 a.p.f.u.)																				
Mn	0.001	0.000	0.000	0.000	0.001	0.000	0.001	0.000	0.001	0.000	0.001	0.000	0.001	0.000	-		-		-	
Fe	0.177	0.005	0.204	0.013	0.172	0.053	0.166	0.010	0.171	0.005	0.179	0.009	0.175	0.006	0.141	0.002	1.333	0.306	1.226	0.060
Cu	0.004	0.008	0.015	0.022	0.029	0.028	0.001	0.001	0.004	0.013	0.005	0.004	0.005	0.006	0.001	0.001	1.624	0.139	1.905	0.100
Zn	0.805	0.014	0.766	0.010	0.895	0.372	0.823	0.009	0.811	0.019	0.804	0.005	0.811	0.005	0.839	0.003	0.376	0.196	0.103	0.107
Cd	0.002	0.000	0.002	0.000	0.003	0.001	0.003	0.000	0.006	0.000	0.002	0.000	0.002	0.001	0.010	0.001	-		-	
In	-		-		-		-		-		-		-		-		0.057	0.048	0.005	0.004
Sn	-		-		-		-		-		-		-		-		0.646	0.188	0.831	0.047
Total M	0.990	0.007	0.987	0.009	1.103	0.329	0.993	0.004	0.993	0.004	0.990	0.002	0.995	0.008	0.992	0.004	4.037	0.028	4.071	0.004
S	1.010	0.007	1.013	0.009	0.897	0.329	1.007	0.004	1.007	0.004	1.010	0.002	1.005	0.008	1.008	0.004	3.963	0.028	3.929	0.004
%ZnS	81.3	1.1	77.58	0.92	79.60	6.63	82.85	1.00	81.68	1.78	81.18	0.47	81.56	0.74	84.64	0.23				
%CdS	0.2	0.0	0.25	0.04	0.31	0.09	0.26	0.05	0.62	0.05	0.19	0.04	0.25	0.06	1.01	0.05				
%FeS	17.9	0.6	20.67	1.41	17.15		16.70	1.01	17.19	0.54	18.03	0.90	17.55	0.56	14.23	0.22				
logX _{FeS} /X _{ZnS}	-0.66		-0.58		-0.73		-0.70		-0.68		-0.65		-0.67		-0.77		0.55		0.08	
Coexisting sphalerite-stannite pairs																				
	logX _{FeS} /X _{ZnS} sphalerite										logX _{FeS} /X _{ZnS} stannite									
	RG59/116	-0.52	RG59/115	-0.30	Detection limits (wt%) Cu 0.06, Zn 0.04, Mn 0.03, Cd 0.09, In 0.12, Sn 0.11, S 0.06															
	RG59/121	-0.67	RG59/122	0.03	Ag was also measured but was <mdl (0.14 wt%)															
	RG59/123	-0.58	RG59/124	0.19																
	RG59/126	-0.60	RG59/125	0.31																
	RG59/133	-0.59	RG59/134	0.34																
	RG59/135	-0.75	RG59/136	1.08																
	RG27/153	-0.64	RG27/152	0.66																

Table 6. Electron probe microanalyses of gold/electrum, maldonite and hessite

	NATIVE GOLD / ELECTRUM									MALDONITE			HESSITE	
	25RG1	25RG33	62RG35	62RG37	62RG38	62RG44	52RG54	52RG56	52RG67	52RG59	52RG60	52RG61	52RG49	52RG63
Au	57.32	85.68	86.71	95.55	95.70	86.54	92.92	70.21	93.35	62.63	62.46	60.53	<mdl	<mdl
Ag	35.48	7.36	7.38	5.56	5.87	10.01	4.62	3.81	1.92	0.52	0.54	0.30	64.62	62.93
Bi	<mdl	<mdl	<mdl	0.19	0.24	<mdl	0.42	18.34	0.43	35.69	35.65	37.28	<mdl	0.39
Te	0.10	<mdl	<mdl	<mdl	<mdl	<mdl	<mdl	<mdl	<mdl	<mdl	<mdl	0.64	37.29	37.53
S	<mdl	<mdl	<mdl	<mdl	<mdl	<mdl	<mdl	<mdl	<mdl	<mdl	<mdl	<mdl	0.17	<mdl
Total	92.90	93.05	94.09	101.31	101.81	96.55	97.95	92.37	95.70	98.85	98.64	98.74	102.08	100.84
Formulae calculated to 1 a.p.f.u.										3 a.p.f.u.			3 a.p.f.u.	
Au	0.469	0.864	0.865	0.902	0.897	0.826	0.913	0.743	0.960	1.933	1.930	1.868	-	-
Ag	0.530	0.136	0.134	0.096	0.100	0.174	0.083	0.074	0.036	0.030	0.030	0.017	2.000	1.983
Bi	0.000	0.000	0.000	0.002	0.002	-	0.004	0.183	0.004	1.038	1.038	1.084	-	0.006
Te	0.001	-	-	-	-	-	-	-	-	-	-	0.031	0.976	0.999
S	-	-	-	-	-	-	-	-	-	-	-	-	0.018	-

Detection limits (wt%) Au 0.37, Ag 0.16, Bi 0.15, Te 0.10, S 0.06

Se was also measured but was <mdl (0.15 wt%)

Analyses with low totals (small grain size) are retained to represent compositional variation

Table 7. Electron probe microanalyses of bismuth telluride species

	TSUMOITE				TSUMOITE (+S)		Bi ₄ (Te,S) ₅ RG43 (in MoS ₂)		Bi ₄ (Te,S) ₅	HEDLEYITE		Bi ₂ Te		Bi ₈ Te ₃	HED	Bi ₂ Te
	RG45 (in MoS ₂)		RG43 (in MoS ₂)		RG43 (in MoS ₂)				RG62	RG52		RG52		RG52	RG42	
	mean	SD	mean	SD	mean	SD	mean	SD		mean	SD	mean	SD			
(wt. %)	n=25		n=8		n=2		n=5			n=4		n=4				
Ag	<mdl		<mdl		<mdl		<mdl		<mdl	<mdl	<mdl	<mdl		<mdl	0.15	0.66
Pb	0.89	0.24	1.27	0.09	1.21	0.03	0.91	0.20	0.60	<mdl	<mdl	<mdl		0.08	<mdl	
Bi	61.02	1.10	62.92	0.50	60.84	0.47	59.35	0.68	61.06	79.09	0.92	75.45	0.70	78.50	84.48	75.34
Sb	0.28	0.11	<mdl		<mdl		<mdl		0.26	0.25	0.06	0.23	0.07	0.17	<mdl	
Te	36.64	0.72	35.78	0.50	34.53	1.02	35.82	0.30	29.89	19.82	0.70	22.62	0.70	17.64	18.79	27.49
Se	0.15	0.05	0.20	0.04	0.20	0.02	0.17	0.05	0.20	<mdl		<mdl		<mdl	<mdl	
S	0.52	0.50	0.31	0.24	1.59	0.31	2.18	0.39	3.98	<mdl		<mdl		0.08	<mdl	
Total	99.50		100.48		98.37		98.42		95.99	99.16		98.31		96.47	103.42	103.48
Formulae	(2 a.p.f.u.)						(9 a.p.f.u.)		(9 a.p.f.u.)	(10 a.p.f.u.)		(3 a.p.f.u.)		(11 a.p.f.u.)	(10 a.p.f.u.)	
Ag	-		-		-		-		-	-	-	-	-	-	0.025	0.031
Pb	0.014	0.004	0.020	0.002	0.019	0.000	0.062	0.014	0.039	-		-		0.008	-	
Bi	0.969	0.025	1.004	0.011	0.940	0.007	3.998	0.095	3.996	7.023	0.063	1.994	0.019	7.945	7.287	1.847
Sb	0.005	0.004	-		-		-		0.029	0.038	0.010	0.011	0.003	0.030	-	
Total M	0.988	0.024	1.025	0.013	0.959	0.007	4.065	0.102	4.064	7.066	0.059	2.011	0.018	7.983	7.312	1.879
Te	0.953	0.027	0.935	0.016	0.874	0.025	3.951	0.059	3.203	2.882	0.098	0.979	0.016	2.924	2.655	1.104
Se	0.006	0.002	0.008	0.001	0.008	0.001	0.030	0.009	0.035	-		-		-	-	
S	0.053	0.050	0.032	0.025	0.160	0.031	0.954	0.154	1.697	-		0.003	0.002	0.056	-	
Total S,Se,Te	1.012	0.024	0.975	0.013	1.041	0.007	4.935	0.102	4.936	2.934	0.059	0.989	0.018	3.017	2.688	1.121
	PHASE 'C'		ALEKSITE		SADDLEBACKITE											
			RG45													
(wt. %)																
Pb	12.28		21.94	17.77	37.42											
Bi	53.30		43.75	45.11	31.58											
Te	32.91		25.38	26.99	18.22											
Se	0.31		0.75	0.83	0.72											
S	1.86		6.50	6.46	9.74											
Total	100.73		98.36	97.20	97.70											
Formulae	(10 a.p.f.u.)		(7 a.p.f.u.)		(9 a.p.f.u.)											
Pb	0.934		1.020	0.828	2.064											
Bi	4.018		2.017	2.082	1.726											
Total M	4.961		3.041	2.914	3.793											
Te	4.063		1.916	2.041	1.631											

Detection limits (wt%) Ag 0.15, Pb 0.20, Bi 0.15, Sb 0.09, Te 0.10, Se 0.15, S 0.06

Se	0.061	0.091	0.101	0.104
S	0.915	1.952	1.944	3.472
Total S,Se,Te	5.039	3.959	4.086	5.207

Table 8. Summary of LA-ICP-MS spot analyses of molybdenite

SampleName		Fe	Co	Ni	Cu	Zn	As	Se	Ag	Sn	Sb	Te	W	Re	Au	Tl	Pb	Bi	U
NK25 n=10	mean	10360	8.4	25	128	17	19	698	3.0	1.5	13	108	162	374	15	3.6	183	343	0.37
	SD	10940	8.0	21	97	16	16	111	2.0	1.4	9.0	39	73	252	6.8	3.9	121	210	0.91
	max	30682	24	66	391	47	48	930	7.2	4.9	30	151	262	905	27	14	440	685	2.9
	min	813	1.7	5.8	68	2.7	4.9	516	1.0	0.11	2.9	45	69	94	7.5	0.31	50	82	<mdl
RG8 n=20	mean	5499	7.6	12	996	44	4.7	553	51	2.8	5.3	188	153	122	78	0.85	194	876	0.04
	SD	8112	9.4	13	1431	48	3.2	95	53	3.7	4.6	117	120	99	81	0.87	129	803	0.03
	max	35218	42	49	6269	182	15	711	219	17	15	432	549	481	347	3.0	458	2855	0.11
	min	253	0.47	1.1	54	3.3	1.3	414	1.5	0.24	0.17	16	58	36	2.1	0.04	25	42	<mdl
RG10 n=15	mean	3336	2.0	3.6	15	14	13	1149	19	0.95	6.7	295	122	350	24	1.6	217	530	0.03
	SD	3947	1.7	3.5	12	13	8.9	208	28	1.0	6.6	163	146	146	30	1.6	128	354	0.04
	max	12669	5.6	12	51	43	32	1543	115	3.6	22	670	536	713	126	5.3	402	1338	0.12
	min	58	0.15	0.25	2.7	1.5	3.6	779	0.16	0.12	0.33	133	8.1	150	0.63	0.03	16	34	<mdl
RG25 n=17	mean	26853	17	53	158	79	11	603	57	3.2	8.0	865	306	4.7	70	3.5	1532	2929	0.41
	SD	40893	14	54	280	106	5.8	94	62	2.4	5.5	922	172	4.2	87	2.3	1051	3076	0.47
	max	141646	54	187	1201	343	24	740	229	8.3	19	3912	823	16	314	8.5	3440	12108	1.4
	min	610	0.87	3.1	6.6	4.6	3.3	462	2.4	0.24	0.79	40	113	0.34	1.6	0.29	150	71	<mdl
RG27 n=16	mean	4797	4.9	17	1261	43	5.1	485	9.8	13	0.75	46	104	126	9.4	0.50	105	113	0.08
	SD	3429	7.3	25	1326	46	3.8	132	32	24	1.0	22	59	101	11	0.40	116	118	0.13
	max	12591	29	104	4267	165	15	786	129	89	4.2	85	280	347	43	1.2	399	363	0.43
	min	3.9	0.14	0.17	2.8	0.4	1.4	292	0.0	0.1	0.02	20	42	8.4	0.17	0.01	4.4	6.0	<mdl
RG29 n=10	mean	1575	0.85	2.2	228	8.0	8.8	413	3.1	11	0.72	107	81	0.16	25	0.12	120	287	1.2
	SD	1632	0.92	1.7	406	6.4	7.6	35	5.4	21	0.74	107	29	0.12	32	0.20	124	280	3.2
	max	4606	3.1	4.7	1137	22	21	493	17	68	2.6	399	152	0.44	81	0.67	342	694	10
	min	2.6	0.11	0.31	0.65	1.4	1.5	368	<mdl	0.23	0.04	42	50	0.03	0.03	0.01	0.28	1.3	<mdl
RG30 n=10	mean	4045	1.2	4.8	96	11	5.2	328	42	6.5	0.9	105	79	0.43	116	0.38	96	186	0.17
	SD	6790	1.4	7.3	123	15	7.7	30	133	7.7	1.3	126	57	0.55	349	0.64	91	359	0.45
	max	22554	5.1	25	362	52	26	387	421	22	4.1	456	230	1.8	1110	2.1	257	1166	1.5
	min	27	0.44	0.38	1.3	1.2	0.5	275	<mdl	0.16	0.08	39	40	0.03	0.24	0.01	1.4	4.4	0.003

**Table 8
continued.
Sample**

Name		Fe	Co	Ni	Cu	Zn	As	Se	Ag	Sn	Sb	Te	W	Re	Au	Tl	Pb	Bi	U
RG40 n=12	mean	5549	3.0	0.27	202	12	6.0	208	6.5	7.4	1.7	723	206	5.2	11	1.9	428	1014	6.9
	SD	6920	2.5	0.52	360	16	4.7	98	6.5	7.3	1.4	1144	114	3.9	15	1.8	330	1680	9.8
	max	24128	7.8	1.9	1242	50	17	357	22	22	4.6	4256	378	17	53	5.2	963	6195	33
	min	<mdl	<mdl	<mdl	0.77	0.30	0.45	88	0.02	0.08	0.02	40	35	0.66	<mdl	<mdl	0.19	0.07	<mdl
RG43 n=12	mean	2544	2.4	0.19	400	165	4.9	444	17	2.5	2.4	4042	92	4.0	0.86	7.9	1863	6628	1.3
	SD	2522	2.4	0.28	513	522	5.0	106	20	3.3	2.0	6624	94	4.8	0.90	8.3	1211	10808	2.8
	max	6257	8.4	1.0	1433	1820	17	553	76	11	6.8	24705	335	18	3.3	25	4022	40308	9.4
	min	<mdl	0.01	<mdl	1.8	0.20	<mdl	184	0.08	0.09	0.03	55	15	0.40	0.01	0.05	16	45	<mdl
RG44 n=10	mean	2088	1.1	0.21	9.1	9.0	4.3	247	1.3	8.3	1.4	1159	69	2.4	0.16	2.5	449	1968	5.4
	SD	2401	0.73	0.14	7.5	8.7	3.1	38	1.1	8.1	0.87	924	40	1.4	0.11	1.7	277	1698	8.2
	max	7084	2.7	0.47	24	30	11	287	3.7	29	3.3	3459	165	4.4	0.36	6.6	910	6255	27
	min	113	0.07	0.03	2.4	1.7	0.4	158	0.16	0.21	0.21	356	19	0.71	0.02	0.35	85	775	0.27
RG45 n=16	mean	420	0.56	0.06	2.7	1.9	2.0	347	32	1.7	4.6	5093	77	2.9	0.61	2.4	4774	7885	0.50
	SD	765	1.0	0.07	4.6	2.7	2.5	90	43	3.7	5.5	9435	109	1.3	1.0	3.6	4866	14166	1.4
	max	2896	3.6	0.23	17	9.6	9.0	580	132	11	17	35599	364	5.6	3.3	11	15602	52682	5.1
	min	1.6	0.01	<mdl	0.38	0.33	0.10	213	0.78	0.06	0.13	38	25	0.66	<mdl	0.02	46	23	<mdl
RG49 n=10	mean	854	0.44	0.08	2.1	2.5	4.3	205	3.5	6.1	0.18	36	124	3.2	0.01	1.1	281	51	3.9
	SD	1419	0.48	0.07	1.9	3.0	3.0	87	2.8	7.3	0.20	20	68	1.9	0.01	1.3	388	52	4.1
	max	4044	1.4	0.17	6.1	9.8	10	317	7.9	25	0.53	68	235	7.6	0.04	3.9	983	152	11
	min	2.3	0.02	<mdl	0.48	0.31	0.35	80	0.10	0.35	<mdl	10	50	1.3	<mdl	<mdl	2.8	0.84	0.002
RG51 n=12	mean	1870	1.0	0.10	4.2	5.5	6.5	249	4.3	4.8	0.86	45	124	5.9	0.02	1.1	146	32	1.9
	SD	2481	1.4	0.08	3.2	5.4	4.4	103	7.0	5.9	1.4	33	106	3.4	0.04	1.9	216	46	2.8
	max	6743	4.3	0.32	9.2	16	12	340	23	18	4.4	129	354	14	0.14	5.4	612	139	7.5
	min	1.3	0.01	<mdl	0.57	0.87	0.6	59	0.03	0.29	<mdl	8.0	38	0.92	<mdl	<mdl	0.19	0.02	<mdl
RG55 n=10	mean	2501	2.7	8.4	837	24	5.7	501	5.2	4.7	1.2	123	244	1.3	41	0.44	150	389	0.54
	SD	2237	1.8	6.5	709	22	2.5	53	4.3	3.3	1.2	79	128	1.2	48	0.31	99	303	0.64
	max	8445	6.6	22	2473	86	8.8	593	14	12	4.4	212	476	4.0	148	1.1	292	803	2.1
	min	914	0.57	2.1	237	9.3	1.1	419	0.54	1.1	0.22	32	64	0.36	2.1	0.09	26	27	0.01

**Table 8
continued.**

Sample Name		Fe	Co	Ni	Cu	Zn	As	Se	Ag	Sn	Sb	Te	W	Re	Au	Tl	Pb	Bi	U
RG56 n=14	mean	7709	7.4	16	227	23	7.3	311	22	13	0.53	118	181	0.90	56	1.2	301	363	1.6
	SD	7553	5.3	11	160	17	6.3	45	40	18	0.31	46	109	1.0	112	0.98	165	252	2.8
	max	22375	20	37	524	62	24	409	125	69	1.2	184	410	3.3	435	2.5	577	831	8.8
	min	147	0.15	0.50	15	1.2	0.36	268	0.17	0.16	0.01	48	41	0.04	0.62	0.02	7.5	12	0.01
RG60 n=12	mean	1390	14	20	267	28	5.2	400	96	2.8	0.44	107	123	1.8	37	0.23	230	322	0.25
	SD	2863	23	34	209	35	2.9	54	88	3.4	0.34	44	49	2.1	37	0.26	176	180	0.31
	max	10401	83	125	760	125	12	469	326	13	1.4	182	207	5.9	122	1.0	610	655	0.93
	min	57	1.4	2.0	34	2.3	2.6	317	16	0.14	0.16	50	65	0.15	1.6	0.03	54	99	0.00
RG62 n=15	mean	3167	2.8	5.6	123	59	4.7	429	2.2	0.75	0.20	169	133	0.79	9.4	0.61	57	265	0.13
	SD	4376	2.9	6.7	195	74	4.2	60	2.1	0.53	0.13	129	70	0.78	8.3	0.54	60	244	0.18
	max	13456	11	25	706	270	18	540	5.5	1.9	0.39	543	269	2.0	26	1.6	234	999	0.52
	min	40	0.51	0.43	15	0.18	0.28	342	0.14	0.07	0.02	43	50	0.05	0.55	0.02	1.3	12	<mdl
RG64 n=19	mean	9345	14	12	365	29	12	497	64	3.4	2.8	193	255	36	85	4.9	413	572	2.7
	SD	9718	14	11	682	29	8.5	70	101	5.2	3.2	95	175	71	138	5.4	392	402	8.7
	max	33273	50	46	3010	85	31	687	386	22	11.4	434	602	218	517	18	1491	1356	39
	min	1201	1.8	2.3	16	4.3	2.8	385	0.71	0.23	0.10	48	67	0.25	0.58	0.43	9.0	15	0.01
RG65 n=10	mean	2864	3.6	3.9	157	35	5.1	344	63	14	1.5	141	96	1.7	44	0.57	84	569	2.0
	SD	2971	5.6	2.9	229	39	3.4	29	144	19	3.0	137	24	1.4	84	0.56	82	674	2.1
	max	9457	19	10	767	132	13	387	464	56	9.9	457	144	4.1	273	1.5	244	2105	5.1
	min	28	0.04	0.47	3.0	2.4	1.8	310	0.05	0.34	<mdl	27	60	0.26	0.01	0.01	2.2	2.8	0.01

APPENDIX

APPENDIX FIGURE CAPTIONS

FIGURE A1. (a) Map view of the structural controls on the Central Diorite orebody showing the main shear zones and faults confining the ore body. (b) Map view of the major shear zones within the deposit and the location of the interlayered dykes that intruded the orebody.

FIGURE A2. (a) Map view showing the Wourhaming granite situated with respect to the shear zones and intrusive dykes. The location of drillcore WRD 09775002 is shown through the granite pluton. Inset is a table of granite samples collected and relative depths. (b) Oblique view showing the Wourhaming granite intercepting the intrusive dykes and major shear zones. The direction of drillcore WRD 09775002 is shown in relation to the granite.

FIGURE A3. (a) NW-SE cross-section showing lithologies in the Central Diorite orebody with the outline of the high-grade Southern Diorite Deep core. Sampled drillcores and also shown. (b) NW-SE cross-section showing the same area as in (a) but with Au concentrations plotted along the drillcores. The sampling intervals are shown in the three diorite drillcores.

FIGURE A4. (a) Plan view of the southern section of the South Pit showing the blocks with different grades and samples collected from the high grade zones. Inset the location of the South Pit with respect to the surrounding volcanics and Central Diorite. (b) Photograph of diorite sample with zeolite facies alteration and native copper dissemination and staining. (c) Photograph of South Pit wall to the east showing the trajectory of the South-Eastern shear. (d) Photograph of the pit floor after blast with ore grades marked out and chip-rock sample collection.

FIGURE A5. Schematic lithological columns and assay data for Cu, Mo, Au and Bi in the four drillcores sampled in this project. The sampling intervals are also marked.

FIGURE A6. (a) Lithological and mineralisation details for the sampled interval in the drillcore that intersects the granite (WRD 09775002). The individual sample locations are also marked. (b) Photograph illustrating a mineralised contact between sheared diorite and granite. (c) Photograph showing fluorite veinlet in coarse grained granite. (d) Typical coarse molybdenite patches in coarse-grained granite (e) and (f) Polished blocks showing molybdenite in both coarse and fine-grained granite.

FIGURE A7. (a) Lithological and mineralisation details for the sampled interval in diorite from drillcore WBD 1063001. The individual sample locations are also marked. (b) Photograph of diorite showing the appearance of cross-cutting veinlets with mineralisation. (c) Photograph of diorite showing quartz veining with molybdenite occurring on the margin.

(d) Photograph showing the typical appearance of sheared diorite. (e) Polished block showing sulphides in a biotite rich zone.

FIGURE A8. (a) Lithological and mineralisation details for the sampled interval in diorite from drillcore WBD 10590002. The individual sample locations are also marked. (b-e) Polished blocks showing occurrence of molybdenite and other sulphides

FIGURE A9. (a) Lithological and mineralisation details for the sampled interval in diorite from drillcore WRD 10600004. The individual sample locations are also marked. (b) Photograph of quartz±clinozoisite veinlets in diorite that have undergone deformation. (c) Photograph of diorite showing fine-grained shear zones with biotite. (d) Photograph of diorite showing porphyroblastic albite. (e) Polished block showing large, pegmatitic albite and associated molybdenite. (f) Photograph of large vein in diorite comprising milky quartz±clinozoisite.

FIGURE A10. BSE images illustrating lithologies and alteration assemblages. (a) Typical Qz-Plag-Bt association in coarser diorite (b) Mica-rich bands characterising foliation in the fine-grained diorite. (c) Coarse-grained granite showing typical perthitic feldspar and the presence of Clz along the edges of molybdenite (d, e) Typical break-down of coarse pyroxene resulting in Hbn-Ti-minerals and epidote replacement in dolerite. (f) Enrichment in apatite and scheelite grains in diorite. Inclusions of REE-minerals in granite (g) and Ilmenite surrounding a rutile core (h). (i) Detail on the dusty inclusions in ilmenite from (h). (j) Sulphides along a veinlet of actinolite. The complexity of alteration assemblage is shown and also the transition to fine-grained diorite with little mineralisation. The veinlet selvage comprises epidote (replacing actinolite?) and biotite. (k-l) Clinozoisite embedding sulphides in the granite. (m) Oscillatory zonation in clinozoisite. (n) Biotite-Clz alteration in granite; note the dusty REE-mineral inclusions accompanying break-down of Clz/allanite. (o) Fe-rich chlorite (chamosite) interlayered with muscovite in granite.

FIGURE A11. BSE images showing the occurrence of Ca-rich stilbite (a-c) and aspects of accompanying minerals in the zeolite facies alteration. Stilbite intergrown with molybdenite (a), and replacing feldspar in diorite (b). Detail from (b) showing typical acicular aggregates of stilbite (c). Halo of quartz+clay minerals replacing plagioclase porphyroblast in diorite. (e) Late hydrothermal biotite interlayered with chlorite (f) and overgrown by Clz (f). (g, h) Breakdown of allanite resulting in fields of dusty inclusions with REE-minerals and enrichment in Th. (i) Large grain of thorite nucleating in areas as in (h).

FIGURE A12. BSE images of sulphide assemblages in diorite host rock. (a) Typical two-phase pyrrhotite with lamellar exsolutions. Note the pointed edges of the lamellae. (b)

Skeletal exsolutions of Po in Cub. (c) Argentopentlandite as inclusions in Pn. (d) Fields of small exsolutions of Sph-Stn in cubanite. (e) Coarser-Sph-Stn inclusions in Cub (f) Stn segregated at the boundary between Sph and Cp. (g) Co-bearing Mck in Cp. (h-j) Unusual thiospinel occurrence (embedded within bastnasite) occurring at the boundaries between pyrite and chalcopyrite. (k) Minor bornite and covellite replacing chalcopyrite with cubanite exsolutions. Chalcocite (l) and native Cu (m) in the diorite altered to zeolite facies.

FIGURE A13. LA-ICPMS element map of a coarse molybdenite lamella in diorite from the Open Pit (sample RG10) showing a tight microfold on one side and silicate replacement on the other side. This grain shows high- Re concentration with slight depletion along replacement boundaries. Tungsten shows strong concentration relative to replacement boundaries. The chalcophile elements (Bi, Pb, Te) show a strong correlation with one another and correlate with spots of high-Au concentration.

FIGURE A14. LA-ICPMS element map of coarse-grained, highly-deformed molybdenite from diorite in ABreccia (North Pit, sample NK25). Rhenium is highly concentrated within molybdenite lamellae and depleted along the boundaries. Tungsten shows an inverse trend. Small, spot-concentration of Au and Ag are present and show correlation with Pb and Bi distribution.

FIGURE A15. Secondary electron and ion beam images showing the experimental procedure during FIB-TEM sample preparation (as marked). The duplication in (a, b) and (d, e) is meant to show details of the tellurides that have been sliced, e.g. pilsenite in 62RG in (a), tsumoite in 45RG in (b, e) and the Bi-Pb-tellurides that have been analysed by EPMA on sample 45RG in (e); the latter slice was lost during welding on the Cu grid.

FIGURE A16. Secondary electron images showing location and details of the five FIB-TEM prepared foils from molybdenite in granite and diorite. These targeted specific-site extraction of material for TEM study necessary for crystal-structure and nanoscale characterisation of Bi-Pb-tellurides and host molybdenite.

APPENDIX TABLES LIST

Table A1. Microprobe analyses of feldspar group minerals

Table A2. Microprobe analyses of biotite group minerals

Table A3. Microprobe analyses of muscovite group minerals

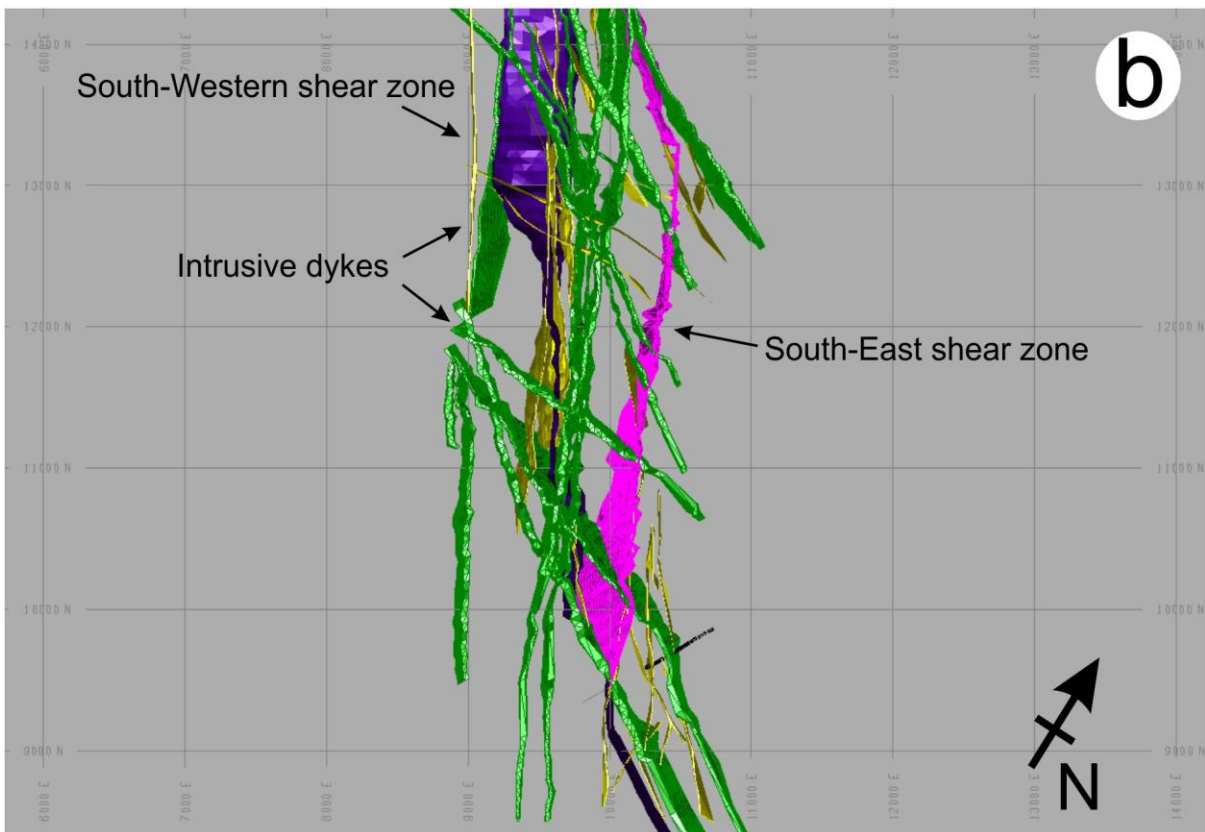
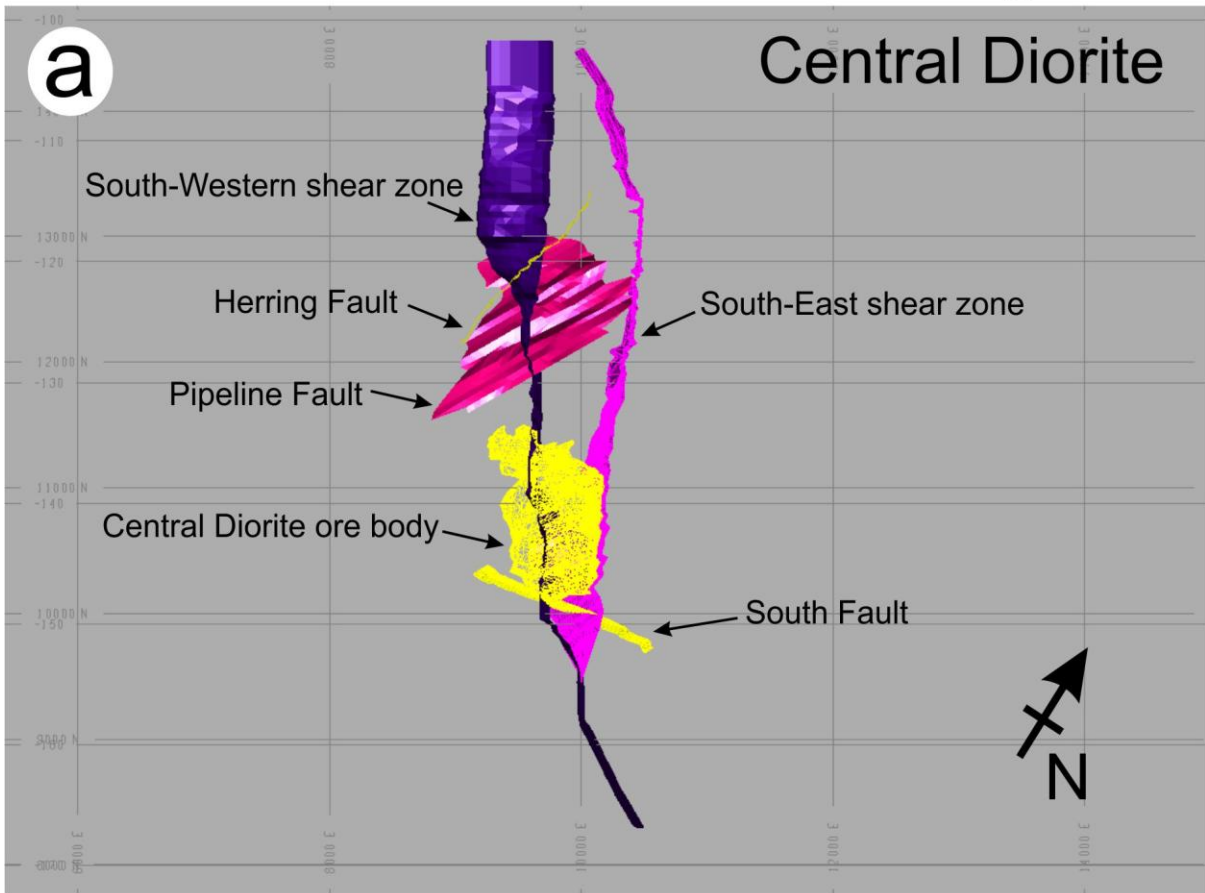
Table A4. Microprobe analyses of epidote group minerals

Table A5. Microprobe analyses of stilbite

Table A6. Electron probe microanalyses of pyrite, pentlandite, argentopentlandite, cubanite, mackinawite and Fe-Ni-thiospinel

Table A7. LA-ICPMS data of molybdenite

Figure A1



WRD 09775002-Granite

Figure A2

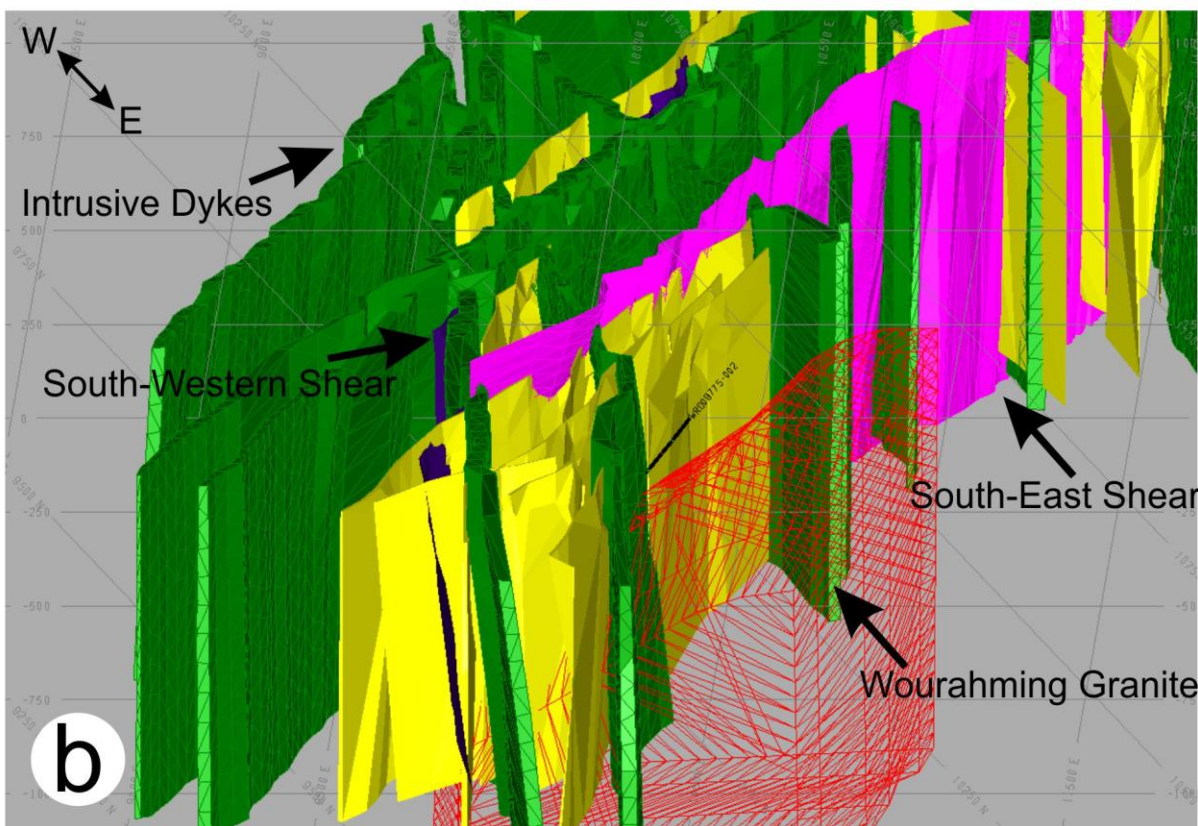
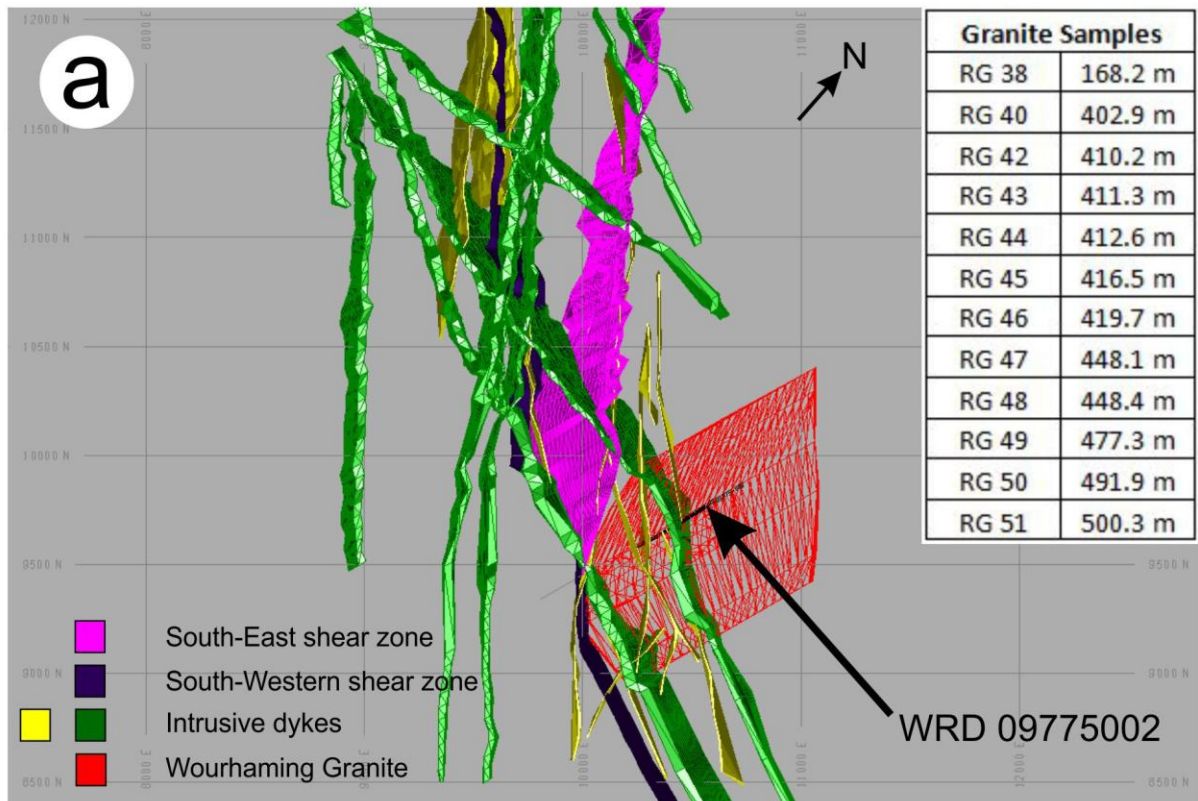


Figure A3

Central Diorite Drill Cores

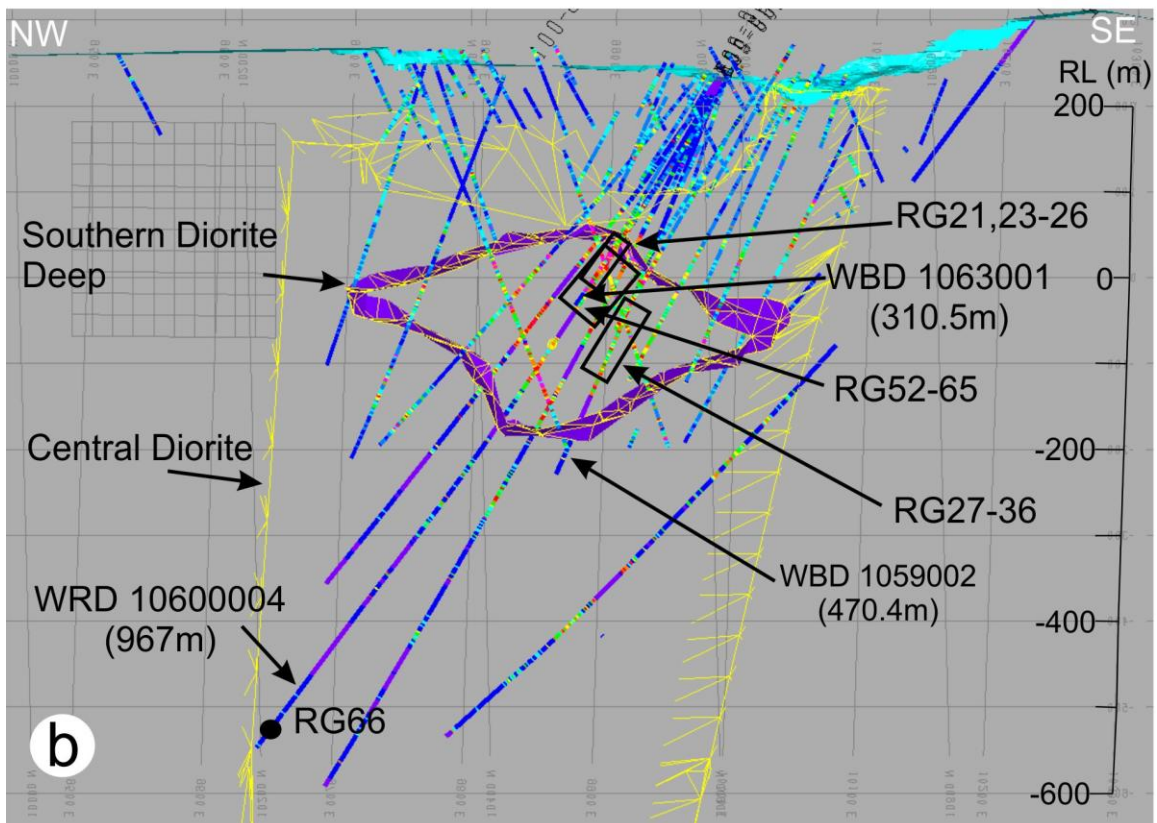
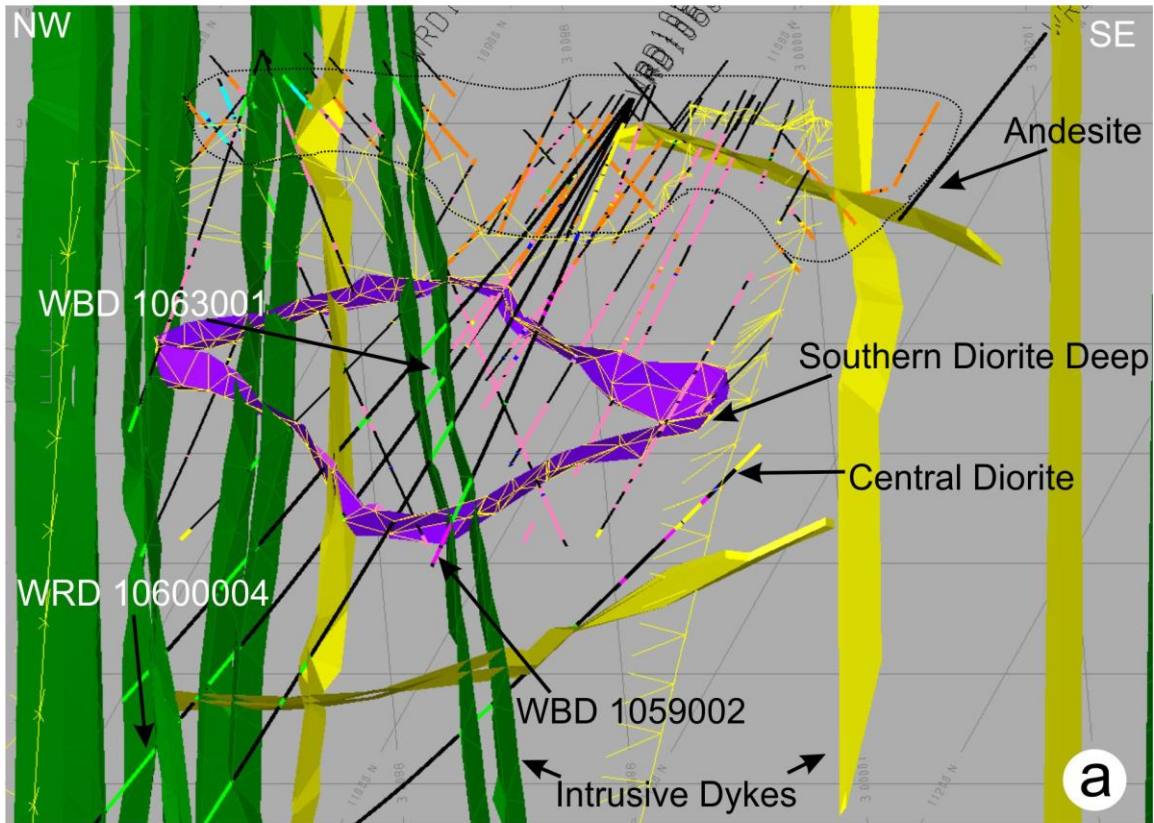


Figure A4

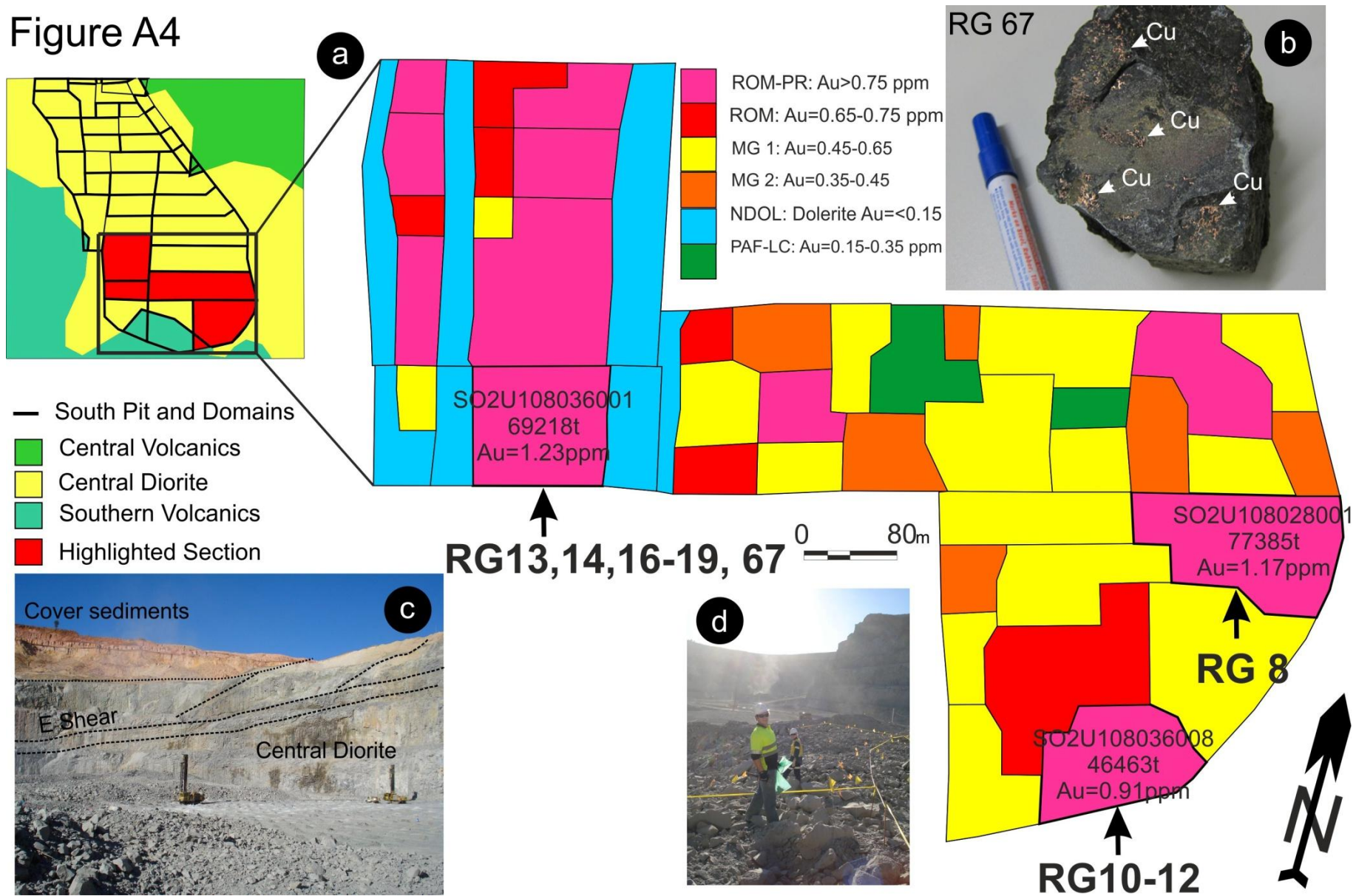
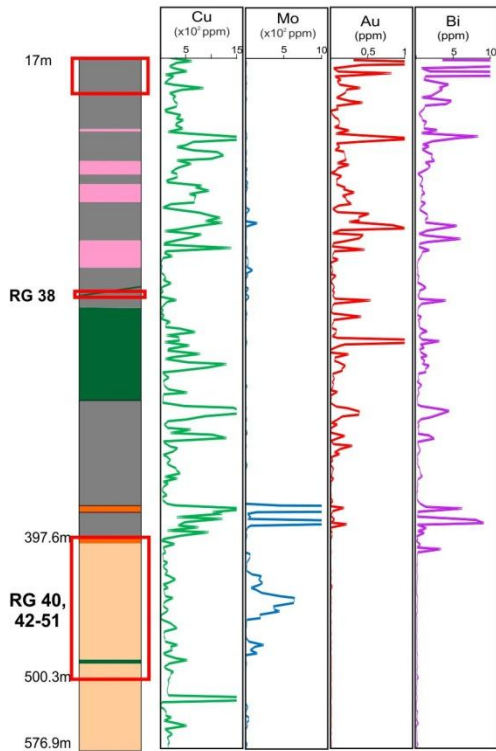
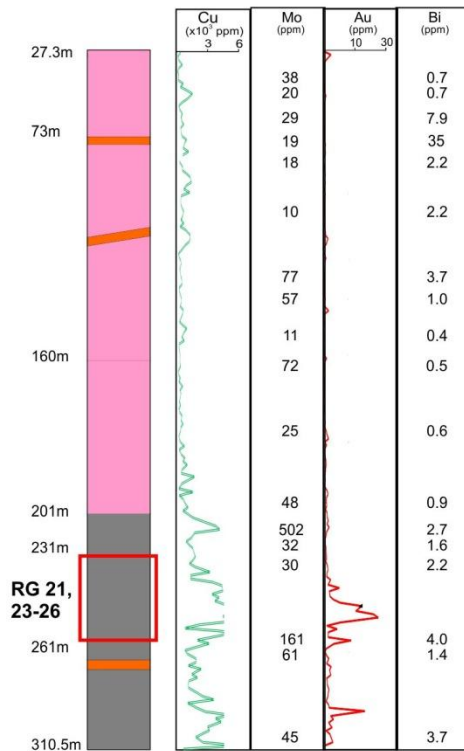


Figure A5

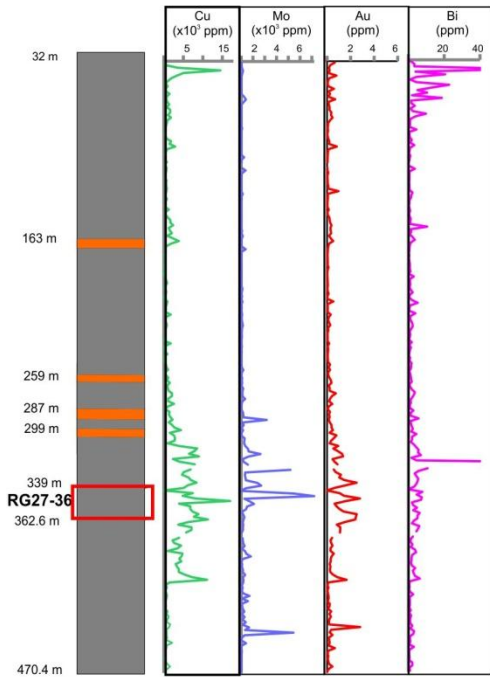
WRD 09775002



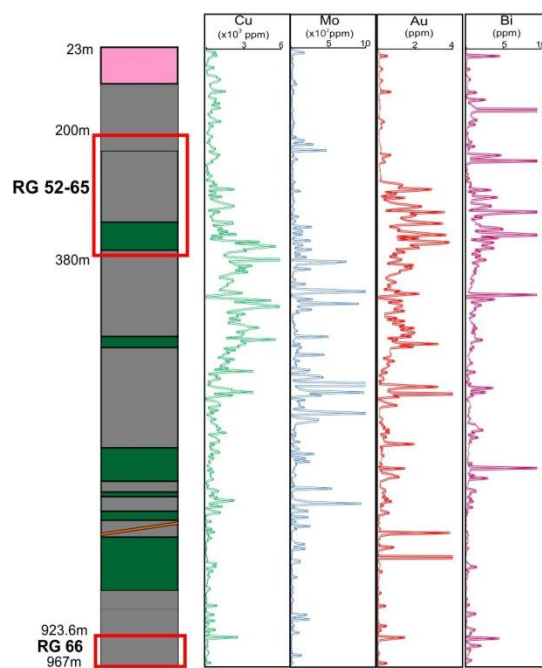
WBD 10630001



WBD 105900002



WRD 10600004



WRD 09775002

Figure A6

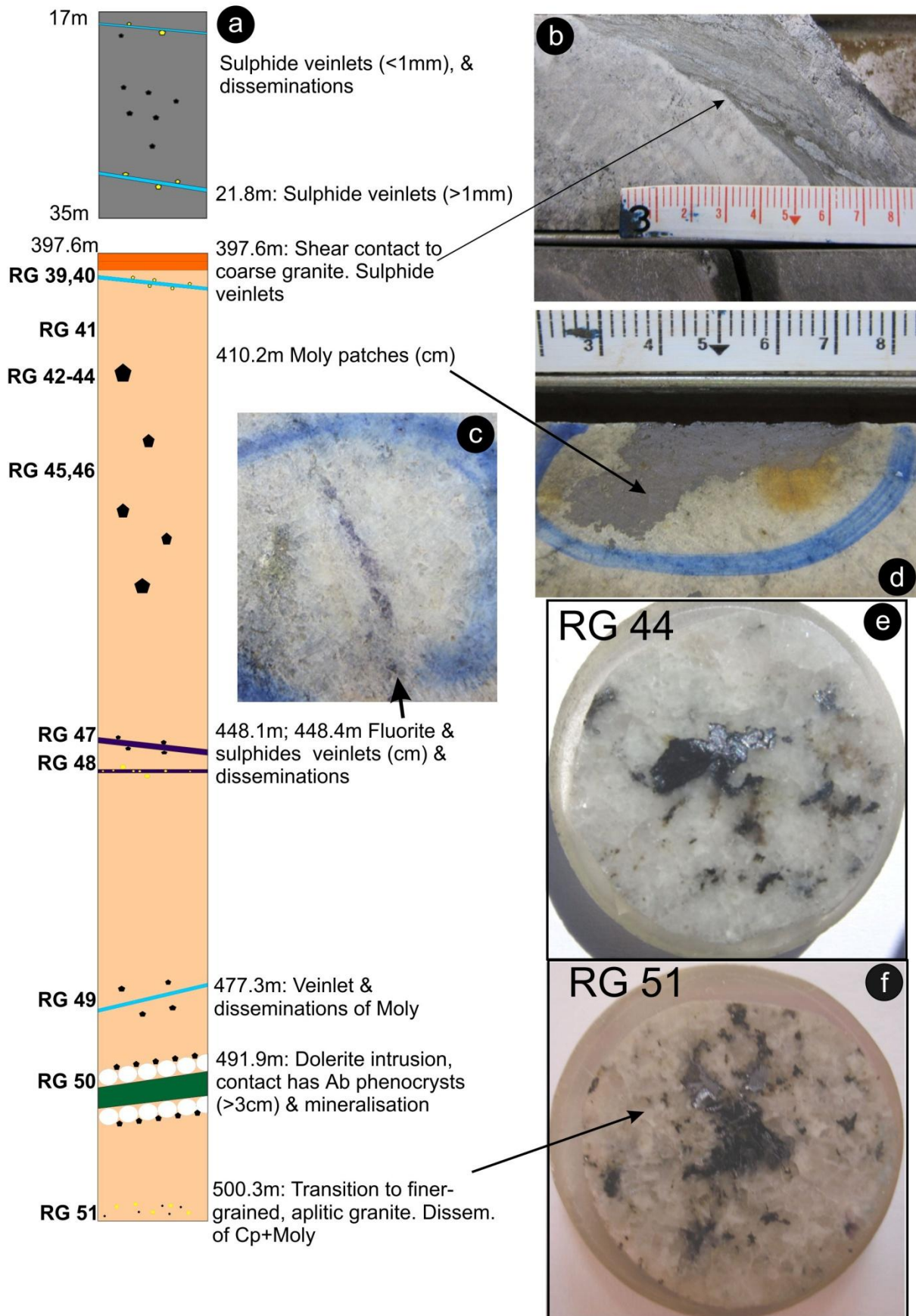


Figure A7

WBD 1063001

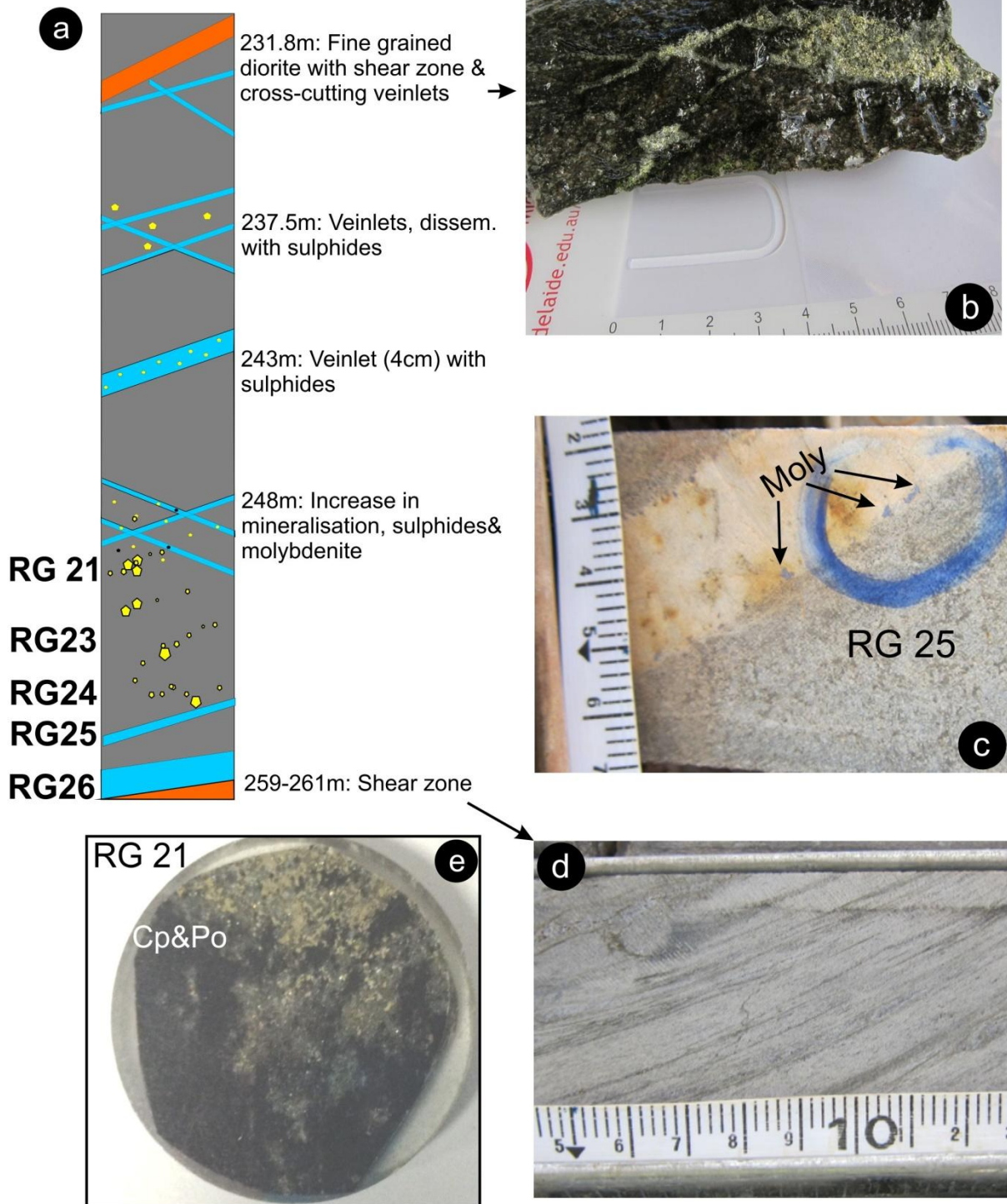
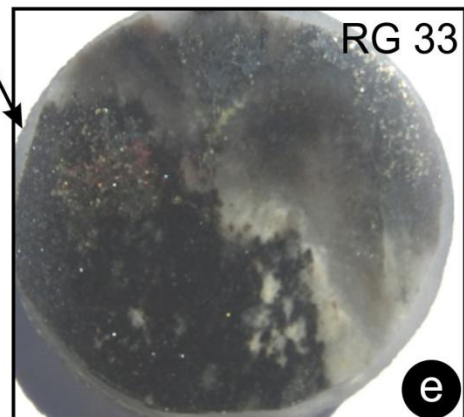
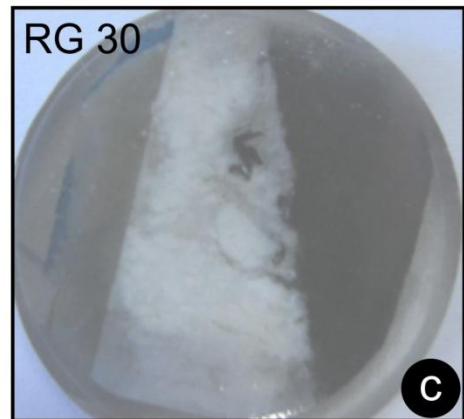
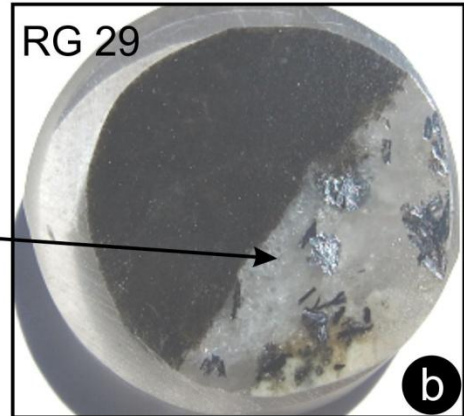
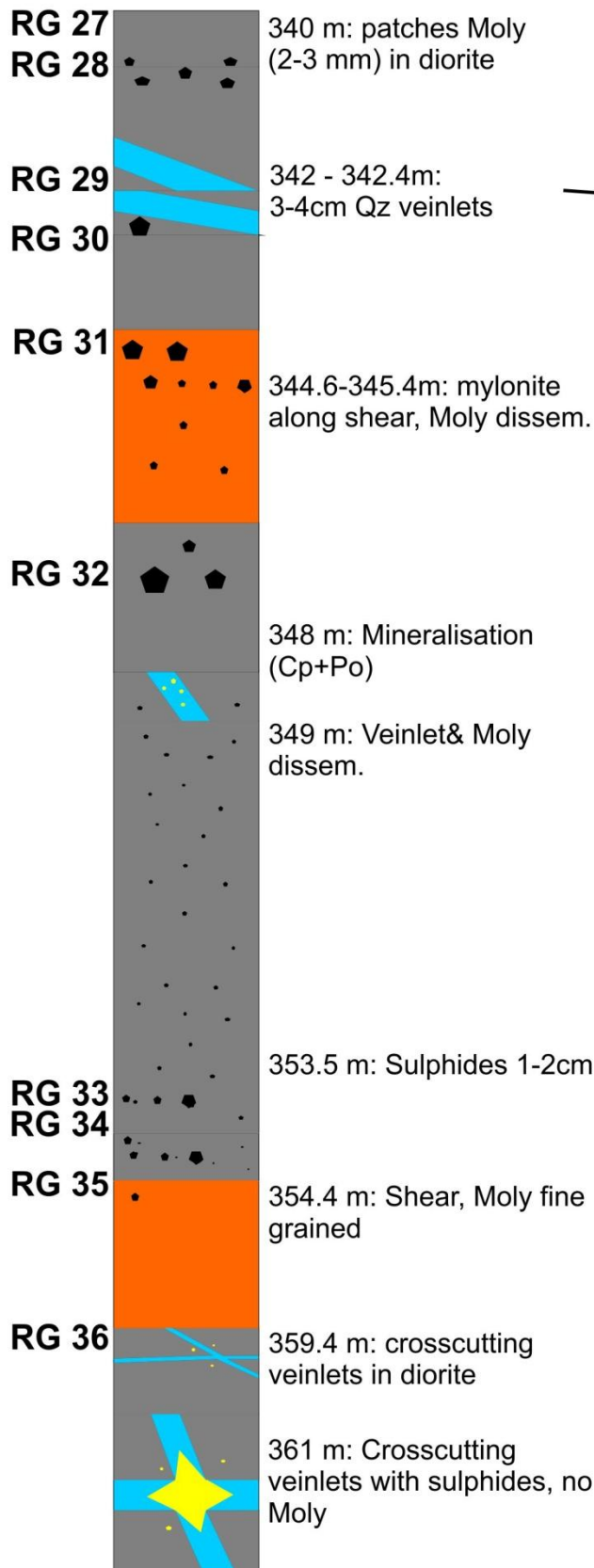


Figure A8

a WBD 10590002



a WRD10600004

Figure A9

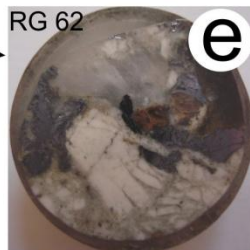
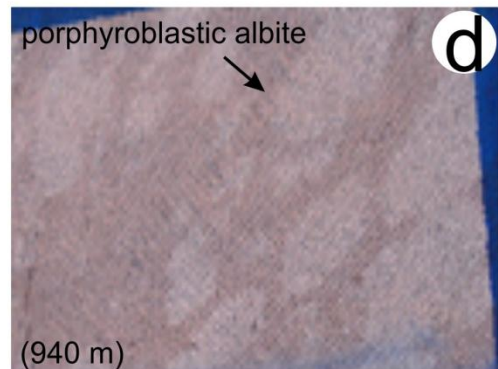
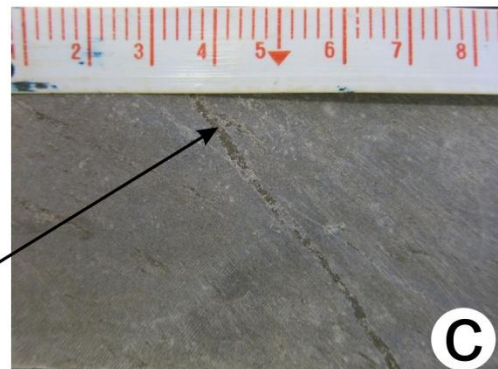
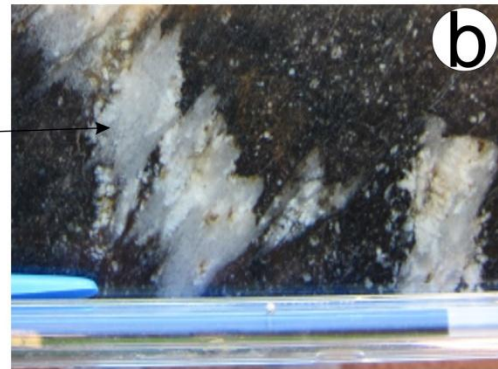
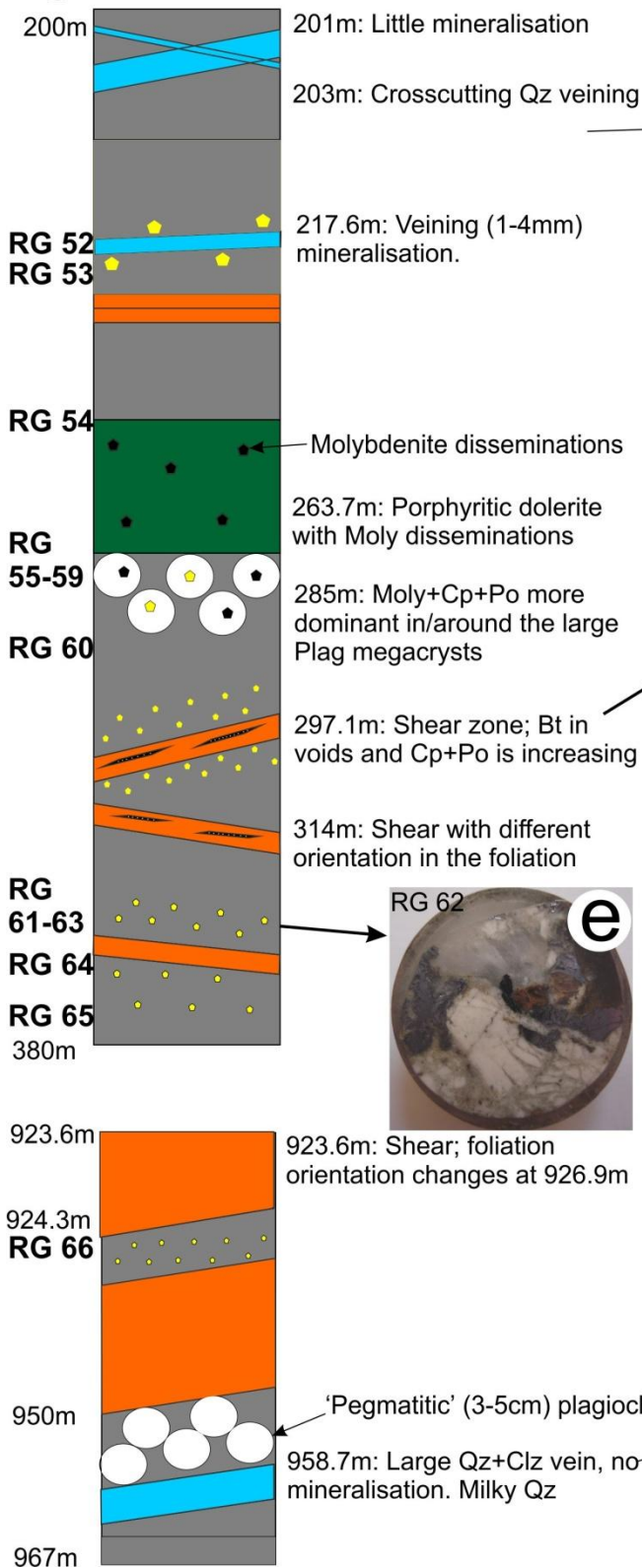


Figure A10

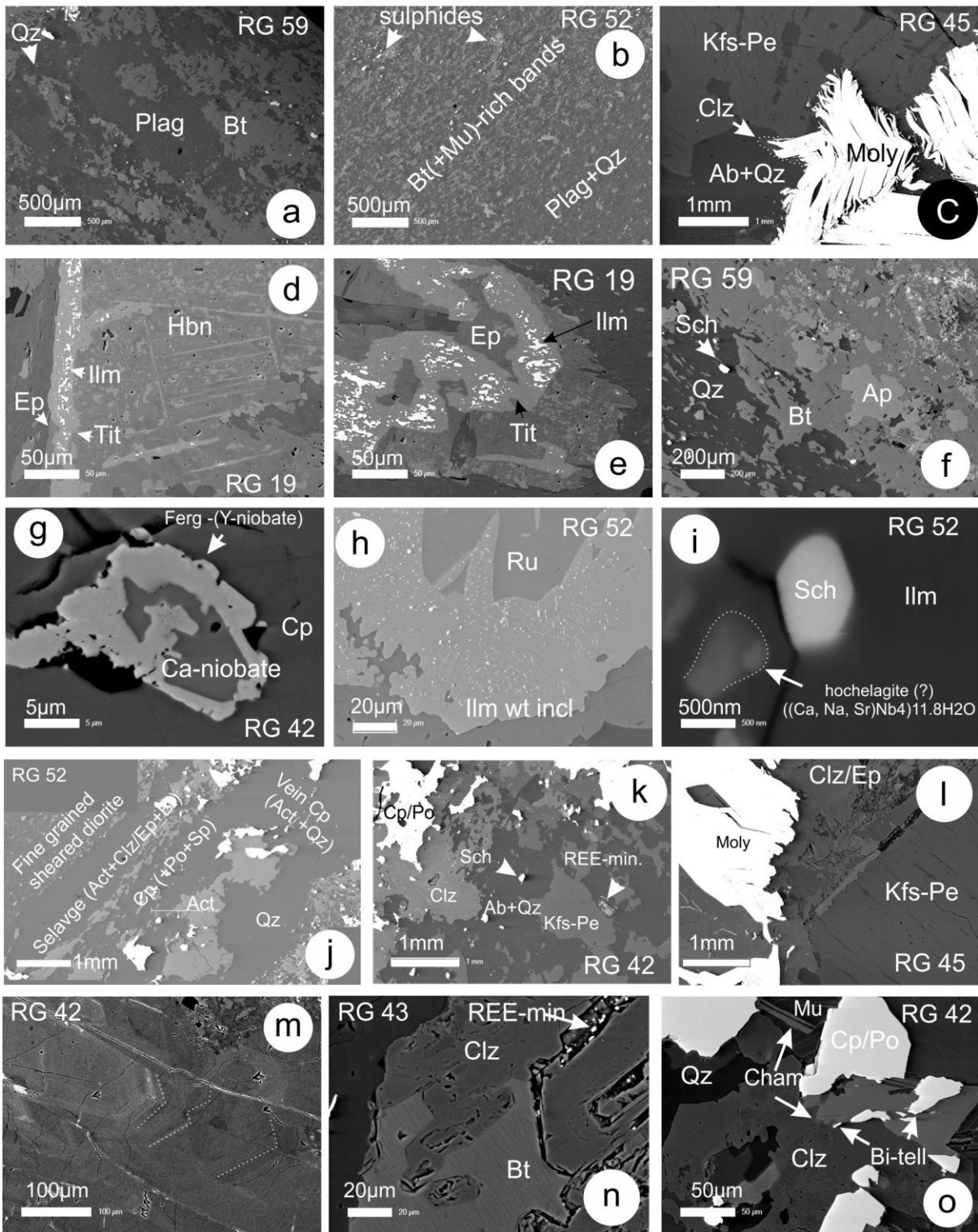


Figure A11

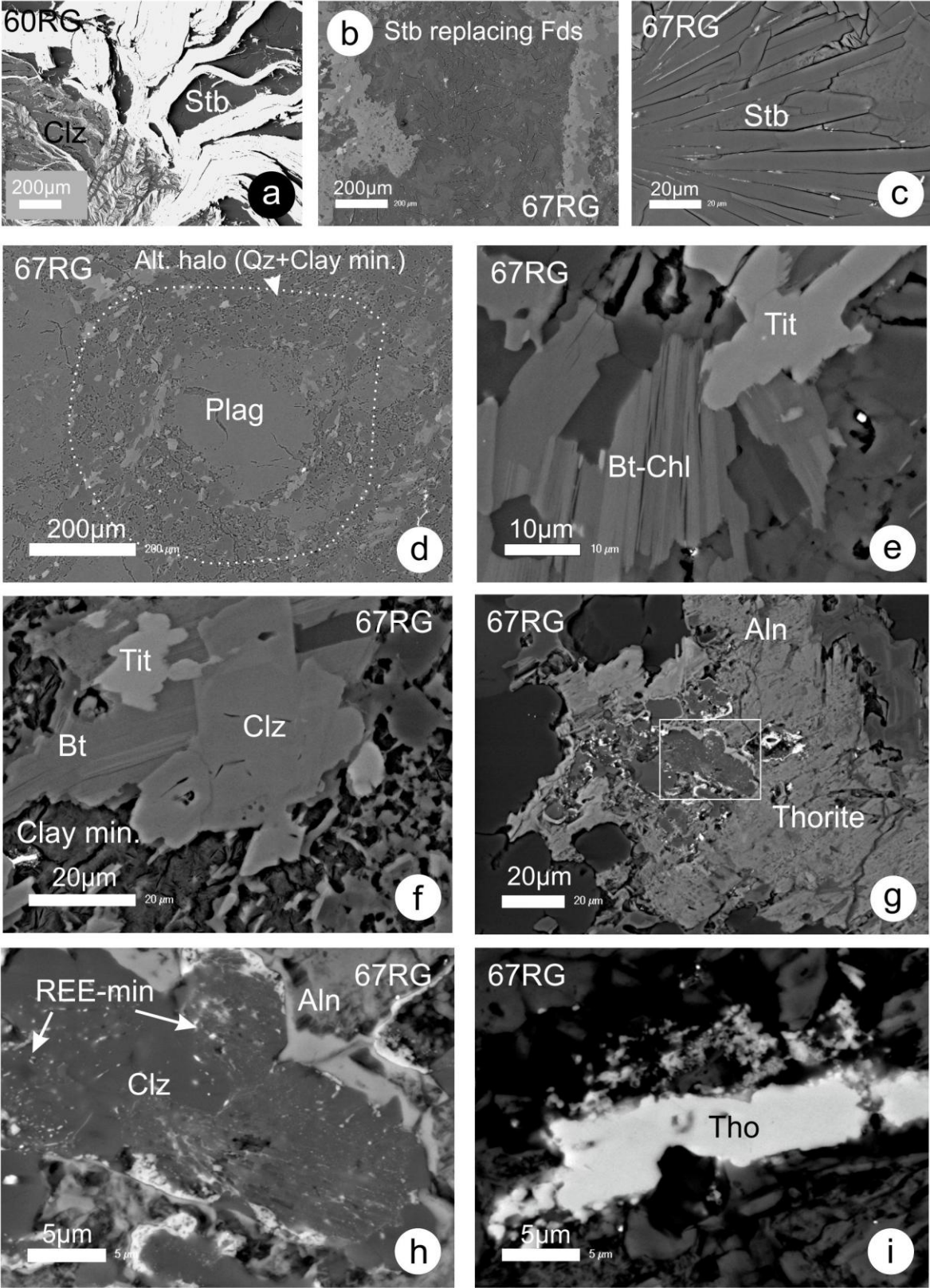
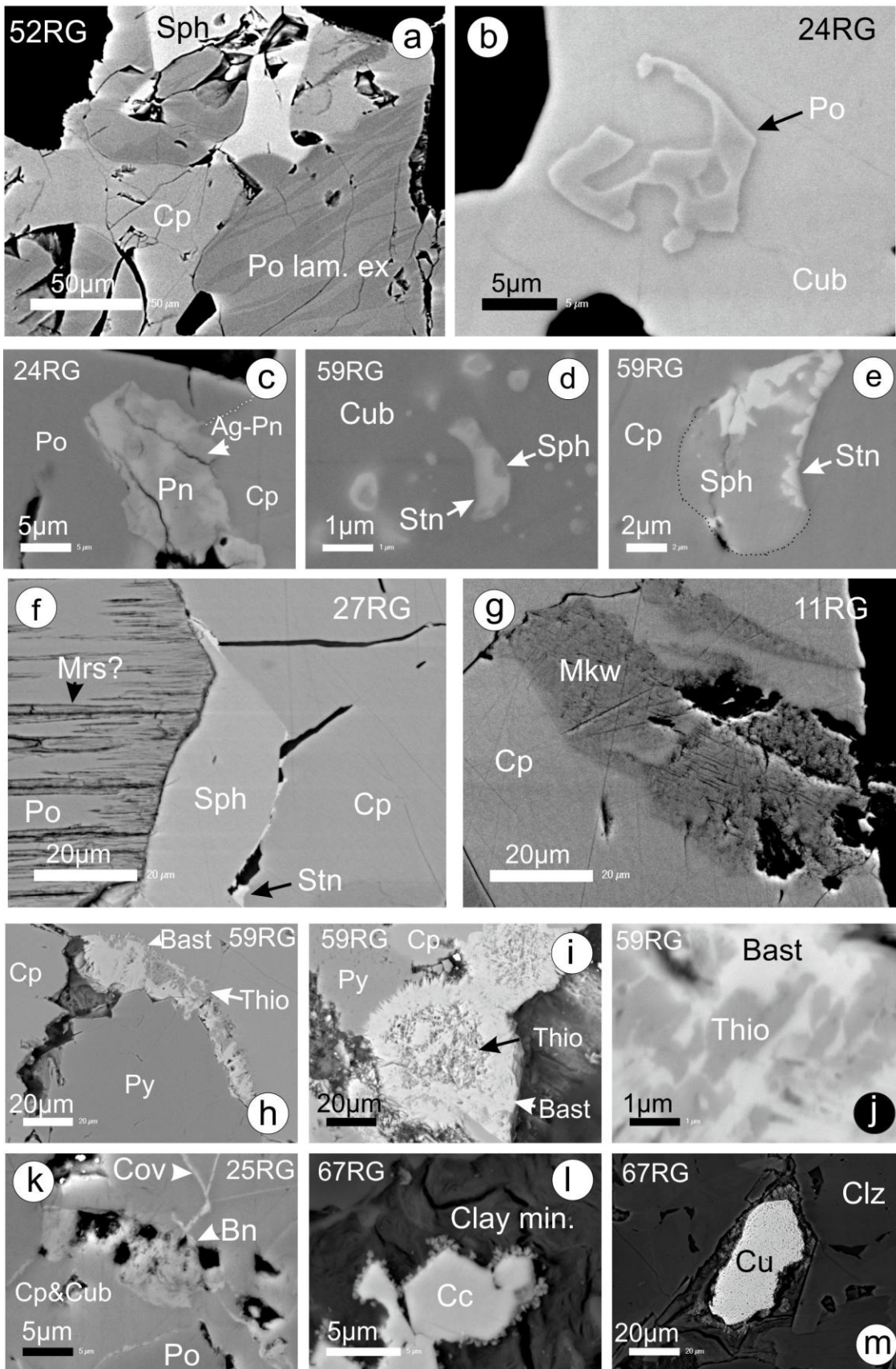
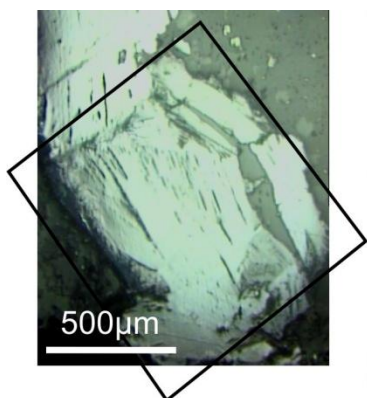


Figure A12





RG 10

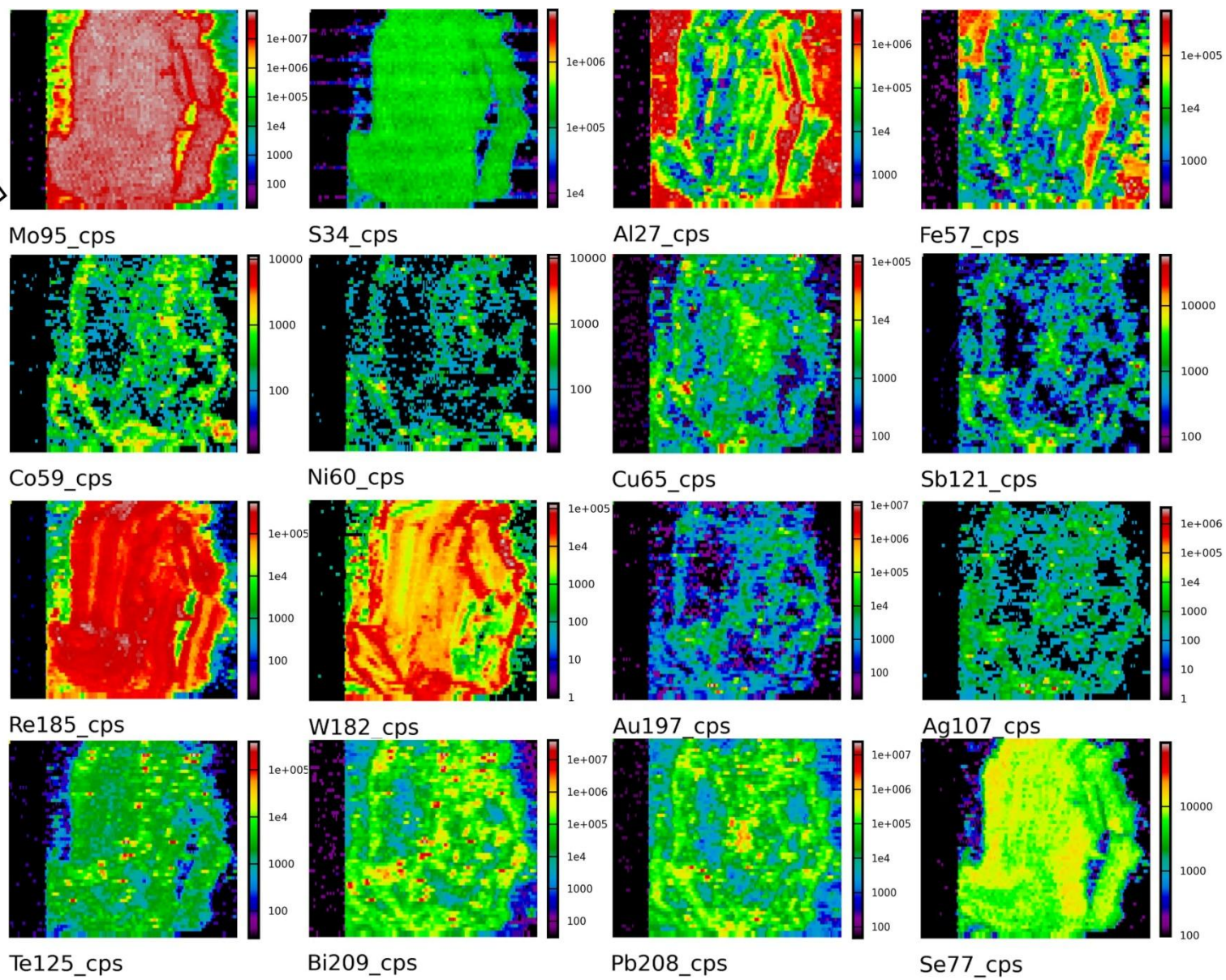


Figure A13

NK 25

Figure A14

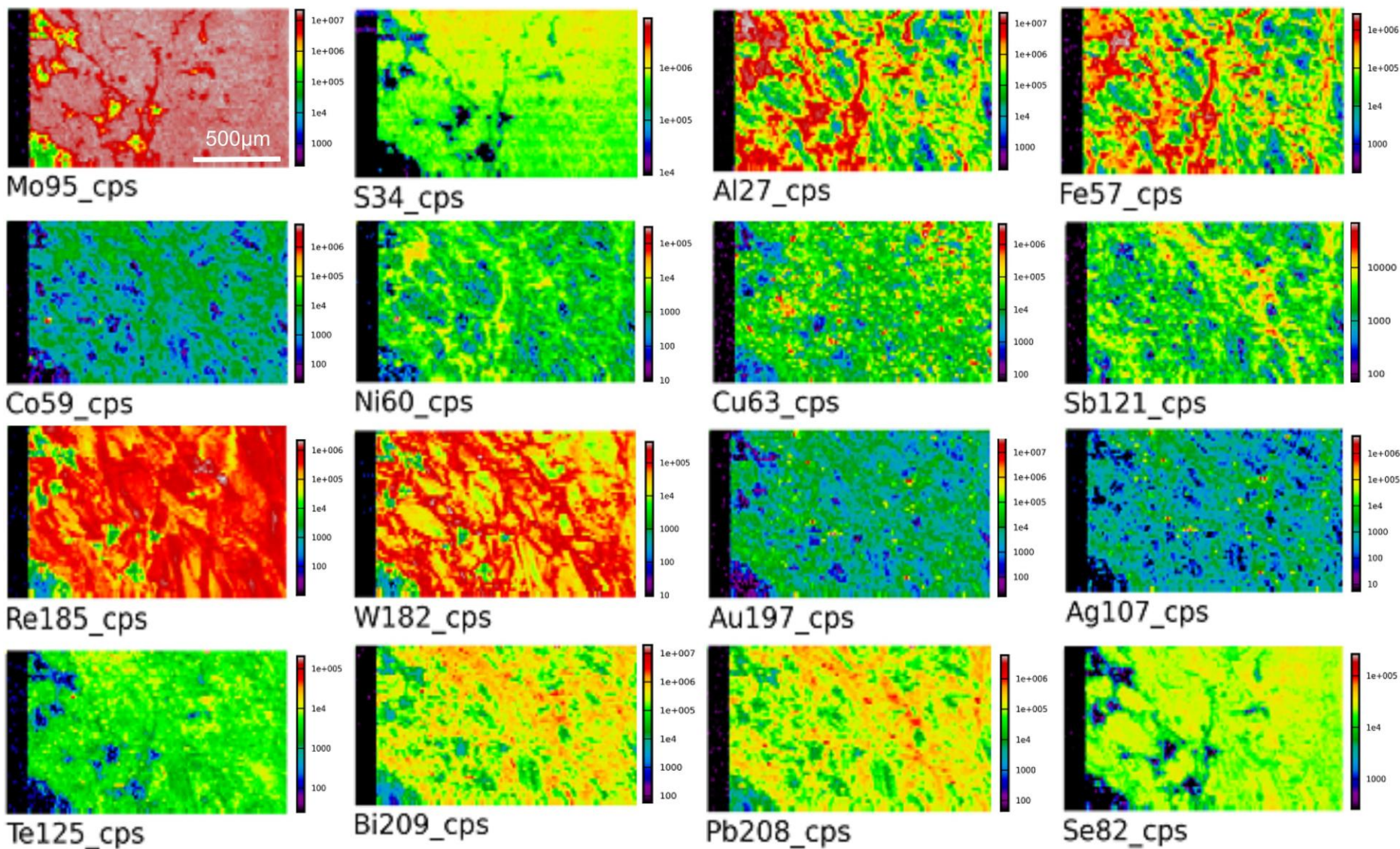


Figure A15

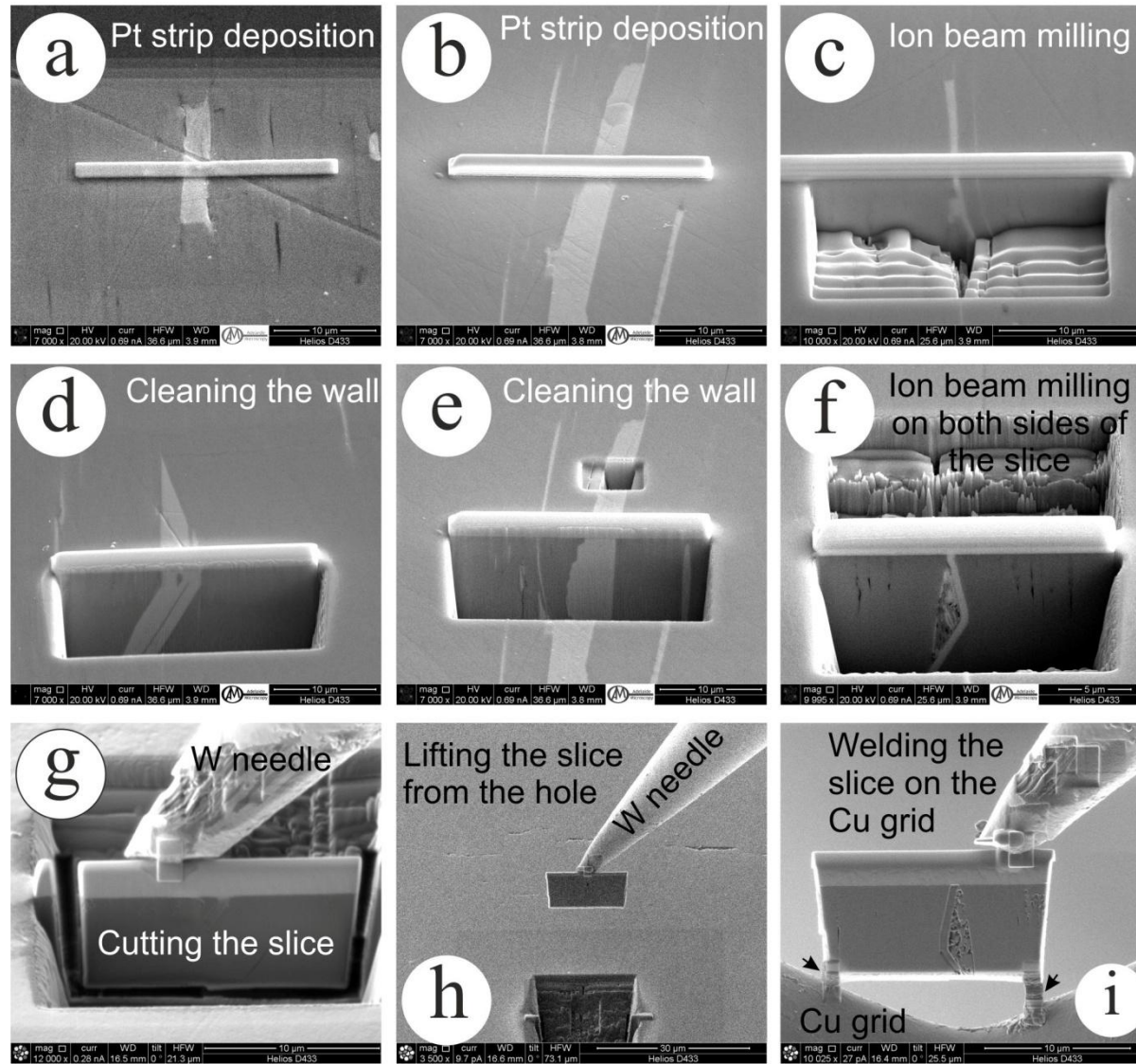


Figure A16

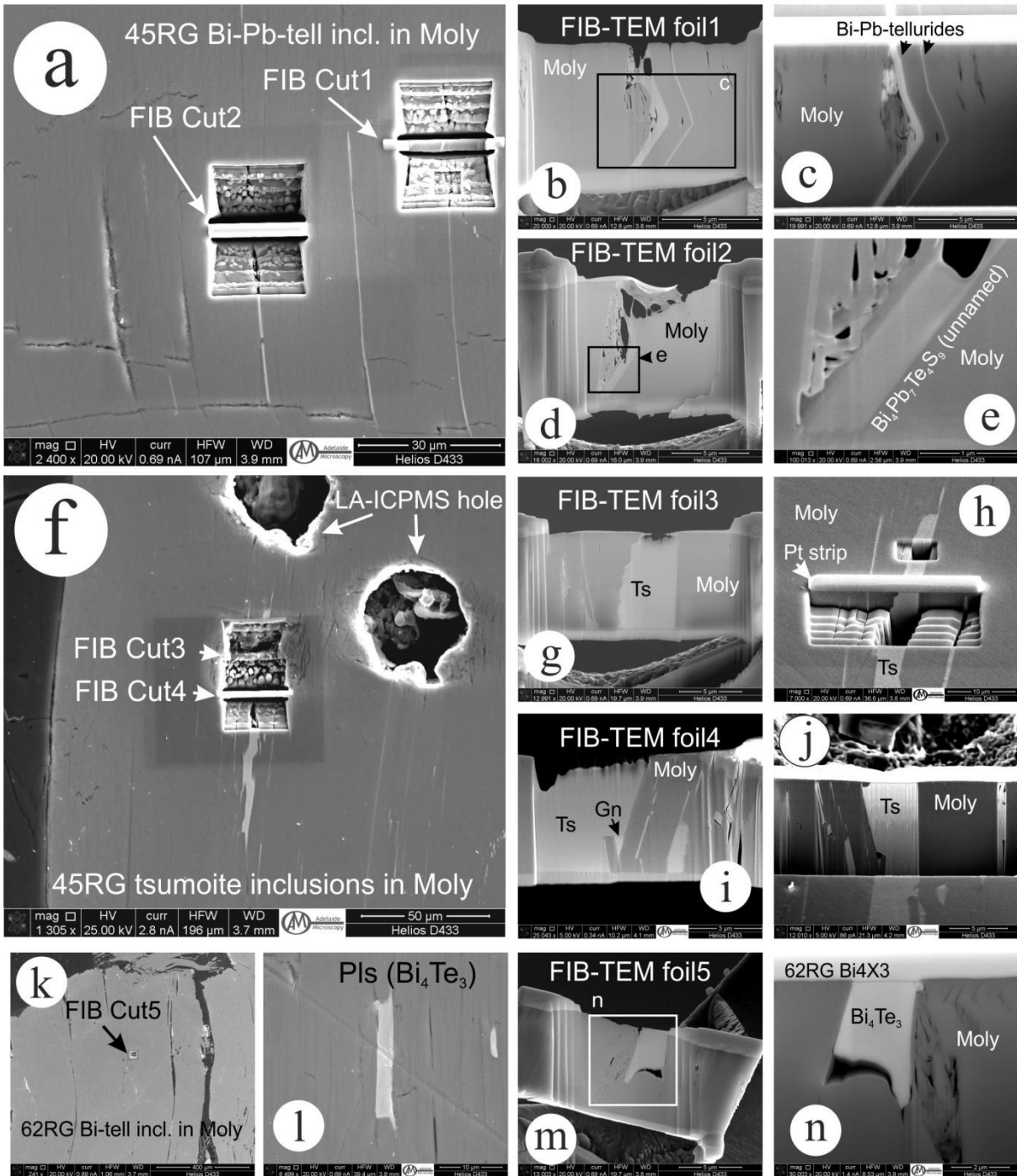


Table A1. Microprobe analyses of feldspar group minerals

	RG42				RG43				RG45				RG47				RG49				RG50			
	albite		K-feldspar		albite	K-feldspar		plagioclase		K-feldspar		albite		K-feldspar		albite		K-feldspar		albite		K-feldspar		
	mean	SD	mean	SD		mean	SD	mean	SD	mean	SD	mean	SD	mean	SD	mean	SD	mean	SD	mean	SD	mean	SD	
(Wt.%)	n=2		n=3		n=4		n=5		n=6		n=8		n=15		n=7		n=7		n=10		n=2			
CaO	0.04	0.01	<mdl		0.66	<mdl	0.46	0.29	<mdl		0.69	0.44	<mdl		0.54	0.28	<mdl		3.45	1.91	0.16	0.04		
Na ₂ O	10.68	1.54	0.34	0.07	11.22	0.28	0.03	9.66	3.04	0.31	0.08	11.35	0.22	0.35	0.07	11.48	0.20	0.27	0.66	9.64	1.25	1.35	0.36	
K ₂ O	0.10	0.01	16.39	0.27	0.05	16.41	0.08	0.95	1.91	16.19	0.14	0.09	0.03	16.25	0.21	0.07	0.02	16.35	0.85	0.39	0.58	13.81	1.86	
FeO	0.04	0.01	0.06	0.02	0.15	0.05	0.05	0.29	0.49	<mdl		<mdl		0.04	0.04	<mdl		<mdl		0.27	0.17	0.33	0.45	
TiO ₂	<mdl		<mdl		<mdl	0.04	0.03	<mdl		<mdl		<mdl		<mdl		<mdl		<mdl		<mdl		0.03	0.04	
MgO	<mdl		<mdl		<mdl	<mdl		0.05	0.09	<mdl		<mdl		<mdl		<mdl		<mdl		<mdl		<mdl		
SiO ₂	71.26	3.67	64.06	0.52	68.38	63.95	0.30	67.12	3.52	64.07	0.33	67.77	0.34	64.07	0.60	67.35	0.78	64.49	0.54	64.11	2.46	60.91	4.52	
MnO	<mdl		<mdl		0.03	<mdl		<mdl		<mdl		<mdl		<mdl		<mdl		<mdl		<mdl		<mdl		
Al ₂ O ₃	18.08	2.01	18.23	0.24	20.56	18.31	0.17	20.08	0.54	18.23	0.29	20.32	0.70	17.94	0.35	20.28	0.50	18.36	0.28	22.32	1.49	21.95	4.44	
Cl	<mdl		0.02	0.03	<mdl	<mdl		0.04	0.06	0.02	0.01	<mdl		0.03	0.10	<mdl		<mdl		0.02	0.05	<mdl		
Total	100.2		99.1		101.0	99.0		98.6		98.8		100.2		98.6		99.7		99.5		100.2		98.5		
Formula calculated to 8 O a.p.f.u.																								
Ca	0.002	-	-	0.001	0.031	-	0.000	0.022	0.014	-	0.000	0.032	0.020	-	0.002	0.025	0.013	-	0.006	0.163	0.091	0.008	0.0021	
Na	0.895	0.1405	0.031	0.006	0.941	0.026	0.002	0.830	0.260	0.028	0.007	0.960	0.0233	0.032	0.007	0.976	0.016	0.024	0.060	0.825	0.099	0.122	0.0333	
K	0.006	-	0.977	0.013	0.003	0.979	0.004	0.054	0.105	0.966	0.010	0.005	0.0017	0.972	0.014	0.004	0.001	0.969	0.048	0.022	0.033	0.823	0.1034	
Total	0.903	0.140	1.008	0.008	0.975	1.004	0.004	0.905	0.167	0.995	0.009	0.998	0.0121	1.004	0.015	1.006	0.012	0.993	0.020	1.010	0.014	0.953	0.068	
Al	0.921	0.1143	1.004	0.008	1.049	1.009	0.010	1.049	0.022	1.005	0.014	1.045	0.029	0.991	0.015	1.049	0.028	1.006	0.014	1.161	0.084	1.208	0.2555	
Si	3.081	0.120	2.993	0.004	2.959	2.990	0.007	2.974	0.050	2.996	0.010	2.957	0.0269	3.004	0.009	2.955	0.025	2.997	0.009	2.829	0.086	2.845	0.1856	
Mg	-	-	-	-	-	-	-	0.003	0.007	-	-	-	-	-	-	-	-	-	-	-	-	-	-	
Fe	0.002	-	0.002	0.001	0.006	0.002	0.002	0.011	0.019	-	-	-	-	0.001	0.001	-	-	-	-	0.010	0.006	0.013	0.0178	
Mn	-	-	-	-	0.001	-	-	-	-	-	-	-	-	-	-	-	-	-	-	-	-	-	-	
Ti	-	-	-	-	-	0.001	0.001	-	-	-	-	-	-	-	-	-	-	-	-	-	-	0.001	0.0014	
Total	0.003	-	0.005	0.001	0.007	0.004	0.003	0.015	0.026	0.002	0.001	0.003	0.0018	0.003	0.002	0.002	0.001	0.001	0.002	0.012	0.006	0.016	0.0192	
ab %	99.1	0.2	3.1	0.6	96.5	2.5	0.2	91.7	16.1	2.9	0.8	96.3	2.1	3.2	0.7	97.1	1.3	2.4	5.7	81.7	10.4	12.8	4.4	
an %	0.2	0.1	0.0	0.1	3.2	0.0	0.0	2.4	1.5	0.0	0.0	3.2	2.0	0.0	0.2	2.5	1.3	0.0	0.5	16.1	8.9	0.8	0.3	
Kfs %	0.6	0.1	96.9	0.6	0.3	97.5	0.2	6.0	17.0	97.1	0.7	0.5	0.2	96.8	0.6	0.4	0.1	97.6	6.2	2.2	3.3	86.4	4.7	

Detection Limits (wt%) Al 0.01, Ca 0.02, Cr 0.01, Cl 0.02, Fe 0.03, K 0.01, Mn 0.03, Mg 0.02, Na 0.04, P 0.03, Si 0.02, Ti 0.02

F and Cr contents were also measured but all values were <mdl (0.17wt%, 0.01wt%, respectively)

Table A1. Microprobe analyses of feldspar group minerals (continued)

	RG25		RG29		K-spar	RG32				RG36	
	albite		plagioclase			plagioclase	K-feldspar		plagioclase		
	mean	SD	mean	SD		mean	SD	mean	SD	mean	SD
	n=4		n=3		n=8		n=3		n=3		
(Wt.%)											
CaO	2.69	1.42	2.44	0.69	<mdl	3.60	1.87	<mdl		4.25	0.54
Na2O	10.32	0.79	10.50	0.39	0.04	9.82	1.05	0.15	0.20	9.56	0.44
K2O	0.06	0.04	0.05	0.01	16.34	0.15	0.14	16.27	0.14	0.22	0.09
FeO	0.17	0.22	0.19	0.01	<mdl	0.23	0.29	0.36	0.36	0.12	0.03
TiO2	<mdl		<mdl		0.03	<mdl		<mdl		0.05	0.04
MgO	<mdl		<mdl		<mdl	0.07	0.15	<mdl		<mdl	
SiO2	64.50	2.09	63.67	1.21	64.15	63.87	2.29	63.03	1.97	63.65	0.70
MnO	<mdl		0.03	0.02	<mdl	<mdl		<mdl		<mdl	
Al2O3	22.27	0.99	20.15	0.63	17.64	22.73	1.30	18.28	0.25	23.09	0.06
Cl	<mdl		<mdl		<mdl	<mdl		<mdl		<mdl	
Total	100.0		97.0		98.2	100.4		98.1		100.9	
Formula calculated to 8 O											
a.p.f.u.											
Ca	0.127	0.068	0.119	0.034	-	0.170	0.089	-	0.000	0.200	0.027
Na	0.882	0.061	0.925	0.028	0.003	0.838	0.082	0.014	0.018	0.813	0.031
K	0.003	0.002	0.003	0.000	0.981	0.008	0.008	0.981	0.015	0.012	0.005
Total	1.012	0.010	1.047	0.010	0.984	1.016	0.016	0.995	0.008	1.026	0.009
Al	1.157	0.060	1.080	0.038	0.978	1.179	0.076	1.018	0.033	1.194	0.007
Si	2.843	0.067	2.894	0.039	3.019	2.811	0.076	2.980	0.033	2.793	0.010
Mg	-		-		-	0.005	0.010	-		-	
Fe	0.006	0.008	0.007	0.001	-	0.008	0.011	0.014	0.014	0.004	0.001
Mn	-		0.001	0.001	-	-		-		-	0.000
Ti	-		-		-	-		-		0.002	0.001
Total	0.007	0.008	0.009	0.001	0.002	0.014	0.020	0.015	0.015	0.008	0.001
ab %	87.1	6.8	88.4	3.2	0.3	82.4	8.3	1.4	1.8	79.3	2.4
an %	12.6	6.6	11.3	3.2	0.0	16.7	8.7	0.0	0.0	19.5	2.8
Kfs %	0.3	0.2	0.3	0.0	99.7	0.8	0.8	98.6	1.8	1.2	0.5

Detection Limits (wt%) Al 0.01, Ca 0.02, Cr 0.01, Cl 0.02, Fe 0.03, K 0.01, Mn 0.03, Mg 0.02, Na 0.04, P 0.03, Si 0.02, Ti 0.02

F and Cr contents were also measured but all values were <mdl (0.17wt%, 0.01wt%, respectively)

Table A2. Microprobe analyses of biotite group minerals

(Wt.%)	RG45		RG43		RG50		RG27		RG36		RG25		RG32		RG29		
	mean	SD	mean	SD	mean	SD	mean	SD	mean	SD	mean	SD	mean	SD	mean	SD	
			n=3		n=9		n=30		n=18		n=18		n=5		I n=6		II n=3
CaO	0.00	0.13	0.03	0.48	1.36	0.03	0.06	0.03	0.06	0.18	0.56	<mdl	<mdl	<mdl	<mdl	<mdl	<mdl
Na2O	0.06	0.06	0.04	0.05	0.03	0.05	0.03	0.22	0.48	0.11	0.23	0.06	0.03	0.07	0.03	0.08	0.05
K2O	9.41	8.05	0.65	9.37	0.43	9.38	0.18	9.48	0.58	9.28	0.59	9.55	0.10	9.28	0.44	8.92	0.50
FeO	18.80	26.49	0.85	22.68	1.17	19.54	0.53	17.82	1.54	17.19	0.71	19.92	0.39	18.29	2.17	15.57	0.75
TiO2	0.57	1.16	0.04	0.96	1.71	0.65	0.05	0.90	0.24	0.97	0.52	0.74	0.06	0.68	0.07	0.74	0.07
MgO	12.36	5.87	0.04	8.43	0.73	11.47	0.35	10.38	0.81	11.97	0.66	10.54	0.29	11.74	1.93	14.21	0.09
SiO2	38.31	34.33	0.26	35.42	0.55	36.59	0.62	38.01	4.17	36.31	1.67	36.48	0.67	36.90	1.27	37.12	0.85
MnO	0.36	0.25	0.04	0.30	0.05	0.32	0.05	0.22	0.05	0.19	0.03	0.27	0.05	0.28	0.06	0.22	0.01
Cr2O3	0.02	0.01	0.01	<mdl		0.01	0.01	0.02	0.01	0.02	0.01	0.02	0.01	0.01	0.01	<mdl	
Al2O3	15.19	17.41	0.33	16.26	0.64	15.27	0.32	17.19	1.25	16.63	0.68	16.73	0.28	16.18	0.73	16.29	0.32
F	2.71	0.50	0.04	1.44	0.11	2.45	0.13	0.89	0.06	1.23	0.10	1.71	0.11	1.74	0.39	1.28	0.12
Cl	0.05	0.08	0.01	0.07	0.03	0.06	0.02	0.04	0.02	0.06	0.02	0.06	0.01	0.06	0.02	0.06	0.03
Total	97.77	94.16		95.45		95.74		94.94		94.13		96.07		95.23		94.49	1.02

Formula based on Biotite K2(Fe,Mg,Mn)6Al2Si6O20(OH,F)4

Na	0.019	0.019	0.012	0.014	0.009	0.016	0.010	0.019	0.006	0.031	0.067	0.019	0.009	0.020	0.005	0.022	0.014
K	1.823	1.641	0.131	1.887	0.093	1.852	0.037	1.894	0.024	1.831	0.081	1.882	0.020	1.879	0.127	1.734	0.084
Total	1.841	1.660		1.901		1.868		1.913		1.862		1.901		1.899		1.756	
Mg	2.796	1.399	0.005	1.983	0.178	2.668	0.072	2.470	0.043	2.763	0.120	2.425	0.054	2.431	0.055	3.228	0.030
Fe	2.387	3.541	0.115	2.994	0.155	2.574	0.068	2.395	0.049	2.227	0.090	2.573	0.063	2.554	0.070	1.985	0.108
Mn	0.047	0.034	0.006	0.040	0.007	0.040	0.006	0.027	0.006	0.024	0.005	0.036	0.006	0.042	0.006	0.028	0.002
Ca	0.000	0.022	0.005	0.080	0.228	0.003	0.003	0.001	0.002	0.029	0.091	-		-		-	
Ti	0.066	0.139	0.005	0.113	0.201	0.077	0.005	0.108	0.019	0.113	0.059	0.087	0.008	0.075	0.006	0.085	0.008
Total	5.296	5.134		5.211		5.362		5.000		5.156		5.122		5.105		5.327	
Al	2.719	3.280	0.046	3.026	0.131	2.813	0.069	3.155	0.062	3.036	0.072	3.046	0.064	2.953	0.040	2.927	0.051
Cr	0.003	0.001	0.002	-		0.001	0.001	0.002	0.002	0.002	0.002	0.002	0.002	0.001	0.002	-	
Total	2.721	3.282		3.027		2.814		3.157		3.038		3.048		2.955		2.928	
Si	5.818	5.487	0.049	5.593	0.097	5.703	0.061	5.600	0.029	5.622	0.076	5.635	0.070	5.719	0.027	5.659	0.073
F	1.301	0.254	0.021	0.720	0.057	1.200	0.077	0.432	0.031	0.606	0.054	0.833	0.050	0.972	0.143	0.617	0.063
Cl	0.012	0.021	0.003	0.018	0.008	0.017	0.006	0.011	0.007	0.015	0.006	0.016	0.003	0.016	0.005	0.016	0.007
OH	2.687	3.725	0.022	3.262	0.054	2.783	0.075	3.557	0.029	3.379	0.054	3.151	0.051	3.011	0.146	3.367	0.058
Total	4.000	4.000		4.000		4.000		4.000		4.000		4.000		4.000		4.000	
TOTAL	19.68	19.56		19.73		19.75		19.67		19.68		19.70		19.68		19.67	
Mol.% end-members																	
Annite	45.1	69.0	0.6	57.6	4.3	48.0	1.2	47.9	0.7	43.2	1.4	50.2	0.9	50.0	0.9	37.3	1.1
Phlogopite	52.8	27.3	0.6	38.2	4.2	49.8	1.1	49.4	1.0	53.6	1.8	47.3	1.1	47.6	1.0	60.6	1.0
Fluorphlogopite	32.5	6.3	0.5	18.0	1.4	30.0	1.9	10.8	0.8	15.1	1.4	20.8	1.2	24.3	3.6	15.4	1.6

Detection Limits (wt%) Al 0.01, Ca 0.02, Cr 0.01, Cl 0.02, F 0.17, Fe 0.03, K 0.01, Mn 0.03, Mg 0.02, Na 0.04, P 0.03, Si 0.02, Ti 0.02

Table A3. Microprobe analyses of muscovite group minerals

	RG29		RG32		RG42		RG43		RG45	
	mean	SD	mean	SD	mean	SD	mean	SD	mean	SD
(Wt.%)	n=3		n=7		n=6		n=2		n=3	
CaO	<mdl		0.05	0.11	<mdl		<mdl		0.02	0.01
Na ₂ O	0.23	0.04	0.36	0.43	0.15	0.04	0.16	0.02	0.17	0.03
K ₂ O	10.01	0.25	9.30	2.10	10.34	1.41	11.01	0.01	10.73	0.18
FeO	2.76	0.47	2.34	0.58	4.40	1.09	3.81	0.37	1.89	0.09
TiO ₂	0.10	0.03	0.12	0.04	0.08	0.03	0.22	0.11	<mdl	
MgO	2.03	0.09	1.86	0.43	1.22	0.28	1.28	0.40	0.62	0.04
SiO ₂	47.77	1.03	51.33	9.80	47.23	1.15	47.22	0.98	46.23	0.42
MnO	0.06	0.01	0.03	0.02	0.03	0.03	0.09	0.02	0.03	0.02
Cr ₂ O ₃	<mdl		0.02	0.01	0.01	0.01	<mdl		0.01	0.02
Al ₂ O ₃	31.30	0.40	29.69	5.80	31.23	1.80	31.59	1.80	34.37	0.33
F	0.69	0.08	0.49	0.14	0.39	0.05	0.47	0.02	<mdl	
Cl	<mdl		<mdl		<mdl		<mdl		0.02	0.01
Total	94.94		95.57		95.08		95.85		94.09	

Formula on basis of KAl₂(Si₃Al)O₁₀(OH,F)₂

Na	0.029	0.005	0.044	0.049	0.020	0.005	0.021	0.003	0.022	0.004
K	0.862	0.023	0.791	0.194	0.898	0.137	0.948	0.000	0.925	0.013
Total	0.891		0.835		0.918		0.968		0.947	
Total Al	2.490	0.025	2.332	0.513	2.497	0.095	2.513	0.140	2.737	0.033
Si	3.223	0.040	3.375	0.458	3.206	0.038	3.187	0.070	3.123	0.020
Al (iv)	0.777	0.040	0.625	0.458	0.794	0.038	0.813	0.070	0.877	0.020
Total	4.000		4.000		4.000		4.000		4.000	
Al (iv)	1.712	0.021	1.708	0.055	1.702	0.079	1.700	0.070	1.860	0.013
Cr	-		0.001	0.001	0.001	0.000	-		0.001	0.001
Mg	0.204	0.012	0.185	0.046	0.123	0.030	0.129	0.041	0.063	0.004
Fe	0.156	0.028	0.131	0.036	0.250	0.063	0.215	0.021	0.107	0.005
Mn	0.003	0.001	0.002	0.001	0.002	0.002	0.005	0.001	0.002	0.001
Ca	-		0.003	0.007	-		-		0.001	0.001
Ti	0.005	0.002	0.006	0.002	0.004	0.001	0.011	0.005	-	
Total	2.082		2.035		2.083		2.061		2.034	
TOTAL	6.973		6.870		7.001		7.029		6.981	
F	0.148	0.016	0.103	0.032	0.085	0.012	0.101	0.005	0.025	0.019
Cl	0.000		0.000		0.000		0.000		0.002	0.001
OH	1.852	0.016	1.896	0.033	1.915	0.012	1.899	0.005	1.973	0.019
Total	2.000		2.000		2.000		2.000		2.000	
Phengite component %	17.7	1.8	15.9	3.0	18.2	2.9	17.5	3.2	8.5	0.4
Fe/(Fe+Mg)	0.43	0.03	0.41	0.02	0.66	0.08	0.63	0.05	0.63	0.01
% F-end-member	7.4	0.8	5.2	1.6	4.2	0.6	5.0	0.2	1.2	1.0
% Cl-end-member	0.0	0.0	0.0	0.0	0.0	0.0	0.0	0.0	0.1	0.0

Detection Limits (wt%) Al 0.01, Ca 0.02, Cr 0.01, Cl 0.02, F 0.17, Fe 0.03, K 0.01, Mn 0.03, Mg 0.02, Na 0.04, P 0.03, Si 0.02, Ti 0.02

Table A4. Microprobe analyses of epidote group minerals

	RG42		RG43		RG45		RG49		RG50		RG21	RG25	RG29		RG36	
	mean	SD	mean	SD	mean	SD	mean	SD	mean	SD			mean	SD	mean	SD
(Wt.%)	n=25		n=10		n=20		n=10		n=19				n=24		n=34	
CaO	24.77	0.33	23.75	0.81	24.31	0.36	24.25	0.35	24.28	0.94	22.03	24.69	24.69	0.19	24.70	0.46
Na2O	<mdl		0.05	0.04	<mdl		<mdl		0.08	0.17	<mdl	<mdl	<mdl		<mdl	
K2O	0.01	0.01	0.01	0.01	0.02	0.01	0.01	0.01	0.01	0.02	0.12	<mdl	0.01	0.01	0.01	0.01
FeO (meas.)	7.71	1.20	8.78	0.51	8.04	0.99	10.53	2.19	8.16	1.92	11.40	6.11	6.60	0.57	7.99	1.16
Fe2O3 (calc.)	8.57	1.33	9.76	0.57	8.94	1.11	11.70	2.43	9.07	2.13	12.67	6.79	7.33	0.63	8.89	1.28
TiO2	<mdl		0.04	0.03	0.03	0.03	0.06	0.04	0.34	0.94	0.05	<mdl	0.04	0.04	0.04	0.04
MgO	<mdl		<mdl		<mdl		<mdl		0.03	0.04	0.65	<mdl	<mdl		<mdl	
SiO2	37.80	0.53	37.52	0.22	37.65	0.28	36.80	1.12	37.72	0.72	35.05	38.29	37.41	0.70	37.92	0.41
MnO	0.07	0.07	0.13	0.05	0.12	0.09	0.07	0.07	0.12	0.07	0.17	0.14	0.17	0.06	0.07	0.05
Cr2O3	0.01	0.01	0.01	0.01	0.01	0.01	0.01	0.01	0.01	0.01	0.03	0.03	0.01	0.01	0.01	0.02
Al2O3	26.95	1.16	25.34	0.54	26.09	0.82	24.51	2.02	26.08	2.10	23.64	28.22	27.00	0.67	26.49	1.07
F	<mdl		0.21	0.08	0.18	0.06	0.19	0.04	0.17	0.08	0.16	<mdl	0.17	0.05	<mdl	
Cl	<mdl		0.04	0.05	<mdl		<mdl		<mdl		0.02	<mdl	<mdl		<mdl	
Total	98.17		96.86		97.33		97.59		97.92		94.60	98.16	96.84		98.13	
Formula, based on Ca2(Al,Fe3+)3Si3O12(OH)																
Ca	2.079	0.014	2.031	0.044	2.064	0.023	2.078	0.024	2.050	0.065	1.95184	2.05625	2.0991	0.03053	2.07601	0.02753
Na	-		0.008	0.006	-		-		0.012	0.026	-	-	-		-	
K	0.001	0.001	0.001	0.001	0.002	0.001	0.001	0.001	0.002	0.003	0.01301	-	0.001	0.001	0.001	0.00114
Total	2.082		2.040		2.068		2.081		2.064		1.9657	2.0563	2.102		2.0788	
Cr	0.001	0.001	0.001	0.001	0.001	0.001	0.001	0.001	0.001	0.001	0.002	0.002	0.001	0.001	0.001	0.001
Mg	-		-		-		-		0.003	0.005	0.080	-	-		-	
Fe	0.506	0.083	0.586	0.031	0.533	0.066	0.707	0.159	0.539	0.135	0.789	0.397	0.438	0.038	0.525	0.079
Mn	0.004	0.005	0.009	0.004	0.008	0.006	0.004	0.005	0.008	0.005	0.012	0.009	0.012	0.004	0.004	0.003
Ti	-		0.002	0.002	0.002	0.002	0.003	0.003	0.020	0.056	0.003	-	0.002	0.002	0.003	0.002
Al	2.488	0.085	2.385	0.029	2.437	0.072	2.309	0.147	2.422	0.167	2.305	2.586	2.525	0.038	2.449	0.078
Total	2.999		2.984		2.980		3.024		2.993		3.191	2.995	2.978		2.982	
Si	2.961	0.018	2.996	0.035	2.984	0.015	2.943	0.034	2.974	0.044	2.900	2.977	2.969	0.011	2.975	0.023
(OH)	0.961	0.015	0.942	0.027	0.952	0.015	0.952	0.010	0.956	0.020	0.955	0.971	0.957	0.012	0.961	0.015
F	-		0.053	0.021	0.046	0.016	0.047	0.011	0.043	0.020	0.042	-	0.043	0.012	-	
Cl	-		0.005	0.007	-		-		-		0.003	-	-		-	
XFe	16.9	2.7	19.6	1.0	17.9	2.2	23.4	5.1	18.0	4.5	24.7	13.3	14.7	1.3	17.6	2.6
XMn	0.1	0.2	0.3	0.1	0.3	0.2	0.1	0.2	0.3	0.2	0.4	0.3	0.4	0.1	0.1	0.1
XAl	82.9	2.8	79.9	1.0	81.8	2.3	76.4	5.1	80.9	5.2	72.2	86.3	84.8	1.2	82.1	2.6

Detection Limits (wt%) Al 0.01, Ca 0.02, Cr 0.01, Cl 0.02, F 0.17, Fe 0.03, K 0.01, Mn 0.03, Mg 0.02, Na 0.04, P 0.03, Si 0.02, Ti 0.02

Table A5. Electron probe microanalyses of stilbite

	RG27							
	p7_1	p7_2	l8.1	l8.2	l9.1	l9.2	l12.1	l12.2
(Wt.%)								
CaO	9.30	8.92	9.16	9.32	9.16	9.17	7.78	8.71
Na2O	1.70	1.29	1.55	0.52	1.04	1.19	1.22	1.27
K2O	0.12	0.11	0.13	0.14	0.19	0.13	1.35	0.38
FeO	<mdl	<mdl	<mdl	<mdl	<mdl	<mdl	1.98	<mdl
TiO2	<mdl	0.04	<mdl	<mdl	<mdl	<mdl	0.12	0.09
MgO	<mdl	<mdl	0.02	0.03	<mdl	0.02	1.11	0.08
SiO2	61.69	62.17	60.74	60.98	61.74	61.44	58.60	59.71
MnO	<mdl	<mdl	<mdl	<mdl	<mdl	<mdl	<mdl	0.03
Cr2O3	<mdl	<mdl	<mdl	<mdl	0.03	<mdl	<mdl	<mdl
Al2O3	18.45	18.69	19.38	18.62	17.95	18.45	17.89	17.89
F (wt.%)	<mdl	<mdl	<mdl	0.19	<mdl	<mdl	<mdl	<mdl
Cl (wt.%)	<mdl	<mdl	<mdl	<mdl	<mdl	0.02	0.02	0.02
Total	91.25	91.22	90.97	89.79	90.12	90.42	88.09	88.18
Formulae based on NaCa4[Al9Si27O72]· nH2O								
Ca	4.24	4.06	4.20	4.30	4.22	4.22	3.69	4.13
Na	1.40	1.07	1.28	0.44	0.87	0.99	1.05	1.09
K	0.06	0.06	0.07	0.07	0.10	0.07	0.76	0.22
Total	5.70	5.18	5.56	4.81	5.19	5.28	5.50	5.44
Cr	-	-	-	-	0.01	-	-	-
Mg	-	-	0.01	0.02	-	0.02	0.73	0.05
Fe	-	-	-	-	-	-	0.48	-
Mn	-	-	-	-	-	-	-	0.01
Ti	-	0.01	-	-	-	-	0.04	0.03
Al	9.26	9.36	9.79	9.46	9.09	9.34	9.33	9.33
Total	9.67	9.71	10.04	9.93	9.49	9.64	10.59	9.58
Si	26.26	26.41	26.03	26.28	26.53	26.39	25.93	26.43

Detection Limits (wt%) Al 0.01, Ca 0.02, Cr 0.01, Cl 0.02, F 0.17, Fe 0.03, K 0.01, Mn 0.03, Mg 0.02, Na 0.04, P 0.03, Si 0.02, Ti 0.02

Table A6. Electron probe microanalyses of pyrite, pentlandite, argentopentlandite, cubanite, mackinawite and Fe-Ni-thiospinel

	P Y R I T E		PENTLANDITE		ARGENTOPENTLANDITE		CUBANITE			CO-NI MACKINAWITE			FE-NI THIOSPINEL	
	RG18		RG24		RG25		RG24	RG36		RG11	RG36	RG36		
	mean	SD	mean	SD	mean	SD	mean	SD	mean	SD	mean	SD	mean	SD
Wt.%	n=31		n=5		n=3		n=18			n=8			n=3	
Ag			<mdl		11.47	1.13	<mdl			<mdl			<mdl	
Cu	<mdl		1.19	1.04	2.17	1.31	23.36	22.95	0.24	0.59	0.30	0.40	0.44	0.20
Fe	45.94	0.46	32.11	0.50	37.04	1.14	39.67	40.52	0.21	53.06	1.06	56.23	35.57	3.89
Co	0.08	0.06	4.68	0.88	0.19	0.17	<mdl	<mdl		4.99	1.57	0.32	0.38	0.19
Ni	0.04	0.03	27.54	2.15	15.98	0.40	<mdl	<mdl		3.69	0.48	5.20	20.18	1.52
S	52.91	1.75	33.25	0.25	32.05	0.66	35.40	35.58	0.20	35.63	0.56	35.54	40.35	1.22
Total	98.97		98.77		98.90		98.42	99.04		97.96		97.69	96.92	
Formula (3 a.p.f.u.)			Formula (17 a.p.f.u.)		Formula (17 a.p.f.u.)		Formula (6 a.p.f.u.)			Formula (2 a.p.f.u.)			Formula (7 a.p.f.u.)	
Ag			-		0.916 0.102		-			-			-	
Cu	0.000	0.000	0.146	0.127	0.293	0.176	1.010	0.986	0.010	0.008	0.004	0.006	0.022	0.010
Fe	0.997	0.026	4.483	0.058	5.714	0.246	1.952	1.982	0.009	0.856	0.019	0.909	1.978	0.203
Co	0.002	0.001	0.620	0.118	0.027	0.025	-	-		0.076	0.024	0.005	0.020	0.010
Ni	0.001	0.001	3.659	0.286	2.345	0.028	-	-		0.057	0.008	0.080	1.068	0.084
Total M	1.000	0.027	8.911	0.040	8.387	0.060	2.966	2.968	0.009	0.999	0.004	0.999	3.088	0.108
S	2.000	0.027	8.089	0.040	8.613	0.060	3.034	3.032	0.009	1.001	0.004	1.001	3.912	0.108
M/S	0.50	0.02	1.10	0.01	0.97	0.01	0.98	0.98	0.01	0.997	0.009	0.999	0.790	0.049

Detection limits (wt%) Ag 0.15, Cu 0.06, Co 0.04, Ni 0.03, Fe 0.05, S 0.06

Mn, As, Sb and Se were also measured; all were <mdl (0.03, 0.15, 0.09 and 0.15 wt%, respectively)

Table A7. LA-ICPMS data of molybdenite.

	FileName	SampleName	Fe57	Co59	Ni60	Cu65	Zn66	As75	Se77	Ag107	Sn118	Sb121	Te125	W182	Re185	Au197	Tl205	Pb208	Bi209	U238
Open Pit																				
ABreccia	AU04A235	NK25.A1	1448	5.5	13	135	3.7	8.5	821	2.15	0.11	12	119	89	143	18	3.1	241	335	0.01
	AU04A236	NK25.A2	3977	21	44	100	5.6	19	645	2.82	0.33	22	151	218	541	7.5	14	257	641	0.19
	AU04A237	NK25.A3	14635	8.1	28	101	21	40	683	3.10	0.37	12	123	107	328	9.4	2.8	217	365	0.52
	AU04A238	NK25.A4	24539	12	44	74	32	29	701	7.23	0.86	21	139	207	206	23	5.1	244	504	0.07
	AU04A239	NK25.A5	813	1.7	5.8	111	2.7	5.1	516	1.01	0.85	3.3	47	239	905	7.8	1.6	57	162	0.00
	AU04A240	NK25.A6	3086	1.8	6.6	72	5.8	6.4	666	1.29	1.2	2.9	81	86	288	11	1.1	50	115	0.02
	AU04A241	NK25.A7	4536	1.9	8.5	68	8.4	4.9	634	1.26	2.2	5.8	45	125	232	17	0.31	70	82	0.01
	AU04A242	NK25.A8	1387	2.2	6.5	391	10	7.5	930	2.27	4.9	8.4	133	69	94	27	0.35	123	282	0.00
	AU04A243	NK25.A9	18495	6.6	31	152	33	18	710	3.27	1.9	12	94	216	360	18	2.0	134	259	0.02
	AU04A244	NK25.A10	30682	24	66	76	47	48	673	5.27	1.9	30	143	262	646	10	5.6	440	685	2.9
Central Diorite																				
	FileName	SampleName	Fe57	Co59	Ni60	Cu65	Zn66	As75	Se77	Ag107	Sn118	Sb121	Te125	W182	Re185	Au197	Tl205	Pb208	Bi209	U238
	AU04A109	RG8.1	1532	2.1	2.7	400	41	2.3	705	13	3.1	1.0	121	76	88	20	0.31	86	271	0.01
	AU04A110	RG8.2	2308	11	15	1537	62	5.0	534	28	3.3	12	143	58	481	50	1.0	365	682	0.10
	AU04A111	RG8.3	657	0.89	2.6	118	10	1.3	686	1.5	0.61	0.92	83	71	37	2.1	0.05	42	54	0.00
	AU04A112	RG8.4	1274	4.2	7.3	236	9.5	15	446	219	6.9	3.1	400	338	59	347	0.43	239	2855	0.04
	AU04A113	RG8.5	3284	5.8	9.6	195	19	4.4	420	87	2.0	2.6	114	143	137	152	1.0	182	808	0.05
	AU04A114	RG8.6	3376	3.4	6.6	2050	94	3.4	652	38	2.4	5.9	184	118	105	50	1.3	210	530	0.01
	AU04A115	RG8.7	3797	5.8	9.4	2102	63	4.5	560	57	4.1	12	307	112	129	92	2.0	338	1561	0.02
	AU04A116	RG8.8	4244	4.2	8.5	899	97	3.3	493	23	17	4.7	151	94	99	27	0.84	187	541	0.04
	AU04A117	RG8.9	1398	15	20	701	20	6.9	606	94	3.2	12	393	151	94	118	2.9	458	2164	0.09
	AU04A118	RG8.10	984	7.8	9.1	687	15	5.8	655	85	2.3	10	432	101	97	128	0.62	325	2344	0.03
	AU04A119	RG8.11	6165	7.5	11	6269	28	3.0	543	130	2.8	6.2	164	99	54	145	3.0	268	781	0.00
	AU04A120	RG8.12	8984	2.8	4.9	193	182	6.3	474	2.1	1.2	0.2	16	113	61	2.8	0.34	25	42	0.03
	AU04A121	RG8.13	457	0.47	1.1	98	3.8	1.4	711	5.9	0.28	1.4	91	125	99	10	0.12	41	83	0.00
	AU04A122	RG8.14	253	2.1	3.5	209	6.0	2.8	567	26	0.4	6.7	98	67	36	39	0.19	131	361	0.00
	AU04A123	RG8.15	18444	42	49	894	37	6.5	486	67	0.8	2.7	178	265	127	126	0.61	202	1116	0.05
	AU04A124	RG8.16	4350	2.6	3.8	361	19	6.9	465	7.1	1.9	0.4	79	549	101	13	0.15	65	234	0.03
	AU04A125	RG8.17	4985	3.5	7.4	168	18	2.8	486	17	1.4	1.0	218	273	183	58	0.04	45	629	0.11
	AU04A126	RG8.18	1845	4.0	7.3	483	17	3.3	633	35	1.8	7.6	209	105	103	46	1.0	213	685	0.02
	AU04A127	RG8.19	35218	19	45	2258	129	7.5	414	70	1.1	15	274	139	98	104	0.84	362	1424	0.05
	AU04A128	RG8.20	6418	7.1	22	54	3.3	1.9	518	16	0.24	2.1	99	59	261	23	0.20	88	363	0.00
	FileName	SampleName	Fe57	Co59	Ni60	Cu65	Zn66	As75	Se77	Ag107	Sn118	Sb121	Te125	W182	Re185	Au197	Tl205	Pb208	Bi209	U238

AU04A076	RG10.1	821	4.1	7.2	12	8.2	11	1358	27	3.57	7.1	245	79	304	46	5.3	378	599	0.10
AU04A077	RG10.2	10035	5.6	12.2	15	36	21	1016	115	2.11	11	273	536	248	126	4.5	323	600	0.07
AU04A078	RG10.3	1050	0.67	1.5	9.4	4.1	5.2	1068	11	1.49	3.8	231	89	437	4.5	0.58	41	366	0.02
AU04A081	RG10.4	568	1.6	1.6	24	3.7	5.5	1191	29	0.35	7.2	634	29	150	18	0.64	322	1338	0.00
AU04A082	RG10.5	4500	2.4	3.4	51	29	15	1256	14	2.10	20	370	105	232	23	1.9	402	662	0.00
AU04A083	RG10.6	7379	3.3	6.0	15	24	12	779	8.2	0.47	6.5	170	392	212	18	1.5	321	353	0.01
AU04A084	RG10.7	5821	2.0	4.5	21	21	10	1165	6.4	1.36	7.6	249	72	286	25	0.63	203	401	0.01
AU04A085	RG10.8	1137	1.1	1.6	10	7.3	6.3	1337	7.9	0.12	2.2	300	44	368	11	0.81	179	524	0.00
AU04A086	RG10.9	2692	1.6	2.6	8.8	11	16	1543	13	0.24	3.3	371	25	392	12	2.4	231	578	0.12
AU04A087	RG10.10	58	0.41	0.55	6.4	1.5	30	1302	6.6	0.91	1.3	307	8.1	713	20	0.37	106	528	0.05
AU04A088	RG10.11	167	0.15	0.25	2.7	1.9	32	1288	0.16	0.13	0.33	161	50	578	0.6	0.03	16	34	0.00
AU04A089	RG10.12	12669	4.6	9.0	27	43	10	892	12	0.65	22	174	162	247	18	2.6	361	371	0.01
AU04A090	RG10.13	1103	0.51	0.91	8.8	4.0	3.6	995	1.1	0.18	1.3	145	92	416	7.9	0.06	95	167	0.00
AU04A091	RG10.14	1829	1.2	2.1	5.7	10	5.1	893	3.3	0.15	4.1	133	91	325	11	1.4	146	201	0.00
AU04A092	RG10.15	212	0.44	0.73	13	9.5	5.3	1153	27	0.44	1.7	670	57	337	11	0.55	126	1230	0.00

WBD10630001 Central Diorite

FileName	SampleName	Fe57	Co59	Ni60	Cu65	Zn66	As75	Se77	Ag107	Sn118	Sb121	Te125	W182	Re185	Au197	Tl205	Pb208	Bi209	U238
AU04A036	RG25.1	13129	22	33	53	41	16	484	51	2.4	3.1	728	312	2.9	16	1.5	1267	2299	0.93
AU04A037	RG25.2	3039	13	16	343	21	6.1	673	20	2.4	2.6	552	243	3.1	1.6	2.9	708	894	0.26
AU04A038	RG25.3	13823	8.1	27	57	40	12	545	112	1.7	5.1	398	375	16	187	1.5	1165	1410	0.33
AU04A039	RG25.4	141646	37	172	94	339	15	719	29	8.3	7.2	1065	406	3.3	33	5.0	1596	3789	1.3
AU04A040	RG25.5	16888	23	46	1201	84	15	702	36	6.4	12	807	360	2.9	43	4.7	1363	3036	0.99
AU04A041	RG25.6	34064	24	73	47	90	14	513	36	4.2	10	1118	252	1.8	45	3.4	3440	4707	0.27
AU04A042	RG25.7	113772	54	187	96	343	24	683	139	8.0	19	1977	823	12.1	197	7.4	3178	7522	1.4
AU04A043	RG25.8	26999	13	56	169	86	13	462	46	3.2	7.3	288	296	1.5	70	5.0	1748	1003	0.55
AU04A044	RG25.9	2733	3.3	11	20	9.2	6.8	472	15	0.7	3.3	198	247	2.6	24	1.0	785	818	0.07
AU04A045	RG25.10	10268	6.6	22	85	30	9.2	506	229	2.0	7.2	643	270	5.4	314	1.9	1117	2349	0.16
AU04A046	RG25.11	1101	0.87	3.1	29	4.6	5.8	638	3.3	0.24	0.79	40	197	1.3	7.3	0.29	178	71	0.02
AU04A047	RG25.12	1423	1.7	5.7	6.6	5.9	4.7	608	2.4	0.35	1.2	72	142	1.5	3.1	0.69	150	186	0.03
AU04A048	RG25.13	5435	8.7	22	58	16	4.1	596	11	2.7	7.0	610	182	9.2	12	3.0	994	1497	0.09
AU04A049	RG25.14	55970	33	104	118	146	20	706	46	4.5	14	1275	565	6.1	62	5.5	2886	4959	0.50
AU04A050	RG25.15	13263	18	50	136	43	8.3	645	136	3.4	19	3912	225	4.1	117	4.3	3333	12108	0.04
AU04A051	RG25.16	2341	15	49	157	6.6	3.3	740	39	3.0	8.4	632	190	7.0	41	8.5	1282	2363	0.00
AU04A052	RG25.17	610	9.5	21	22	36	10	563	13	1.2	7.3	393	113	0.34	10	3.4	862	782	0.03

WBD105900002

FileName	SampleName	Fe57	Co59	Ni60	Cu65	Zn66	As75	Se77	Ag107	Sn118	Sb121	Te125	W182	Re185	Au197	Tl205	Pb208	Bi209	U238
----------	------------	------	------	------	------	------	------	------	-------	-------	-------	-------	------	-------	-------	-------	-------	-------	------

AU04A129	RG27.1	1662	1.1	11	91	16	3.8	428	1.1	3.1	0.27	23	133	26	3.9	0.34	58	40	0.13
AU04A130	RG27.2	4477	6.7	26	4267	30	2.8	786	2.8	9.9	1.01	85	54	131	14	0.82	155	94	0.00
AU04A131	RG27.3	3068	3.9	8.8	1368	17	1.8	605	0.98	2.8	1.12	72	51	234	5.2	0.38	304	132	0.01
AU04A132	RG27.4	6338	5.2	14	1357	66	2.2	492	3.1	89	1.20	64	112	46	22	0.52	181	247	0.28
AU04A133	RG27.5	4921	0.8	2.8	110	16	3.0	750	0.14	3.5	0.16	69	60	117	0.49	0.09	9.1	12	0.03
AU04A134	RG27.6	283	0.7	2.1	191	13	2.7	465	0.50	0.65	0.07	25	98	79	3.6	0.01	6.5	18	0.00
AU04A135	RG27.7	5137	3.9	20	1767	80	5.0	502	2.1	8.4	0.95	57	78	22	13	1.1	198	175	0.02
AU04A138	RG27.8	4962	1.5	6.4	13	11	7.6	392	0.6	0.47	0.14	54	76	162	0.17	0.52	16	70	0.01
AU04A139	RG27.9	7051	29	104	199	64	11	439	129	5.4	0.39	40	162	98	14	0.81	57	363	0.03
AU04A140	RG27.10	3069	1.5	3.6	3430	16	10	376	2.8	4.5	0.38	41	56	8.4	12	0.07	42	65	0.00
AU04A141	RG27.11	12591	13	30	3211	165	4.9	467	10	55	4.24	69	280	122	43	1.15	399	361	0.43
AU04A142	RG27.12	5526	2.4	8.5	1112	36	2.2	436	1.2	7.4	0.71	20	99	347	4.4	0.45	71	41	0.08
AU04A143	RG27.13	9601	4.3	15	1200	123	4.0	397	0.97	5.7	0.76	41	107	48	6.2	0.91	112	132	0.30
AU04A144	RG27.14	7493	3.6	24	1242	38	4.5	292	1.1	13	0.41	22	119	291	7.5	0.80	53	39	0.02
AU04A145	RG27.15	3.9	0.14	0.17	2.8	0.41	15	390	0.05	0.12	0.02	22	135	59	0.20	0.01	4.4	6.8	0.00
AU04A146	RG27.16	573	0.27	2.4	618	2.2	1.4	539	0.16	0.69	0.22	25	42	221	0.21	0.01	12	6.0	0.00
FileName	SampleName	Fe57	Co59	Ni60	Cu65	Zn66	As75	Se77	Ag107	Sn118	Sb121	Te125	W182	Re185	Au197	Tl205	Pb208	Bi209	U238
AU04A163	RG29.1	3155	0.62	3.1	10	7.5	16	493	0.24	1.02	0.74	44	79	0.44	6.7	0.14	45	153	0.06
AU04A164	RG29.2	1633	1.3	4.3	106	11	2.0	411	17	11	1.0	118	95	0.13	66	0.10	257	586	10
AU04A165	RG29.3	73	0.23	0.31	4.7	2.6	1.5	427	0.16	0.23	0.12	60	61	0.24	3.4	0.01	13	25	0.06
AU04A166	RG29.4	1012	1.6	3.2	99	5.5	9.2	410	1.2	3.9	0.81	70	86	0.09	10	0.17	342	128	0.41
AU04A167	RG29.5	563	0.42	0.74	43	5.2	19	428	0.26	1.7	0.44	80	152	0.15	5.0	0.05	119	141	0.55
AU04A168	RG29.6	2.6	0.19	0.43	0.7	1.4	21	377	0.00	15.19	0.04	48	66	0.03	0.03	0.01	0.28	1.3	0.00
AU04A169	RG29.7	4606	0.64	1.6	43	12	6.2	417	5.7	4.26	0.90	79	57	0.22	67	0.04	71	694	0.39
AU04A170	RG29.8	1017	0.27	3.4	1137	22	2.0	368	0.90	1.0	0.45	399	73	0.11	12	0.02	85	626	0.00
AU04A171	RG29.9	3538	3.1	4.7	829	11	2.8	409	6.0	68	2.6	131	91	0.04	81	0.67	265	500	0.43
AU04A172	RG29.10	148	0.11	0.49	4.4	1.4	7.3	388	0.08	0.46	0.13	42	50	0.17	0.20	0.02	4.3	11	0.02
FileName	SampleName	Fe57	Co59	Ni60	Cu65	Zn66	As75	Se77	Ag107	Sn118	Sb121	Te125	W182	Re185	Au197	Tl205	Pb208	Bi209	U238
AU04A211	RG30.1	5680	0.70	3.7	362	10.8	3.1	320	0.06	2.9	0.24	51	67	0.09	0.24	0.21	19	7.4	0.03
AU04A212	RG30.2	2015	0.52	2.1	4.1	7.4	2.3	338	0.10	0.86	0.08	57	66	0.22	2.9	0.19	7.2	16	0.06
AU04A213	RG30.3	2397	1.0	2.5	87	7.7	0.5	341	0.37	3.4	0.18	66	112	0.03	6.7	0.22	23	48	0.05
AU04A214	RG30.4	5056	1.6	8.5	278	18.3	0.6	298	0.44	16	0.58	62	40	0.29	4.3	0.68	144	77	0.03
AU04A215	RG30.5	22554	5.1	25	41	52.0	4.4	275	421	22	4.1	456	230	1.8	1110	2.1	257	1166	1.5
AU04A216	RG30.6	27	0.44	0.38	21	1.2	2.0	340	0.03	0.37	0.17	49	43	0.57	0.34	0.01	150	5.7	0.01

AU04A217	RG30.7	666	0.99	1.8	79	2.5	3.6	346	1.4	4.9	2.5	120	58	0.21	24	0.08	181	299	0.04
AU04A218	RG30.8	439	0.63	1.5	63	3.9	0.5	317	0.73	14	1.2	105	42	0.16	8.7	0.12	155	211	0.03
AU04A219	RG30.9	461	0.66	1.0	1.3	1.7	25.8	318	0.07	0.99	0.13	42	65	0.03	0.35	0.04	1.4	4.4	0.04
AU04A220	RG30.10	1154	0.67	2.1	23	6.0	9.4	387	0.10	0.16	0.11	39	67	0.89	4.5	0.10	27	23	0.00

WRD09775002
GRANITE

FileName	SampleName	Fe57	Co59	Ni60	Cu65	Zn66	As75	Se77	Ag107	Sn118	Sb121	Te125	W182	Re185	Au197	Tl205	Pb208	Bi209	U238
AU04A183	RG40.1	4605	4.0	0.10	1242	50	4.5	323	6.7	6.0	2.8	4256	68	17	7.6	2.5	888	6195	0.93
AU04A184	RG40.2	668	2.9	0.03	86	6.4	3.2	89	6.0	1.4	1.8	643	289	3.4	13	0.67	437	952	0.34
AU04A185	RG40.3	2858	1.7	0.22	65	2.6	3.8	128	15	7.3	1.4	769	248	5.6	53	1.6	528	1073	14
AU04A186	RG40.4	88	0.73	0.02	7.2	0.64	1.5	92	0.79	0.16	0.48	40	364	4.6	0.48	0.05	85	52	0.0
AU04A187	RG40.5	10926	3.8	0.31	155	13	5.3	194	10	22	2.3	545	177	5.1	6.5	5.2	442	686	7.9
AU04A188	RG40.6	9650	6.5	0.20	106	23	10	188	6.3	16	3.0	652	265	5.3	17	4.3	963	930	12
AU04A189	RG40.7	0.0	0.00	0.00	0.77	0.30	0.45	357	0.0	0.1	0.02	67	35	4.2	0.00	0.00	0	0	0.0
AU04A190	RG40.8	2165	7.8	0.06	69	2.4	8.1	223	6.1	4.1	4.6	784	182	7.0	20	3.7	812	1132	1.1
AU04A191	RG40.9	2133	1.7	0.08	16	2.3	9.2	323	1.8	1.3	0.89	169	44	0.66	3.2	0.44	214	214	1.3
AU04A192	RG40.10	7743	5.1	1.9	96	4.0	17	199	22	12	2.8	225	205	4.0	6.6	3.1	522	319	33
AU04A193	RG40.11	1628	0.64	0.01	23	1.0	2.2	88	1.3	2.3	0.43	211	378	1.9	2.6	0.47	121	261	0.37
AU04A194	RG40.12	24128	1.1	0.38	560	33	6.4	294	2.5	16	0.35	315	214	4.4	1.3	0.58	125	351	13

FileName	SampleName	Fe57	Co59	Ni60	Cu65	Zn66	As75	Se77	Ag107	Sn118	Sb121	Te125	W182	Re185	Au197	Tl205	Pb208	Bi209	U238
AU04A093	RG43.1	0.0	0.01	0.01	1.8	0.20	0.0	495	0.08	0.10	0.03	55	15	18	0.01	0.0	16	45	0.05
AU04A094	RG43.2	5030	4.8	1.0	60	32	8.2	184	20	6.2	4.1	3646	335	6.2	1.2	12	2562	6218	9.4
AU04A095	RG43.3	5188	8.4	0.31	1157	1820	17	470	76	11	6.8	2048	94	2.2	3.3	25	4022	3470	4.1
AU04A096	RG43.4	6257	2.6	0.26	73	10	5.1	512	10	2.8	2.2	3109	49	5.9	1.5	9.3	2842	5076	0.80
AU04A097	RG43.5	5858	2.6	0.22	531	33	7.7	445	10	4.3	1.9	4380	49	0.54	0.66	9.1	1692	7258	0.25
AU04A098	RG43.6	600	0.30	0.09	770	4.2	0.2	493	5.0	0.23	0.97	1710	22	4.3	0.31	1.4	1279	2776	0.00
AU04A099	RG43.7	57	1.5	0.08	8.7	0.7	1.1	486	19	0.12	1.9	1859	26	2.1	0.53	1.4	1678	3040	0.00
AU04A100	RG43.8	1666	0.37	0.00	734	13	1.5	481	6.8	0.09	0.86	347	28	1.9	0.06	0.24	806	558	0.00
AU04A101	RG43.9	4109	3.4	0.10	1433	59	7.1	450	17	3.0	2.9	2202	146	1.4	1.2	8.4	2279	3820	0.52
AU04A102	RG43.10	1301	3.5	0.09	21	3.8	1.9	553	26	0.91	5.0	24705	114	1.4	0.54	21	3459	40308	0.00
AU04A103	RG43.11	16	0.63	0.00	2.8	0.3	9.0	481	5.3	0.16	0.65	1624	40	0.40	0.15	1.2	434	2469	0.00
AU04A104	RG43.12	445	0.93	0.08	6.4	1.7	1.3	275	9.1	0.66	1.2	2814	191	4.2	0.80	5.4	1282	4501	0.53

FileName	SampleName	Fe57	Co59	Ni60	Cu65	Zn66	As75	Se77	Ag107	Sn118	Sb121	Te125	W182	Re185	Au197	Tl205	Pb208	Bi209	U238
AU04A221	RG44.1	2262	1.8	0.47	24	15	11	158	2.7	29	2.4	356	165	2.0	0.27	3.1	904	775	27
AU04A222	RG44.2	396	1.4	0.08	12	2.2	4.6	250	3.7	5.9	1.5	1113	80	1.4	0.15	3.2	621	1706	4.1

AU04A223	RG44.3	5683	0.69	0.28	5.1	14	2.5	251	0.38	11	1.6	496	48	4.4	0.08	2.6	257	779	0.67
AU04A224	RG44.4	1502	0.53	0.24	4.3	5.7	2.4	233	0.60	4.2	0.88	765	58	1.4	0.11	1.1	258	1134	1.0
AU04A225	RG44.5	113	0.07	0.11	2.8	1.9	0.4	286	0.16	0.21	0.21	734	19	4.4	0.02	0.35	85	1176	0.37
AU04A226	RG44.6	229	1.1	0.03	2.4	1.7	1.9	287	0.46	0.73	1.0	1483	35	4.4	0.08	2.7	351	2565	0.27
AU04A227	RG44.7	510	2.7	0.26	7.6	4.7	7.9	278	1.4	9.3	3.3	3459	64	0.71	0.27	6.6	910	6255	11
AU04A228	RG44.8	7084	0.92	0.34	21	30	3.8	259	1.3	9.0	0.92	845	92	2.0	0.11	2.8	321	1324	4.9
AU04A229	RG44.9	1127	0.91	0.18	5.4	6.6	3.0	227	0.90	4.3	1.4	1786	68	2.6	0.36	1.4	355	3111	0.81
AU04A230	RG44.10	1975	0.83	0.09	7.2	8.2	5.6	236	1.3	10	1.1	550	65	1.2	0.13	1.5	432	852	3.6

FileName	SampleName	Fe57	Co59	Ni60	Cu65	Zn66	As75	Se77	Ag107	Sn118	Sb121	Te125	W182	Re185	Au197	Tl205	Pb208	Bi209	U238
AU04A018	RG45.1	86	0.45	0.05	0.99	0.47	1.9	444	132	0.20	8.6	14902	25	4.9	0.40	8.3	7202	23342	0.03
AU04A019	RG45.2	299	0.49	0.03	1.42	1.6	1.1	354	18	0.81	1.0	101	43	2.2	0.23	0.63	4167	179	0.05
AU04A020	RG45.3	290	0.09	0.02	1.04	1.1	0.3	325	12	0.16	0.79	962	30	0.89	0.04	1.2	1908	1540	0.01
AU04A021	RG45.4	4.4	0.07	0.03	0.83	0.39	0.7	360	33	0.12	1.7	1188	27	2.0	0.05	0.18	6522	1865	0.00
AU04A022	RG45.5	5.1	0.06	0.02	0.83	0.69	0.2	314	5.3	0.10	1.0	785	32	1.8	0.07	0.06	1608	1210	0.01
AU04A025	RG45.6	2.3	0.01	0.03	0.49	0.33	0.64	316	3.1	0.07	17	3037	32	3.1	0.01	0.02	1762	4911	0.04
AU04A026	RG45.7	1.6	0.06	0.00	0.58	0.45	3.3	355	0.8	0.08	0.75	711	45	2.0	0.0	0.04	243	1075	0.00
AU04A027	RG45.8	334	0.79	0.00	0.64	1.1	1.8	580	130	0.14	16	35599	52	3.7	0.50	8.7	15602	52682	0.00
AU04A028	RG45.9	303	0.09	0.06	1.8	1.6	5.9	283	0.8	1.5	0.13	38	62	0.7	0.26	0.16	46	23	0.13
AU04A029	RG45.10	35	0.2	0.02	0.38	0.35	0.66	477	64	0.07	9.1	13832	37	2.5	0.18	1.1	10940	22156	0.00
AU04A030	RG45.11	2896	3.6	0.23	17	9.6	9.0	236	44	11	8.7	1938	364	3.1	2.0	11	11390	3271	5.1
AU04A031	RG45.12	1326	2.3	0.15	11	6.4	4.6	213	32	11	5.1	514	346	5.6	3.3	4.6	9619	954	2.5
AU04A032	RG45.13	24	0.04	0.00	1.2	0.45	0.10	311	1.1	0.09	0.22	70	33	3.7	0.08	0.04	216	64	0.01
AU04A033	RG45.14	4.9	0.12	0.03	2.0	0.52	1.1	322	2.6	0.06	0.61	495	38	2.8	2.3	0.05	611	602	0.00
AU04A034	RG45.15	68	0.23	0.07	1.2	0.53	0.31	305	6.1	0.20	0.38	64	39	3.1	0.09	0.08	1144	73	0.03
AU04A035	RG45.16	1035	0.30	0.20	2.1	4.5	0.86	357	28	1.1	3.7	7250	34	3.8	0.24	2.9	3410	12212	0.12

FileName	SampleName	Fe57	Co59	Ni60	Cu65	Zn66	As75	Se77	Ag107	Sn118	Sb121	Te125	W182	Re185	Au197	Tl205	Pb208	Bi209	U238
AU04A273	RG49.1	3.4	0.02	0.06	0.48	0.80	6.9	285	4.5	1.7	0.01	48	72	1.9	0.01	0.27	3.8	0.84	4.1
AU04A274	RG49.2	2.3	0.02	0.09	1.2	0.31	0.74	247	0.47	1.0	0.03	10	67	2.6	0.01	0.06	10	1.6	0.29
AU04A275	RG49.3	1555	0.48	0.09	2.3	3.3	3.8	80	2.9	6.8	0.23	27	147	7.6	0.01	1.4	155	62	5.0
AU04A276	RG49.4	2.7	0.03	0.00	0.78	0.67	0.35	211	0.36	0.93	0.04	11	177	2.5	0.00	0.12	29	6.9	0.09
AU04A277	RG49.5	4044	0.61	0.14	5.1	9.8	4.0	242	2.1	4.6	0.25	31	73	1.3	0.01	0.84	68	30	6.7
AU04A278	RG49.6	3.3	0.06	0.09	0.53	1.4	2.5	173	0.10	6.1	0.00	19	163	3.7	0.00	0.00	2.8	1.4	0.00
AU04A279	RG49.7	56	0.77	0.00	1.5	0.88	6.4	91	7.9	25	0.49	48	196	4.2	0.04	3.9	700	152	9.3
AU04A280	RG49.8	15	0.84	0.14	1.7	1.0	10	317	4.6	0.35	0.17	57	56	1.6	0.02	0.32	983	62	0.02

AU04A281	RG49.9	2557	1.4	0.17	6.1	5.3	4.6	113	5.0	11	0.53	38	235	4.5	0.02	2.7	810	102	11	
AU04A282	RG49.10	301	0.09	0.00	1.5	1.3	3.6	290	7.0	4.5	0.11	68	50	2.1	0.01	1.4	45	90	1.9	
FileName	SampleName	Fe57	Co59	Ni60	Cu65	Zn66	As75	Se77	Ag107	Sn118	Sb121	Te125	W182	Re185	Au197	Tl205	Pb208	Bi209	U238	
AU04A147	RG51.1	3953	1.1	0.09	1.7	7.6	0.59	106	23	1.1	0.07	8.6	301	4.9	0.14	0.30	7.9	1.8	2.7	
AU04A148	RG51.2	5856	4.3	0.11	5.8	15	11	296	6.2	18	4.4	70	85	5.4	0.00	5.4	414	84	7.2	
AU04A149	RG51.3	3583	2.2	0.06	6.7	10	5.9	153	8.6	9.6	1.7	36	146	14	0.01	4.2	342	66	7.5	
AU04A150	RG51.4	789	1.7	0.09	8.7	4.0	9.0	319	2.3	2.4	1.8	129	60	3.8	0.00	1.1	612	139	0.43	
AU04A151	RG51.5	547	0.18	0.00	1.3	1.0	0.65	59	0.39	0.50	0.13	22	354	11	0.00	0.13	38	20	1.2	
AU04A152	RG51.6	1.3	0.01	0.32	0.79	2.2	3.0	333	0.03	13	0.00	46	53	6.3	0.00	0.00	0.33	0.10	0.01	
AU04A153	RG51.7	6.7	0.01	0.00	0.57	0.87	8.8	320	0.03	0.56	0.01	37	68	6.1	0.00	0.00	0.19	0.02	0.00	
AU04A154	RG51.8	28	0.02	0.10	1.8	1.2	12	331	0.05	0.29	0.03	42	73	2.9	0.01	0.01	0.43	0.05	0.01	
AU04A155	RG51.9	104	0.03	0.11	7.5	2.5	12	340	0.04	2.9	0.01	43	38	3.4	0.00	0.01	0.78	0.25	0.02	
AU04A156	RG51.10	690	0.28	0.12	4.0	3.4	0.58	138	0.09	0.78	0.31	8.0	199	6.5	0.01	0.09	9.4	5.2	0.25	
AU04A157	RG51.11	137	0.07	0.06	9.2	2.2	8.4	296	0.06	1.5	0.02	29	41	0.92	0.02	0.01	1.0	0.35	0.41	
AU04A158	RG51.12	6743	2.5	0.12	2.9	16	6.2	294	11	6.2	1.8	66	66	5.6	0.04	2.1	322	72	3.4	
WRD10600004	FileName	SampleName	Fe57	Co59	Ni60	Cu65	Zn66	As75	Se77	Ag107	Sn118	Sb121	Te125	W182	Re185	Au197	Tl205	Pb208	Bi209	U238
AU04A173	RG55.1	1408	1.4	2.9	291	13	2.2	562	0.83	1.4	0.26	41	213	4.0	5.0	0.23	51	81	0.36	
AU04A174	RG55.2	2353	1.1	4.0	2473	14	7.7	498	0.66	5.6	0.22	32	276	0.70	6.8	0.09	55	74	0.11	
AU04A175	RG55.3	2213	2.4	6.8	1329	26	5.6	517	5.0	6.2	1.0	95	276	1.2	24	0.33	138	306	0.44	
AU04A176	RG55.4	993	1.7	4.4	714	9.3	4.2	483	3.1	3.3	0.40	73	124	2.6	7.0	0.40	85	157	0.44	
AU04A177	RG55.5	1113	0.6	2.1	237	13	1.1	433	0.54	1.6	0.23	34	64	1.8	2.1	0.20	26	27	0.15	
AU04A178	RG55.6	3499	4.6	17	317	30	8.1	593	7.5	6.1	4.4	119	418	0.52	21	1.1	160	403	1.2	
AU04A179	RG55.7	1686	3.4	9.4	1349	14	6.5	518	5.1	4.0	1.8	209	210	0.61	75	0.57	256	741	0.13	
AU04A180	RG55.8	8445	6.6	22	363	86	8.8	478	5.4	12	1.1	212	476	0.66	29	0.72	287	573	2.1	
AU04A181	RG55.9	914	1.7	5.5	878	18	7.0	512	10	1.1	1.2	205	247	0.79	148	0.16	154	803	0.01	
AU04A182	RG55.10	2383	3.4	9.2	416	19	6.1	419	14	5.5	1.6	212	135	0.36	92	0.67	292	725	0.50	
FileName	SampleName	Fe57	Co59	Ni60	Cu65	Zn66	As75	Se77	Ag107	Sn118	Sb121	Te125	W182	Re185	Au197	Tl205	Pb208	Bi209	U238	
AU04A259	RG56.1	1929	2.9	5.6	79	8.4	24	285	14	26	0.35	128	85	0.04	36	0.11	179	328	0.81	
AU04A260	RG56.2	3722	7.5	13	308	19	5.0	309	15	8.0	1.2	132	155	0.35	25	0.48	441	343	3.4	
AU04A261	RG56.3	8883	8.2	23	322	27	7.9	268	104	24	0.50	159	131	0.24	102	0.70	355	405	6.9	
AU04A262	RG56.4	15638	11	37	320	62	3.9	281	22	16	0.70	115	140	0.17	27	1.1	246	236	8.8	
AU04A263	RG56.5	190	0.15	0.50	15	1.2	0.36	269	0.17	0.16	0.01	48	41	0.44	0.6	0.02	7.5	12	0.10	
AU04A264	RG56.6	147	0.56	0.69	45	3.3	5.4	271	3.4	0.53	0.14	53	55	0.34	7.1	0.03	43	46	0.01	

AU04A265	RG56.7	2205	3.3	9.4	270	20	6.7	306	3.9	69	0.35	73	190	0.25	1.2	0.12	277	102	0.78
AU04A266	RG56.8	2556	4.8	6.9	524	11	9.4	280	5.3	2.8	0.45	179	173	0.45	34	1.2	360	584	0.14
AU04A267	RG56.9	10370	7.6	18	448	32	16	333	5.4	7.9	0.44	137	347	0.18	24	1.7	255	415	0.45
AU04A268	RG56.10	20770	9.3	27	106	39	2.6	284	2.2	3.1	0.60	93	145	2.2	17	2.5	493	347	0.35
AU04A269	RG56.11	2556	20	17	358	11	4.5	388	4.7	5.9	0.99	175	260	3.3	33	2.5	577	831	0.10
AU04A270	RG56.12	12620	4.9	16	184	37	1.2	325	1.2	1.0	0.35	77	110	2.5	13	2.1	177	198	0.04
AU04A271	RG56.13	3968	12	13	130	13	6.8	409	125	9.0	0.67	184	410	0.88	435	1.8	460	825	0.44
AU04A272	RG56.14	22375	11	31	70	41	8.2	342	4.9	2.8	0.65	101	298	1.2	34	2.5	338	409	0.37

FileName	SampleName	Fe57	Co59	Ni60	Cu65	Zn66	As75	Se77	Ag107	Sn118	Sb121	Te125	W182	Re185	Au197	Tl205	Pb208	Bi209	U238
AU04A199	RG60.1	795	6.4	6.5	148	13	5.6	337	16	4.6	0.3	58	115	0.40	13	0.12	107	129	0.06
AU04A200	RG60.2	340	1.4	2.0	86	6.2	2.8	365	33	4.7	0.6	116	65	0.46	55	0.06	319	440	0.05
AU04A201	RG60.3	10401	14	13	286	40	12	433	146	13	1.4	141	159	0.57	122	0.99	610	655	0.93
AU04A202	RG60.4	574	5.9	9.3	329	21	10	386	160	1.2	0.40	148	99	0.42	17	0.19	311	356	0.05
AU04A203	RG60.5	178	2.1	3.7	161	3.8	2.9	317	138	0.88	0.25	168	99	0.15	13	0.26	92	457	0.02
AU04A204	RG60.6	748	26	31	375	47	6.1	346	33	1.1	0.18	59	188	0.35	1.6	0.11	111	99	0.34
AU04A205	RG60.7	678	5.4	7.4	206	15	5.0	438	41	1.2	0.37	100	98	5.2	17	0.18	227	268	0.20
AU04A206	RG60.8	557	2.3	7.5	152	2.3	4.5	354	91	0.34	0.16	95	65	0.67	67	0.03	54	178	0.00
AU04A207	RG60.9	57	3.6	4.0	34	5.8	2.6	469	40	0.14	0.16	50	207	1.8	32	0.04	72	167	0.05
AU04A208	RG60.10	1541	14	21	760	49	5.3	441	77	2.6	0.40	89	84	4.5	18	0.25	189	238	0.31
AU04A209	RG60.11	572	83	125	537	125	3.4	454	326	2.6	0.76	182	116	5.9	83	0.36	498	586	0.79
AU04A210	RG60.12	243	4.0	4.4	130	6.3	2.9	458	47	1.4	0.38	84	180	1.6	9.3	0.24	167	295	0.16

FileName	SampleName	Fe57	Co59	Ni60	Cu65	Zn66	As75	Se77	Ag107	Sn118	Sb121	Te125	W182	Re185	Au197	Tl205	Pb208	Bi209	U238
AU04A003	RG62.1	575	0.51	0.76	414	5.3	1.7	535	0.33	0.38	0.11	43	92	1.6	3.4	0.08	30	53	0.01
AU04A004	RG62.2	635	1.5	2.1	257	9.5	1.6	414	4.9	0.66	0.26	92	93	0.12	2.0	0.37	33	257	0.08
AU04A005	RG62.3	1029	0.55	0.92	706	16	1.4	410	0.68	0.45	0.09	54	58	1.7	2.7	0.60	18	47	0.00
AU04A006	RG62.4	1181	2.4	3.9	90	15	3.0	485	1.4	0.30	0.25	144	197	1.9	8.9	0.32	50	326	0.04
AU04A007	RG62.5	1904	11	25	51	85	3.9	471	5.5	1.3	0.35	134	221	2.0	22	0.85	102	371	0.23
AU04A008	RG62.6	96	0.58	0.90	23	0.18	0.28	447	0.14	0.07	0.02	48	50	0.15	0.55	0.04	1.3	12	0.00
AU04A009	RG62.7	9465	5.0	10	29	149	2.5	420	5.2	1.4	0.39	179	161	1.7	15	1.6	106	225	0.34
AU04A010	RG62.8	3212	2.2	4.1	39	67	3.9	403	0.58	0.50	0.15	543	82	0.21	6.6	0.58	42	999	0.05
AU04A011	RG62.9	10591	4.2	9.5	15	91	3.4	347	0.90	1.2	0.20	75	116	0.17	2.4	1.3	38	81	0.08
AU04A012	RG62.10	4205	2.9	5.7	20	82	4.6	540	2.3	1.1	0.21	158	220	0.31	11	1.1	62	213	0.52
AU04A013	RG62.11	101	0.53	0.43	26	5.2	18	442	1.3	0.20	0.08	340	96	0.06	21	0.04	10	521	0.03
AU04A014	RG62.12	13456	7.4	14	50	270	4.8	433	5.4	1.9	0.38	222	269	1.3	26	1.3	234	274	0.48

AU04A015	RG62.13	979	3.0	4.4	68	84	7.5	387	3.6	1.0	0.37	158	188	0.40	8.9	0.88	98	207	0.16
AU04A016	RG62.14	42	0.81	1.3	32	1.7	7.9	362	0.29	0.49	0.08	142	82	0.05	1.1	0.02	21	143	0.00
AU04A017	RG62.15	40	0.75	0.84	30	3.2	6.0	342	1.0	0.25	0.07	203	63	0.31	9.3	0.06	8.4	240	0.00

FileName	SampleName	Fe57	Co59	Ni60	Cu65	Zn66	As75	Se77	Ag107	Sn118	Sb121	Te125	W182	Re185	Au197	Tl205	Pb208	Bi209	U238
AU04A057	RG64.1	12365	5.7	8.7	220	41	3.9	475	8.6	0.75	0.93	79	108	16	14	3.1	160	159	0.11
AU04A058	RG64.2	2609	8.6	6.3	94	7.8	10	452	24	1.2	3.1	197	105	0.46	20	4.3	273	475	0.09
AU04A059	RG64.3	1495	11	7.0	469	5.0	5.5	463	38	1.4	2.1	250	124	1.1	86	2.9	424	629	0.01
AU04A060	RG64.4	1557	5.6	4.8	104	5.9	3.7	404	46	0.2	0.9	216	92	0.49	111	0.92	387	724	0.01
AU04A061	RG64.5	6556	44	30	1018	20	28	455	31	9.4	11.4	256	247	1.3	14	14	1491	997	2.3
AU04A062	RG64.6	3506	7.1	4.5	75	10	16	491	42	1.3	1.9	230	84	0.25	64	1.2	218	448	0.11
AU04A063	RG64.7	31885	10	17	23	85	11	502	1.2	1.7	0.39	48	396	110	1.4	2.4	44	15	0.96
AU04A064	RG64.8	21739	7.5	13	16	61	8.2	385	3.0	1.2	0.30	127	430	218	3.9	2.0	138	340	2.0
AU04A065	RG64.9	3857	2.7	4.1	23	14	5.6	594	386	0.54	0.34	153	351	135	517	0.43	165	379	1.5
AU04A066	RG64.10	5307	1.8	3.2	110	15	10	493	0.71	6.8	0.10	49	359	191	0.58	0.55	9.0	54	0.18
AU04A067	RG64.11	12458	5.2	7.5	158	36	3.9	415	32	0.88	1.1	145	91	1.2	18	3.6	149	336	0.02
AU04A068	RG64.12	1201	2.7	2.3	118	4.3	2.8	526	18	0.61	1.1	130	67	3.0	31	0.44	207	222	0.02
AU04A069	RG64.13	5825	8.4	8.2	343	14	14	475	81	4.6	2.2	314	602	1.8	122	2.9	603	1146	3.3
AU04A070	RG64.14	13372	50	46	344	15	31	566	114	22	6.7	278	459	2.5	75	18	1245	1356	39
AU04A071	RG64.15	9027	38	28	394	26	28	501	285	3.6	10	246	567	3.3	402	17	835	926	0.64
AU04A072	RG64.16	4335	12	8.4	88	14	11	518	13	1.7	3.8	136	159	0.66	10	3.1	373	300	0.24
AU04A073	RG64.17	33273	11	18	103	85	10	490	23	2.1	1.9	200	329	1.4	39	5.1	356	536	0.24
AU04A074	RG64.18	5110	10	7.4	3010	85	8.9	548	32	3.3	2.1	434	150	1.8	46	3.2	494	1287	0.56
AU04A075	RG64.19	2073	18	12	227	6.1	13	687	37	1.0	2.5	170	130	0.50	47	7.4	278	539	0.08

FileName	SampleName	Fe57	Co59	Ni60	Cu65	Zn66	As75	Se77	Ag107	Sn118	Sb121	Te125	W182	Re185	Au197	Tl205	Pb208	Bi209	U238
AU04A245	RG65.1	5509	2.8	7.3	88	39	5.3	335	9.2	3.0	1.2	238	96	4.1	19	0.49	244	718	4.5
AU04A246	RG65.2	28	1.0	0.47	29	4.0	2.2	371	0.07	1.1	0.05	27	70	4.0	0.01	0.01	5.4	5.1	0.01
AU04A247	RG65.3	3029	0.9	2.9	38	21	5.1	314	7.4	3.6	0.31	71	95	1.0	2.5	0.50	72	158	1.6
AU04A248	RG65.4	9457	4.0	9.6	64	43	5.6	357	27	7.0	0.47	206	144	2.4	71	0.84	160	744	3.2
AU04A249	RG65.5	153	0.0	1.7	3.0	10	4.7	311	0.05	34	0.00	31	60	1.5	0.05	0.01	2.2	2.8	0.06
AU04A250	RG65.6	359	1.0	0.64	19	2.4	1.9	325	0.29	0.34	0.04	31	117	0.26	0.02	0.06	3.1	5.1	0.04
AU04A251	RG65.7	4566	2.6	3.3	240	132	3.9	310	26	28	1.3	457	104	0.66	15	0.67	151	2105	4.6
AU04A252	RG65.8	1843	2.3	4.7	114	31	13	387	464	9.2	9.9	117	88	1.6	273	1.4	78	1087	5.1
AU04A253	RG65.9	1057	2.1	3.5	206	58	6.9	373	98	56	1.4	189	83	0.97	55	1.5	114	781	0.64
AU04A254	RG65.10	2637	19	5.0	767	12	1.8	357	1.0	0.73	0.23	40	107	0.49	0.0	0.15	14	84	0.02

